DESIGN AND IMPLEMENTATION OF COMPACT RECONFIGURABLE ANTENNAS FOR UWB AND WLAN APPLICATIONS

A Dissertation
Presented to
The Academic Faculty

By

Symeon Nikolaou

In Partial Fulfillment
of the Requirements for the Degree
Doctor of Philosophy
in the
Electrical and Computer Engineering

School of Electrical and Computer Engineering
Georgia Institute of Technology
August 2007

DESIGN AND IMPLEMENTATION OF COMPACT RECONFIGURABLE ANTENNAS FOR UWB AND WLAN APPLICATIONS

Approved by:

Dr. Manos M. Tentzeris, Advisor
Associate Professor, School of ECE
Georgia Institute of Technology

Dr. John D. Cressler
Professor, School of ECE
Georgia Institute of Technology

Dr. John Papapolymerou, Co-Advisor
Associate Professor, School of ECE
Georgia Institute of Technology

Dr. Andrew F. Peterson
Professor, School of ECE
Georgia Institute of Technology

Dr. Joy Laskar
Professor, School of ECE
Georgia Institute of Technology

Dr. Chang-Ho Lee
Director,
Samsung Design Center

Date Approved: June 26, 2007

AKNOWLEDGEMENTS

This work would not have been completed without the support, help and guidance of several people, in many different levels. To every one and each of them I owe a big dept of gratitude. Therefore I would like to express my sincere thanks to:

- My family, for their constant love, patience and support.
- My advisors, Prof. Manos M. Tentzeris and Prof. Papapolymerou for their academic guidance, financial support and the constant encouragement and motivation for academic excellence.
- Prof. Laskar, Prof. Cressler, Prof. Peterson and Dr. Chang-Ho Lee, for serving on my defense committee, and for their suggestions and evaluations that improved the quality of this work.
- Dr. Ponchak for his invaluable help with antenna testing.
- All students and post-doctoral fellows, current and past, of ATHENA and MIRCTECH research groups for a smooth and fruitful collaboration.
- My friends in Atlanta, Cyprus and Athens, for their support and understanding and for making my studies a pleasant experience.
- The staff of ECE and GEDC for their administrative assistance.

TABLE OF CONTENTS

LIST OF TABLES

LIST OF FIGURES

LIST OF SYMBOLS AND ABBREVIATIONS

1D	One Dimensional
2D	Two Dimensional
3D	Three Dimensional
3G	Third Generation
4G	Fourth Generation
Ag	Silver
AM	Amplitude Modulated
AUT	Antenna-Under-Test
CAD	Computer-aided Design
CPW	Coplanar Waveguide
CTE	Coefficient of Thermal Expansion
Cu	Copper
DC	Direct Current
EIRP	Equivalent Isotropically Radiated Power
FCC	Federal Communications Commission
FEM	Finite Element Method
FDTD	Finite Difference Time Domain
FM	Frequency Modulated
GSM	Global System of Mobile Communications
HFSS	High Frequency System Simulator
HIPERLAN	High Performance Radio Local Area Network

IC	Integrated Circuit
IF	Intermediate Frequency
ISM	Industrial-Scientific-Medical
LCP	Liquid Crystal Polymer
LTCC	Low Temperature Co-fired Ceramic
MCM	Multichip Module
MEMS	Micro-Electro-Mechanical Systems
MoM	Method of Moments
RF	Radio Frequency
RFID	Radio Frequency Identification
RLC	Resistor-Inductor-Capacitor
SIP	System-in-a-Package
SOC	System-on-Chip
SOLT	Short, Open, Load, and Thru
SOP	System-on-Package
TE	Transverse Electric
TLM	Transmission Line Matrix
TM	Transverse Magnetic
UHF	Ultra High Frequency
VHF	Very High Frequency
VSWR	Voltage Standing Wave Ratio
WBAN	Wireless Body Area Networks
WLAN	Wireless Local Area Networks

SUMMARY

The objective of this research is to realize compact and reconfigurable antennas for next generation Ultra Wide Band (UWB) and Wireless Local Area Network (WLAN) applications. The contributions of this research are, a methodology for designing compact UWB antennas, a compact WLAN prototype antenna with reconfigurable characteristics in both radiation pattern and frequency of operation, and compact UWB antennas with reconfigurable WLAN band rejection characteristics.

For the completion of this dissertation, five research projects have been studied. First, a double exponentially tapered slot antenna with conformal shape, high gain, and consistent radiation patterns is implemented. The radiation pattern consistency results in minimum distortion for any transmitted pulse.

The second and third projects involve an elliptical slot with a tuning uneven U-shaped stub and two cactus-shaped monopoles. The elliptical slot demonstrates omni-directional radiation patterns and compact size. As an improved iteration of the elliptical slot antenna, two cactus-shaped monopoles are implemented. The two prototypes occupy only 60% and 40%, respectively, of the area that the original elliptical slot occupies resulting in a significant size reduction, while maintaining omni-directional radiation patterns. Through the cactus-shaped monopoles some general design methodologies for UWB antennas are introduced and successfully applied.

The fourth research topic introduced, concerns the study of compact elliptical UWB monopoles. Several prototypes of different geometrical characteristics were designed and tested. Broadband matching techniques and the integration of reconfigurable features on

the elliptical radiator are investigated. For the reconfigurable UWB antenna, resonating elements are used to create a rejection band in the frequency range that is occupied by WLAN applications.

The performance of several of the introduced slot and monopole antennas are tested when the antennas under detection are mounted and operate on non-planar surfaces.

Finally, a reconfigurable annular slot antenna operating at the wireless local area network (WLAN) band is implemented. The proposed antenna demonstrates reconfigurable characteristics in both radiation pattern and return loss.

All of the UWB antennas are fabricated on liquid crystal polymer (LCP) and can be easily integrated with active components on the same module using system on package (SoP) technology.

CHAPTER I

INTRODUCTION

Currently there are several wireless systems applications in a multitude of areas such as mobile and personal communications, radio-frequency (RF) identification, wireless local area networks (WLAN), remote sensing, etc. Regardless of the application, most of those systems have similar demands for increased functionality, improved performance, compact size, and most importantly lower development cost. An objective that attracts a lot of effort is the integration of multiple functions on a single convergent system. Such a system requires a one-step integrated solution for all sensing, computing, and communicating functions. An example could be a device, which can function as a cell phone, monitor weather, store data, perform basic computations, connect to the internet and can be hand-worn like a simple watch. Such devices require an effective packaging technique and a versatile transceiver that would be able to operate in different frequencies. Ideally this versatile operation would be dynamic. For the operation versatility a cognitive radio is desired. Cognitive radio is a communications system which can change its transmission or reception parameters to communicate efficiently without interfering with licensed users. An approach like that, requires reconfigurable modules and therefore reconfigurable antennas.

Although different packaging approaches have been investigated in order to create such convergent systems, like system-on-a-chip (SoC), multichip module (MCM), and system-in-a-package (SiP), the system-on-a-package (SoP) approach [1-3] has been identified as the best solution to implement multiple system functions into one compact, low-cost, high-performance packaged system. In a SoP-based system, the package

performs the functions of powering, cooling and interconnecting these chips and additionally it houses passive functionality. Those passives are built on and/or embedded inside the package and therefore the package and the chip(s) have to be designed together in a SoP system. Part of the SoP challenge is the identification of suitable material technology that supports such integration. For example, a viable 3-D SoP technology for wireless communication applications would require building blocks such as active components, embedded passives, integrated antennas, and a suitable platform to integrate the different parts. The material platform should provide excellent electrical properties, mechanical stability, chemical resistance, good barrier properties, multilayer lamination capabilities, and be cost competitive. Microwave composites and ceramics are attractive candidates that have been identified as suitable platforms for a SoP system. Microwave composites such as variations of Rogers Duroid or Taconic RF [4,5] series materials use proprietary mixes of materials like polytetraflouroethylene (PTFE), glass weave, and ceramic fills. These materials are carefully engineered for excellent performance, but are expensive. Furthermore, because a mix of materials is used, the homogenity is lost. Low-temperature co-fired ceramic (LTCC) is one of the very few substrates that satisfies nearly all the requirements [6,7] however LTCC may not be ideal for all applications. For example, printed antennas on LTCC substrates suffer from reduced efficiency because of their relatively high dielectric constant (ε_r=5.4−9.1). Furthermore, LTCC is still expensive compared to conventional laminate materials. Another disadvantage with the LTCC process is that its process temperature (800◦C −1000◦C) may not be acceptable for some fully integrated solutions. As an example, micro-electro-mechanical system (MEMS) switches which are necessary for the design of smart reconfigurable systems

cannot survive this high processing temperature. The comparatively high processing temperature of LTCC prevents the incorporation of MEMS-based reconfigurability into systems developed on an LTCC platform. Therefore to realize the full advantages of an integrated SoP system, especially for reconfigurable systems alternative material technologies need to be explored such as liquid crystal polymer (LCP).

1.1 Liquid Crystal Polymer (LCP)

LCP is an organic, (it is comprised of only carbon, oxygen, and hydrogen molecules) thin film material. When created, it starts as a liquid polymer (a polymer is physically similar to a plastic; it is slightly different chemically) that is heated to the "liquid crystal" temperature. At this point the molecules align into a pseudo-crystalline structure with spacial regularity. Materials that form this type of structure are incredibly strong and LCP is no exception. In fact, LCP is so versatile because it combines the strengths of strong crystal bonds with the benefits of polymer materials (flexibility and inexpensive to make). For these reasons, LCP has been targeted as a possible substitute for expensive semiconductor substrates in micro-electro-mechanical system (MEMS) devices like MEMS switches.

Although LCP's superior substrate properties have been well known for almost a decade now [8, 9], manufacturing difficulties [10, 11] have prevented it from being considered as a serious candidate for RF applications. Recent advances in LCP processing [12,13] have changed the situation, though, and it has gained immediate attention among RF researchers [14, 15] since then. LCP offers a unique combination of properties that makes it an attractive technology for SoP-based systems. Since it is quasi-hermetic, it has the potential to act both as package and as substrate. It is significantly

cheaper compared to ceramics (LTCC) and other composite materials (Duroid). Its multilayer lamination capabilities make it suitable for the integration of various modules. Especially its flexibility makes it a good candidate for wearable electronics. Its stable electrical properties, low processing temperature (~ 285^{o}C), and low cost make it an attractive material for developing smart, reconfigurable, and fully integrated RF systems using SoP technology.

1.2 Statement of topic

The objective of this research is to realize compact and reconfigurable antennas for next generation ultra wide band (UWB) and wireless local area network (WLAN) applications. For the reconfigurable UWB antennas MEMS switches are used while for the reconfigurable WLAN antenna, PIN diodes are used. For the UWB elliptical monopole two types of resonating elements are used to create a rejection band in the frequency range that is occupied by WLAN applications. The annular slot antenna has reconfigurable frequency of operation and it also has reconfigurable radiation pattern.

1.3 Contributions and Organization

The contributions of this research are, a methodology for designing compact UWB antennas, a compact WLAN prototype antenna with reconfigurable characteristics in both radiation pattern and frequency of operation, and compact UWB antennas with reconfigurable WLAN band rejection characteristics.

Chapter 2 presents the background information, and previous achievements concerning antenna designs for miscellaneous UWB applications, design methodologies and reported compact antennas and finally publications on reconfigurable, or potentially

reconfigurable UWB antennas. The objective is to demonstrate the work completed and published on the topic of the current thesis before this research work was completed.

A number of UWB antennas for both radar and personal mobile communications applications are presented in chapter 3 with major concern to achieve antennas with compact size and improved characteristics. The first proposed antenna is a double exponentially tapered slot antenna (DETSA), an endfire antenna with high gain, high directivity and relatively large size suitable for radar applications and wearable electronics. For UWB mobile, hand-held devices that require omni-directional pattern and compact size, four additional prototypes are proposed. An elliptical slot antenna tuned by a U-shaped stub, two iterations of a cactus-shaped monopole and lastly a CPW-fed elliptical monopole.

In chapter 4 an elliptical monopole with altered geometric characteristics is used to study a broadband transition from a standard CPW line to an elliptical UWB radiator. The customized transition reduces the relatively high real part of the input impedance of the antenna and therefore it significantly improves the matching.

The performance and behavior of conformal UWB antennas when they are mounted on cylindrical surfaces of various radii is investigated in chapter 5. Radiation pattern, frequency and time domain measurements are taken to explore the potential use of conformal antennas on LCP for wireless body area network (WBAN) applications.

Chapter 6 presents the two UWB antennas with the reconfigurable frequency notch at the frequency band allocated for WLAN applications (5-6 GHz). Two approaches are presented. In the first case a U-shaped slot is integrated on the elliptical monopole and in the second case two inverted L-shaped stubs are symmetrically added on the radiating

ellipse. The reconfigurability of the design is accomplished with the use of MEMS switches which are integrated with the antenna in a SoP approach. The MEMS switches do not need any bias lines to be actuated and therefore the radiation performance of the monopoles is not degraded or significantly affected in any way.

A reconfigurable antenna in both frequency and radiation pattern is introduced and investigated in chapter 7. A bidirectional annular slot antenna (ASA) is used, fabricated on Duroid substrate. Two matching stubs are used to match the antenna under detection at 5.2, 5.8 and 6.4 GHz. For the pattern reconfigurability two PIN diodes are used to direct the null of the radiation pattern in a predefined direction, and consequently protect the transceiver from a strong interference coming from that direction.

Finally chapter 8 concludes the thesis, summarizing its contribution.

CHAPTER II

BACKGROUND

On February 14, 2002, the Federal Communications Commission (FCC) announced an order [16] by which the unlicensed use of Ultra-wideband (UWB) in the frequency range from 3.1 to 10.6 GHz was authorized. The UWB frequency range was released partly in an attempt to meet the demand for high data rate communications in short distances for mobile and personal applications. Mobile handheld devices need to be small, lightweight, and relatively cheap to attract buyer's attention. Therefore, there is an increasing need for compact, low-cost UWB radios and consequently a need for compact UWB antennas. Since the operating frequencies for a UWB antenna have such a broad range, designing a compact antenna with consistent radiation characteristics remains a challenging problem.

Part of the designated spectrum for the UWB applications is shared by other applications, like wireless local area networks (WLAN) applications that use the IEEE 802.11a protocol (5.15-5.875 GHz), causing interference among neighboring radios. UWB radio's equivalent isotropically radiated power (EIRP), was defined to be below -41.3 dBm/MHz in the whole frequency range, making the emitted radiation almost undetectable for WLAN receivers. On the other hand, though, UWB transceivers suffer from strong interference from the radiation emitted by the WLAN transmitters, which is received from the UWB radios as noise. The coexistence of many radios in a constantly changing environment, where handheld devices join or leave a local network arbitrarily, make reconfigurable characteristics highly desirable for all transceivers. A special need exists for UWB and WLAN transceivers since they share part of the spectrum. Since the antenna is an absolutely necessary part of any radio, the reconfigurable characteristics

reflect on the antenna. An antenna may have a reconfigurable radiation pattern or reconfigurable return loss. Those "smart" antennas, which are intended for future smart radios, have attracted a lot of researchers' and industry's attention in recent years.

2.1 UWB Applications

Unlike WLAN applications, which are well known and defined as mobile or base station wireless network terminals, UWB applications have great variety [17]. Some of the current and potential applications are listed below.

- Altimeter/Obstacle avoidance radars
- Collision voidance sensors
- Tags
- Intrusion detection radars (through wall imaging)
- Industrial RF monitoring systems
- Wearable electronics for wireless body area network (WBAN)
- High speed WLANs and wireless personal area network (WPANs)

Depending on the application, the required antenna characteristics may vary significantly. For radar applications more directive antennas are needed; for WBAN applications conformal features may be necessary, while for mobile handheld devices omni-directional pattern characteristics are highly desirable. Handheld devices are the terminals for WLANs and WPANs. The UWB radios for wireless networks have many advantages that make them very appealing [18]. UWB signals are very difficult to intercept and they have multipath immunity because of the wide spectrum they use. The fact that UWB radios require fewer components results in small size, low weight, and additionally, relatively low cost. Last, UWB radios are low-power devices since the

emitted power is very low and the required components have typical consumption in microwatts, and low-power radios are especially desired for all battery-operated devices. Nevertheless, the performance of UWB radios can be significantly improved by the use of compact, reconfigurable antennas.

2.2 History of Compact Design

Different techniques were documented to reduce the size of antennas at a given frequency for a compact design. One simple method was the use of a dielectric substrate with higher ε_r value [19]-[21]. Although using higher ε_r value results in a size decrease, it also affected the efficiency of the antenna and in many cases was avoided. Another method used for resonant antennas was the use of meandered metal segments. The meandering was achieved by cutting slots in the non-radiating edges of the antenna [22]-[23]. This effectively elongated the surface current path on the antenna and increased the loading, which resulted in a decrease in the resonant frequency. This second technique could be used primarily for resonating antennas, like the antennas that are used for WLANs with the IEEE 802.11a protocol. However, for non-resonating antennas like the UWB antennas that radiate in a wide frequency, that technique could not be applied.

The earliest UWB antennas (Figure 2.1) reported in the literature were pretty sizeable in order to radiate effectively at the lower frequencies. Because of the variety of UWB applications, the proposed designs demonstrated equally great variety. Clearly, the early designs could not meet the size and integration characteristics that were necessary

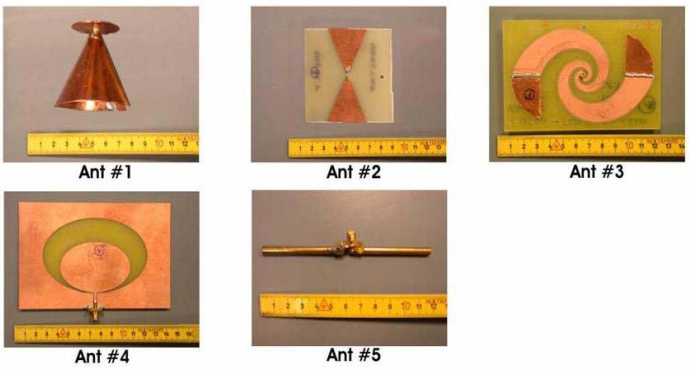

Figure 2.1: Early UWB antennas.

for mobile devices. One of the main issues was the fact that many of those designs were not printed; therefore, their integration with the other radio components was difficult. One of the early printed wideband antennas that were considered for UWB applications was the Vivaldi antenna [24]. Soon after, an improved variation of the Vivaldi antenna, the Double Exponentially Tapered Slot Antenna was introduced and generated a lot of attention [25]-[31] because of its easy matching and high gain. Although those antennas had appealing radiation and matching characteristics, they remained very large compared to the desired size for handheld devices. In addition they were directive antennas and therefore unsuitable for mobile devices that require omni-directional radiation patterns. A better approach than the endfire DETSA was the microstrip fed, or CPW fed slot antennas presented in [32]-[34]. Those slot antennas were not directive and were considerably smaller since the elliptical slots could support multiple radiation modes while maintaining relatively compact size. The development that made UWB antennas small enough to be used for mobile devices was the use of fat monopole antennas [35]-[36]. The effect of the small ground size of those fat monopoles and the transition from

the feed line to the load termination are some of the things that remain to be investigated and are part of the goals of this research.

2.3 History of Reconfigurable Antennas

The multitude of different standards in cell phones and other personal mobile devices requires compact multi-band antennas and smart antennas with reconfigurable features. The use of the same antenna for a number of different purposes, preferably in different frequencies, is highly desirable. A number of different reconfigurable antennas, planar and 3-D, were developed. Some of them were developed for radar applications [37]-[38] and other planar antennas were designed for wireless devices [39]-[42]. Most of those research works demonstrated only frequency reconfigurability. A reconfigurable annular slot antenna (ASA) will be considered in this research that will operate at three frequencies, with the central frequency at 5.8 GHz, and it will also have a reconfigurable radiation pattern. Pure and shorted annular slot antennas were thoroughly investigated both theoretically and experimentally [43]-[46]. Based on the annular slot radiator, several multiband designs were also implemented using various techniques [47]-[49]. For example in [48] (Figure 2.2), a simple microstrip feeding was used, but there was a second slot inside the first annular slot that created a different resonance. In this design all frequencies ranging from 2.4 GHz up to 6.8 GHz were excited at the same time. For the proposed design in this research, the antenna will radiate at predefined frequencies and the return loss will be controlled at will.

Since UWB antennas were investigated much later, no reports were found about reconfigurable UWB antennas. Some papers were published about UWB antennas with band stop characteristics [50]-[55]. Several ideas were introduced toward this

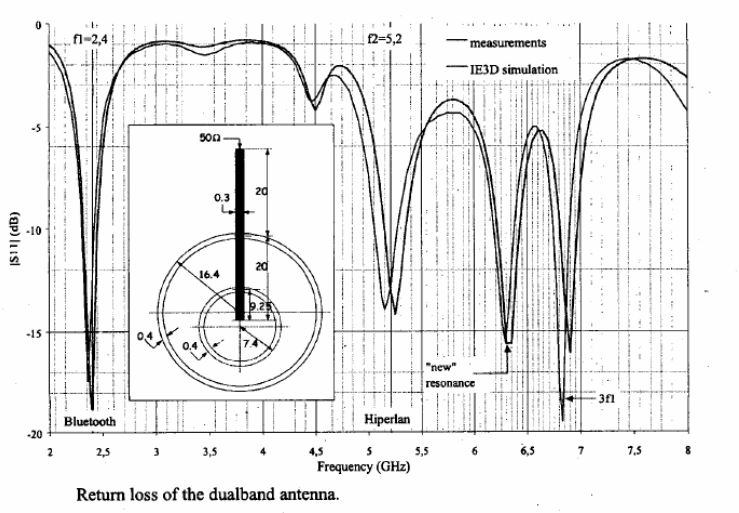

Return loss of the dualband antenna.

Figure 2.2 Multi-band annular slot antenna [48].

direction. The use of parasitic patches was used in [50] and a tuning stub was in [51], while short stubs on a slot line have been proposed in [52]. Nevertheless, the most popular solution has been the introduction of a U-shaped slot in a microstrip fed monopole, which has been used by many researchers [53]-[55]. In all cases, however, the return loss features are not reconfigurable in any way.

One of the goals of this research is to design and implement the first reconfigurable compact UWB antennas for next-generation systems.

CHAPTER III

MINIATURIZATION OF UWB ANTENNAS

A number of requisite research tasks for developing compact antennas for UWB applications have been accomplished by the author. Those steps are:

- Conformal Double Exponentially Tapered Slot Antenna (DETSA) on LCP [56]
- CPW-fed Elliptical Slot UWB Antenna with a Tuning Uneven U-shaped Stub on Liquid Crystal Polymer (LCP) [34]
- Cactus-shaped UWB Monopole Antenna [57-58]
- Compact UWB CPW-fed Elliptical Monopole on Liquid Crystal Polymer (LCP) [59]

Each of these accomplishments will be discussed individually.

3.1 Conformal Double Exponentially Tapered Slot Antenna (DETSA) on LCP

The rapid developments in broadband wireless communications and the great number of commercial and military applications necessitate new types of antennas that can support higher bit rates. The ultra wide band (UWB) [16] protocol using the spectrum from 3.1 GHz to 10.6 GHz is a new promising technology suitable for high rate communications in small distances. A double exponentially tapered slot antenna (DETSA) on a flexible LCP organic material suitable for packaging and integration with other components was introduced and proposed for the UWB range with gain above 7 dBi and return loss below -10 dB for the whole frequency range. The antenna was characterized not only in the traditional planar form, but also in the case that was flexed in a conformaL-shaped that

mimics the shape of an automobile hood or bumper or the leading edge of an aircraft wing, and the characteristics of the two antenna shapes were compared.

3.1.1 Antenna Design

The proposed antenna was fabricated on a 200 μm thick liquid crystal polymer (LCP) substrate with an 18 μm thick copper layer. The DETSA schematic is presented in Figure 3.1. The length of the board is L=13.62 cm, the width is D=6.64 cm, and the slot gap at the feeding point is 100 μm wide. LCP was preferred because of a number of desirable features.

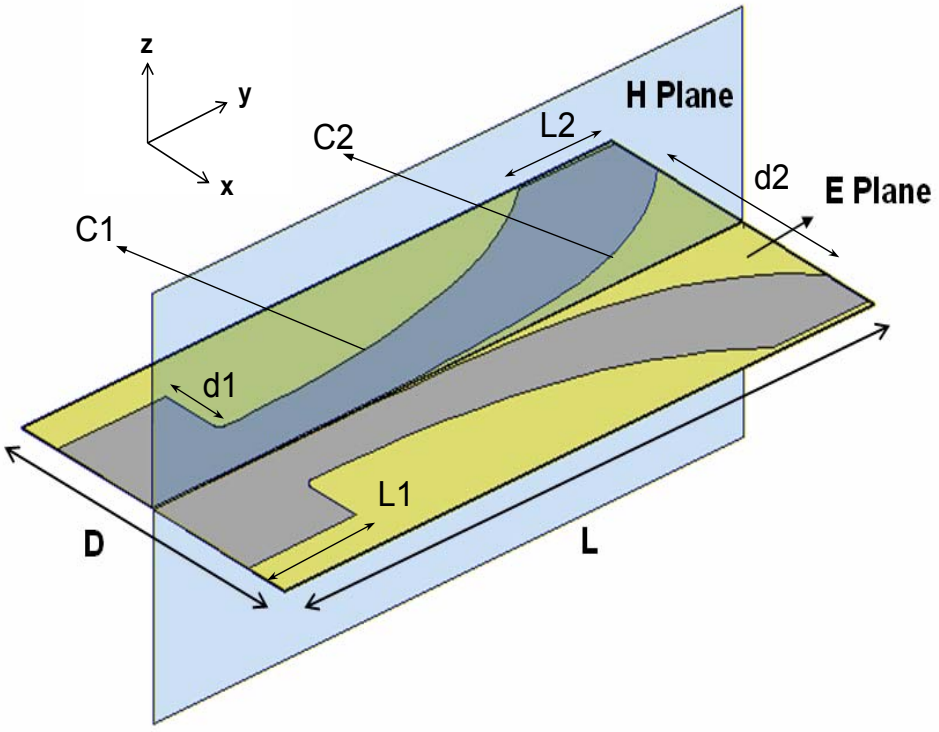

Figure 3.1: DETSA schematic E and H planes are defined.

The dielectric constant ε_r=3.0 is low enough to be used for an end-fire antenna, it has low loss (tanδ=0.002) while being conformal, and it is easy to fabricate with an engineered Coefficient of Thermal Expansion (CTE) [60]. Standard photolithography was used for the fabrication. The design dimensions have been optimized for the antenna to be matched over a frequency range of 3 GHz to 11 GHz. The design parameters are summarized in Table 3.1. For contours C1 and C2, the y variable starts at distance L1 from the edge of the board and is measured in centimeters.

Table 3.1: Dimensions of DETSA.

C1	0.76exp(0.16y) 0<y<8.53 cm
C2	0.012exp(0.48y) 0<y<10.67 cm
d1	12.00 mm
d2	42.92 mm
L1	24.00 mm
L2	21.40mm
D	66.40 mm
L	130.70 mm

3.1.2 Return Loss and Radiation Pattern Measurements

For return loss and radiation pattern measurements, an SMA connector was soldered directly on the slot with no tuning components. The antenna was folded in such a way that the end of the board forms an 18^o angle with the y axis, as shown in Figure 3.2. The contour that describes the projection of the resulted folded antenna surface on the H plane is given by (1) where the y variable is measured in cm and starts at the origin as shown in Figure 3.2.

$$C(y) = -0.0126(y + 1.451y^2 + 0.074y^3)$$
$$0 \le y \le 10.67 \ \ cm \tag{3.1}$$

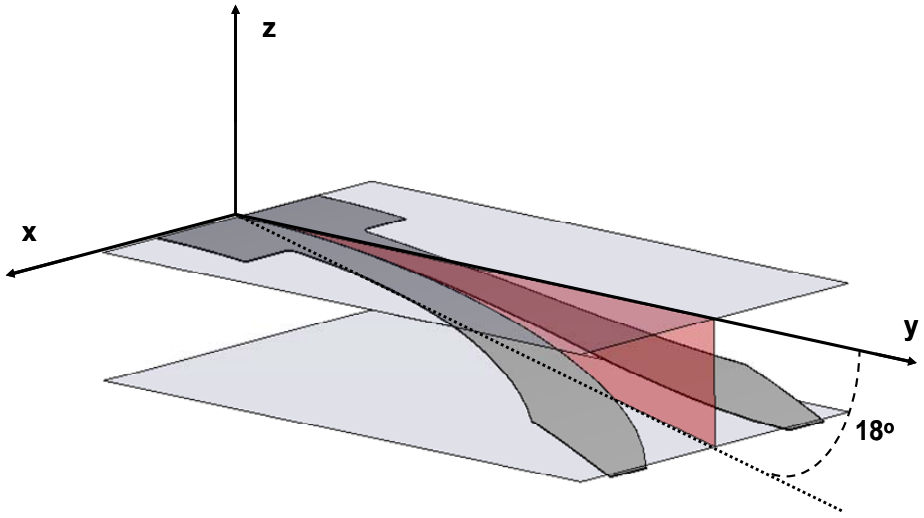

Figure 3.2: Folded DETSA schematic. The antenna is pointing downward at an angle of 18º to the y axis.

Ansoft HFSS 9.0 software [61] was used for the full wave simulations. The simulated and measured return loss is presented in Figure 3.3, where it can be seen that good agreement is achieved between simulated and measured return loss, that there is no difference between flat and folded, conformal, antenna return loss, and the return loss remains below -10 dB in the whole UWB range. The observed "saw" pattern instead of a resonance dominated pattern is expected because the DETSA is a traveling wave antenna with a non-matched termination, not a resonance radiation element. The measured return loss is in agreement with the results in [62]. For the frequencies in the 8 GHz to 10.6 GHz range the return loss is below -15 dB. In those frequencies, relatively higher gain was measured. The planar and folded antennas are shown in Figures 6a and 6b, respectively.

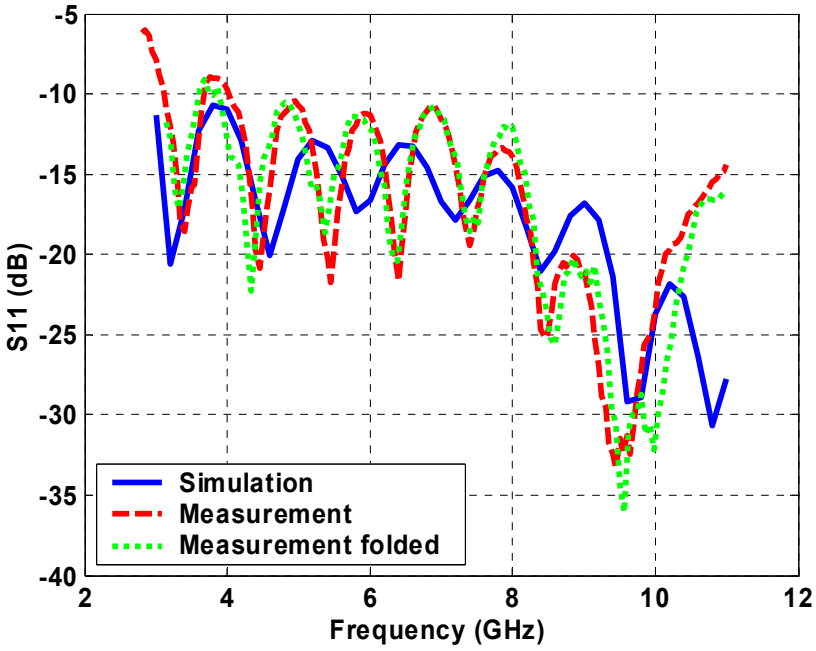

Figure 3.3: Return loss simulation and measurement for planar and folded antenna.

For the radiation pattern diagrams, both near-field and far-field measurements were taken. For all of the measurements, the DETSA was placed between two pieces of 1.5 cm thick styrofoam to give the antenna mechanical support. The styrofoam was cut into the same shape as the DETSA for the conformal antenna. The contour that describes the conformal antenna is a projection on the H plane given by equation (3.1). During characterization of the conformal antenna, the x-z plane at y=0 is located at the SMA connector and the y axis is along the direction of the SMA adapter. Thus, while the E and H plane cut definitions are not changed in the presentation of the results, the DETSA antenna is not in the x-y plane as shown in Figure 3.1. In fact, if a straight line approximation to the conformal antenna is used, the antenna is pointing downward at an angle of 18º to the y axis as shown in Figure 3.2. Despite the unbalanced feeding,

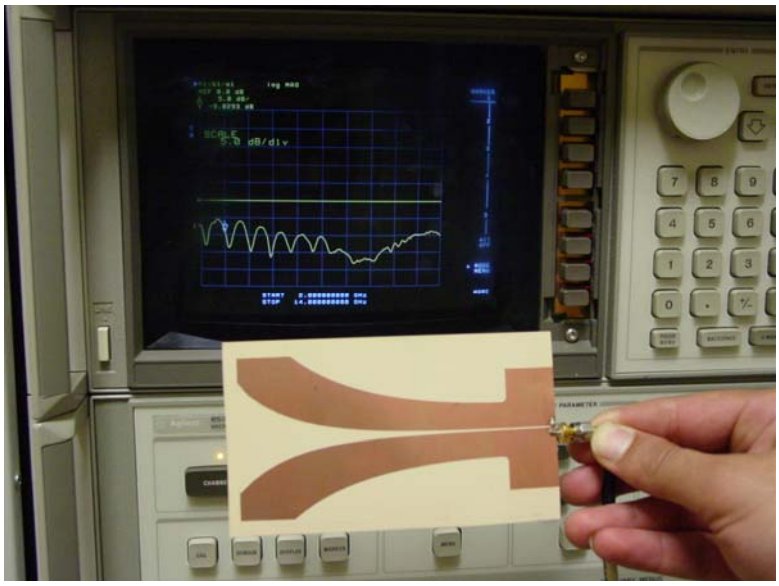

(a)

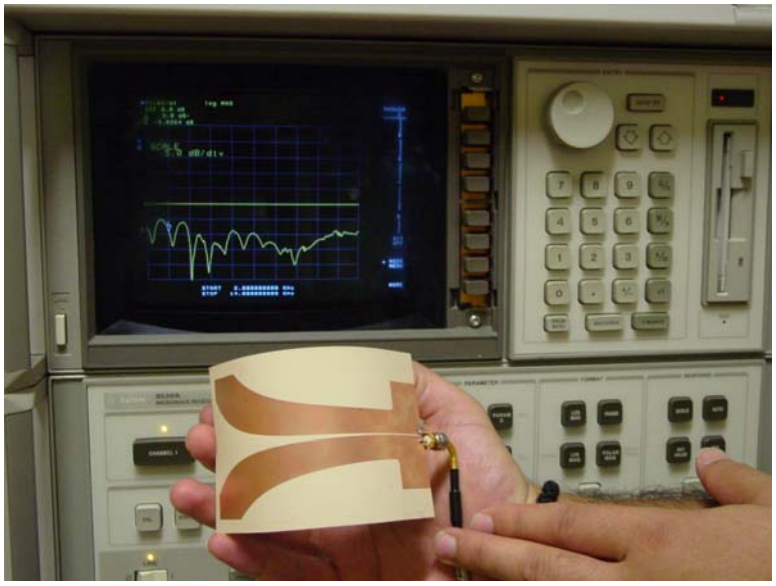

(b)

Figure 3.4: (a) Planar DETSA antenna connected to the HP 8530A Network Analyzer, (b) Folded DETSA antenna connected to the HP 8530A Network Analyzer.

the agreement between the balanced excited simulation and the (unbalanced) measurement is good, as can be seen in Figure 3.5, indicating that the unbalanced feeding does not have any major effect on the radiation patterns.

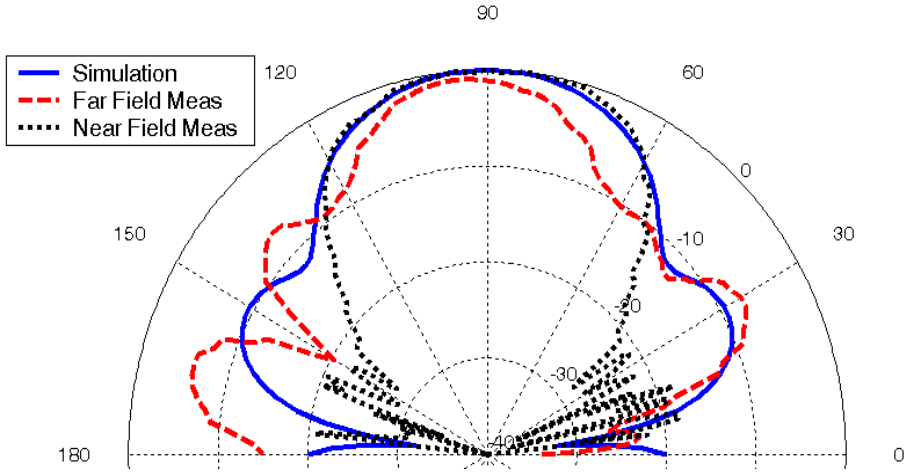

(a)

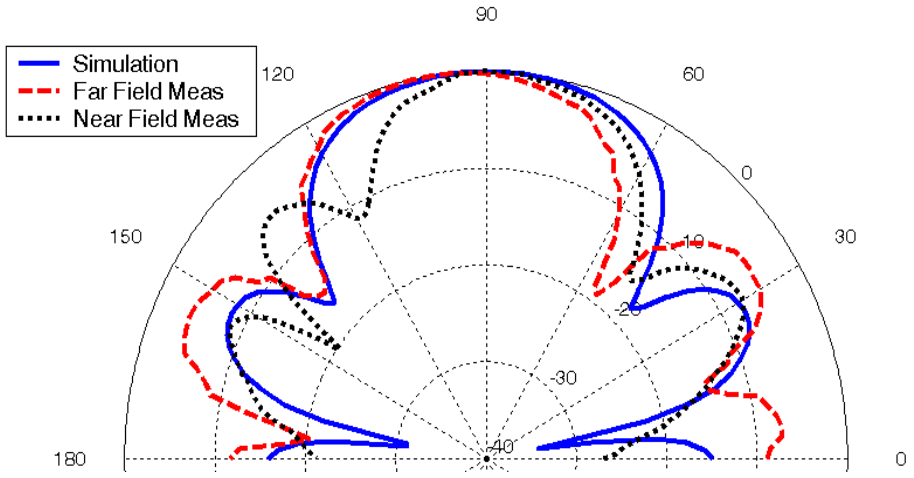

(b)

Figure 3.5: (a) E plane simulation far and near field measurement at f=5 GHz and (b) E plane simulation far and near field measurement at f=5 GHz.

For the near-field measurements, a cylindrical range from Nearfield Systems Inc. was used with an HP8530A microwave receiver. To cover the frequency range of 3 to 12 GHz, four probes, one for each waveguide band, were used. The measured near-field magnitude and phase were transferred to the far field with a 2-D Fourier transform performed by the near-field range software. The maximum scan in the vertical direction was 110 cm, which reduced the accuracy of the system as configured for measuring the DETSA for radiation patterns at angles greater than 62º off axis.

The main problem with wideband antennas is the electrical length variation with frequency, which causes significant distortion in the radiation patterns. Generally, an increase in frequency in end-fire antennas causes the main beam to become narrower (reduced beamwidth) and the directivity to increase. The y axis in Figure 3.1 corresponds to $\varphi=90^{o}$ for the E plane cuts and to $\theta=90^{o}$ for the H plane cuts. The x axis corresponds to $\varphi=0^{o}$ and the z axis to $\theta=0^{o}$. The E and H planes with respect to the antenna and axes orientation can be seen in Figure 3.2.

In Figure 3.5, the far-field and near-field measurements are presented at 5 GHz with the simulated radiation patterns for the planar antenna. There is very good agreement between the measured field patterns from the near- and far-field ranges except for the E plane near-field pattern for angles greater than 60^{o} off axis. This limit in the near-field measurements was already discussed. Furthermore, there is excellent agreement between the simulated and far-field radiation patterns except for small errors in the magnitude of the side lobes.

The wideband behavior of the planar DETSA is shown in Figures 3.6, 3.7, and 3.8 where radiation pattern measurements are presented. The radiation pattern is similar from

4 to 10 GHz. It is also seen that the cross-polarization cuts, labeled H-cross and E-cross, are below -15 dB across the frequency band and below -20 dB at some frequencies. There is a slight asymmetry in the side lobes, especially noticeable in the E-co cuts; it is believed that this is due to the SMA launcher and coaxial cable that was positioned below the antenna or at angles greater than 90º. The asymmetry in the planar antennas is constant with respect to frequency. This overall radiation pattern consistency over a wide frequency band is the major advantage of the DETSA, especially with respect to competitive UWB designs [63], [64]. However, the measured gain varies with respect to frequency, as shown in Table 3.2 which demonstrates that the gain increases linearly with frequency.

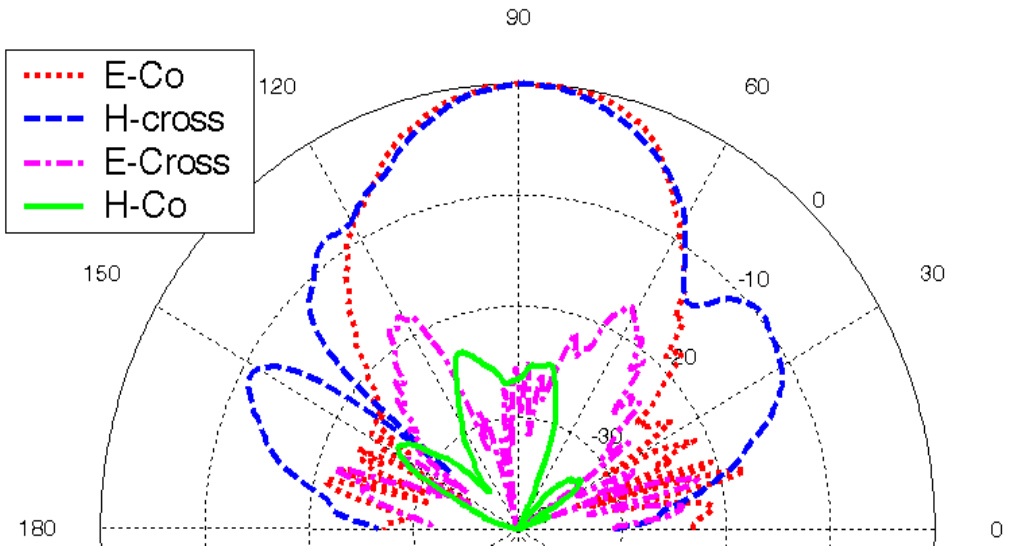

Figure 3.6: Planar DETSA, f=6 GHz.

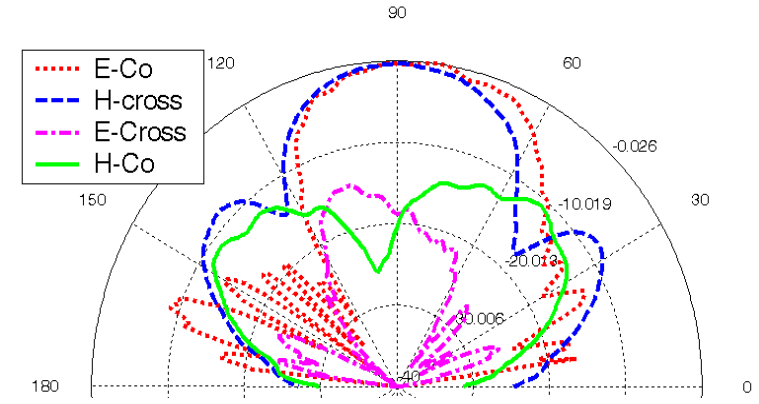

(a)

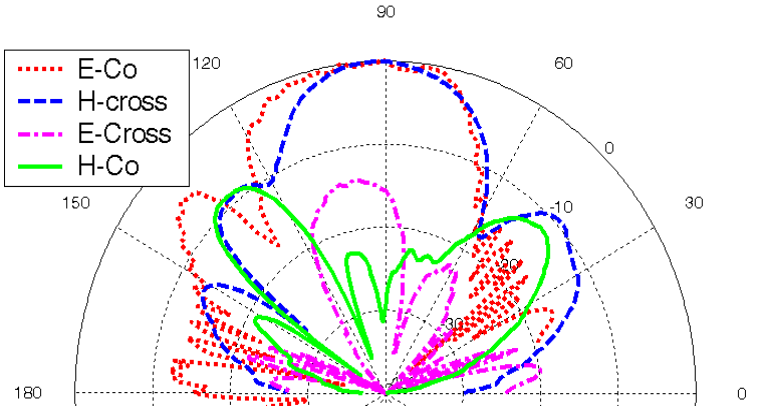

(b)

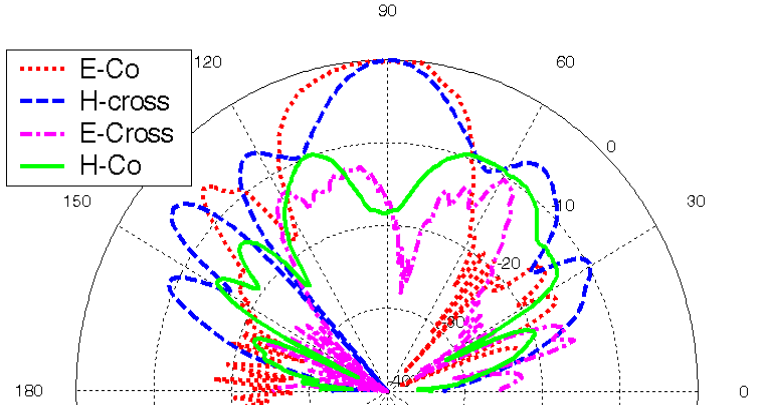

(c)

Figure 3.7: (a) Folded DETSA f=4 GHz, (b) Folded DETSA f=6 GHz, (c) Folded DETSA f=10 GHz.

Table 3.2: Measured gain of planar DETSA

Frequency [GHz]	Gain [dBi]
3	7.4
4	7.8
5	7.0
6	9.8
8	11.9
10	10.6

The applicability of a DETSA fabricated on a very thin, flexible substrate for conformal antennas is also shown in Figure 9. By comparing the planar to the folded DETSA radiation patterns, it is seen that the E-co pattern is nearly identical. As expected, the H-co pattern is pointed toward $\theta > 90^{\circ}$ (downward with respect to the y axis as per (3.1)), because of the folding of the antenna in the H-plane. Furthermore, the pattern is skewed more as frequency increases, and for 10 GHz, the beam points 18º off axis as predicted by the shape of the folded DETSA. There is an increase in the cross-polarization level for the folded DETSA, especially in E-cross and in the direction of the H-co pattern, which agrees with the observations of Lee and Simons for folded tapered slot antennas [65], [66]. Generally, though, the shape of the beam does not vary with folding. This can be verified with an inspection of Figure 3.8, where 3-D patterns are presented. The off-axis field magnitude for the planar antenna is below -20 dB, and it is below -10 dB for the folded antenna for the main beam. This 10 dB increase in off-axis field magnitude and the maximum gain direction, which is directed at $\theta=108^{o}$, are the major effects caused by folding.

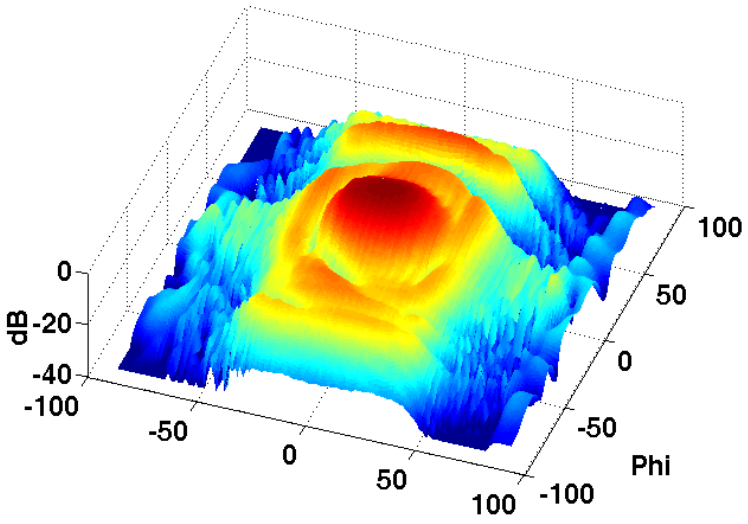

(a)

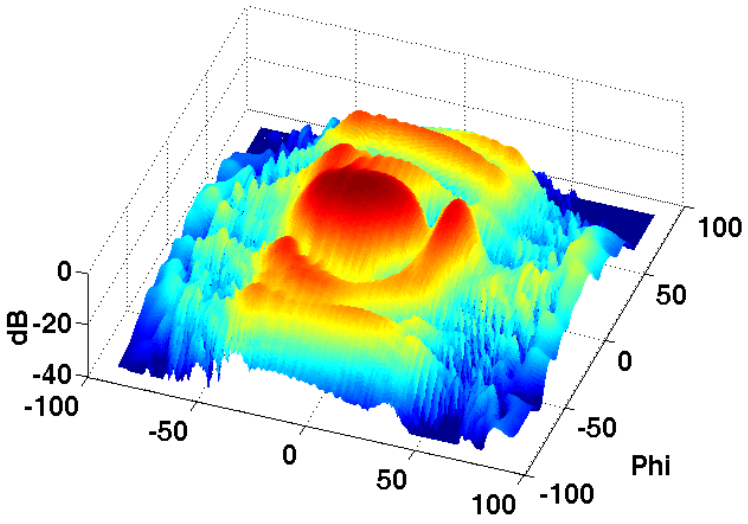

(b)

Figure 3.8: (a) Planar DETSA 3-D pattern f=8 GHz, (b) Folded DETSA 3-D pattern f=8 GHz.

3.1.3 Frequency Domain Measurement for Distortion Estimation

To get an estimate of the effect of the antenna on a transmitted pulse, the setup in Figure 3.9 was used. Two antennas were used, one as a transmitter and the second as a receiver. The two DETSA antennas were aligned with the SMA launcher or y-axis of each antenna pointing at each other, and the distance between them was set at 1.5 m. The minimum far-field distance given from $R=2D^2/\lambda$ was calculated at 0.65 m when D=13.6 cm and λ for 10.6 GHz are used. Both antennas were connected to an HP 8530A network analyzer and S_{21} measurement was taken. The antennas' planes were kept perpendicular to the ground as they appear in Figure 3.4 to avoid the use of mechanical support with styrofoam. The measurement was repeated when both the antennas were identically conformed and the SMA launcher of each still aligned. The whole process took place in a laboratory environment that more realistically resembles an actual communications environment compared to a potential measurement in an anechoic chamber. The measurements are presented in Figure 3.10 for both planar and folded antennas. The misalignment, as a result of the folding, causes higher fading for the higher frequencies (8-10.6 GHz) because of the respective higher directivity and the increasing skew in the radiation pattern with frequency as seen in Figure 3.7. The phase, in both cases, however, remains linear.

The S_{21} measurement represents the transfer function H(f) of a "black box" that consists of the transmitter DETSA, the 1.5 m laboratory environment channel and the receiver DETSA. Any time domain pulse s(t) to be transmitted has a Fourier transform S(f). The pulse detected at the receiver has a Fourier transform R(f)=S(f)H(f). The transmitted pulse s(t) and the received pulse $r(t)=F^{-1}\{R(f)\}$ were correlated to get an

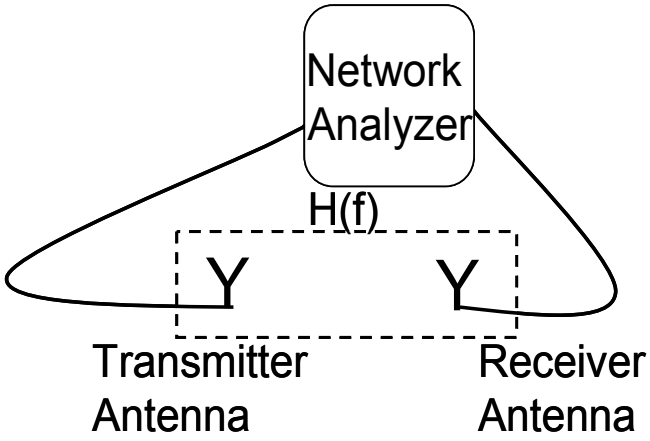

Figure 3.9: Setup for the system: transmitter - channel – receiver, frequency domain measurement.

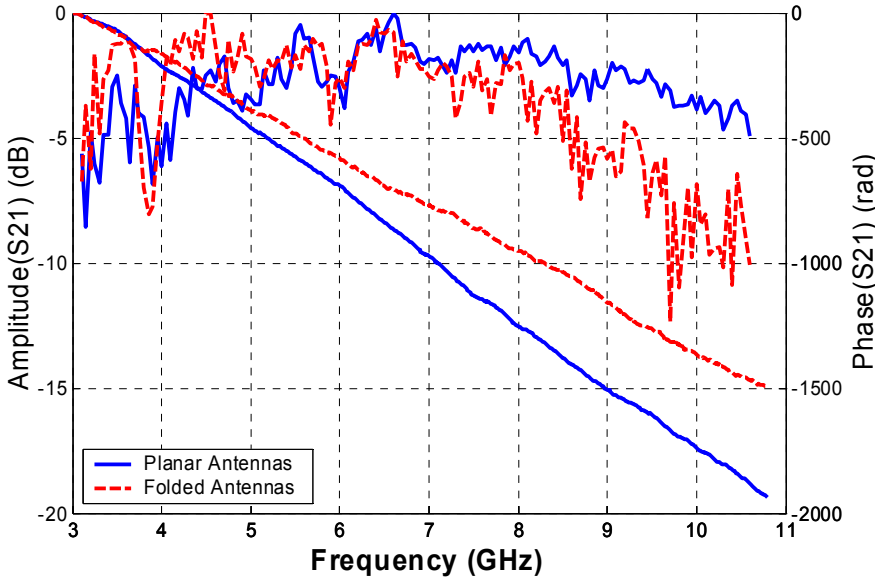

Figure 3.10: S_{21} measurements for the system: transmitter - channel – receiver.

estimation of the distortion added by the DETSA UWB communications system. The distance between the two antennas was long enough to guarantee a far-field measurement and at the same time small enough that it is reasonable to assume that the distortion was caused mainly by the antennas and not by the wireless channel itself. We investigated the effect on an ideal rectangular pulse of duration of 1 ns. The spectrum for a rectangular pulse is mainly concentrated around the dc frequency and goes to zero at n/To where To is the pulse duration that equals to 1 ns, and n $\in$ N. We compare the received pulse with the equivalent time domain pulse that is created when the rectangular pulse baseband spectrum is modulated at (6.85=(10.6+3.1)/2) GHz and filtered from an ideal passband filter with passband range at 3.1-10.6 GHz. The superimposed pulses are presented in Figure 3.11 and very good agreement is observed. The folded antennas caused stronger distortion than the planar antennas, but still the maximum correlation value, estimated with function (2), results in 0.96 for the folded antennas and 0.99 for the planar antennas.

$$Corr(d) = \frac{\sum_i \left[\left(x(i) - m_x \right) \left(y(i-d) - m_y \right) \right]}{\sqrt{\sum_i \left(x(i) - m_x \right)^2} \sqrt{\sum_i \left(y(i) - m_y \right)^2}} \tag{3.2}$$

x(i) and y(i) are the compared waveforms, m_x and m_y are the respected mean values.

The rectangular pulse is an ideal pulse and is not used in practice for any communication systems because of the huge spectrum required. Therefore we used a raised cosine pulse to investigate the same effect. The raised cosine pulse has a spectrum (3.3) that causes zero intersymbol interference (ISI) and is a popular pulse for several modulations. The time domain pulse as a result of the spectrum described by (3.3) is

given by (3.4):

$$H_{rc}=\begin{cases} Ts & 0\le|f|\le(1-a)/2Ts \\ \frac{Ts}{2}\left[1-\sin\frac{\pi Ts}{a}\left(|f|-\frac{Ts}{2}\right)\right] & (1-a)/2Ts\le|f|\le(1+a)/2Ts \\ 0 & (1+a)/2Ts\le|f| \end{cases} \tag{3.3}$$

$$s_{RC}=F^{-1}\{H_{RC}(f)\}=\frac{\sin(\pi t/\mathrm{T}s)}{\pi t/\mathrm{T}s}\frac{\cos(a\pi t/Ts)}{1-4a^2t^2/Ts^2} \tag{3.4}$$

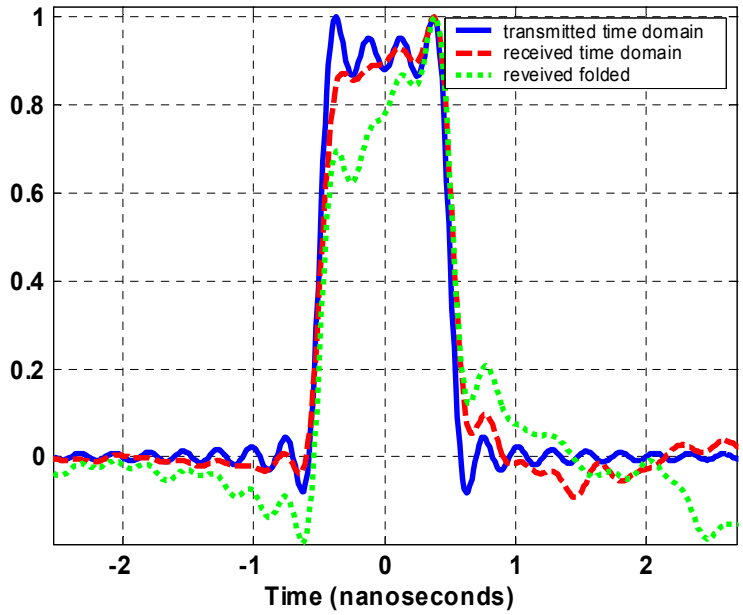

Figure 3.11: Time domain rectangular pulse. The solid line pulse is a rectangular pulse with 7.5 (10.6-3.1) GHz bandwidth that is used as a transmitted pulse. The duration of the pulse is only 1 nanosecond. Small distortion is added by the system: transmitter – channel – receiver.

For the pulse presented in Figure 3.12, Ts = 1/BW was used, where BW=(10.6 – 3.1) GHz and the roll-off factor is α=0.5. The pulse described from the analytical expression (4) is plotted with the normalized inverse Fourier transform of the pulse's spectrum multiplied by the measured H(f), and very good agreement is deduced (Figure 3.9). The maximum correlation value is estimated at 0.98 for the planar antennas and 0.95 for the folded antennas.

The measurement and the mathematical analysis of the data clearly indicated that very little distortion was introduced by the antennas, and the antennas practically did not affect in a destructive way the transmitted pulses. This is mainly due to their broadband performance (3.1-10.6 GHz) and high directivity.

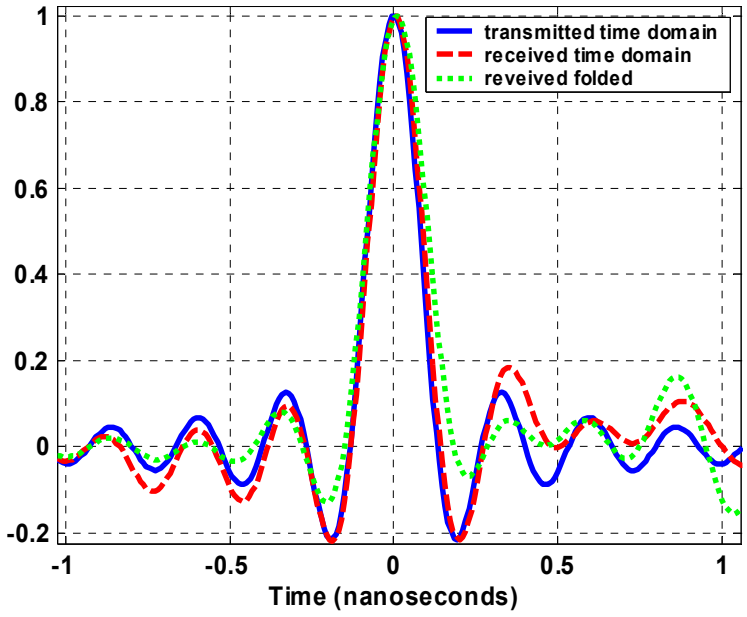

Figure 3.12: Time domain pulse described by (4) superimposed with distorted pulse from both planar and folded antennas. The pulse has theoretically infinite duration because of the confined spectrum but it decays with 1/t.

3.1.4 Summary

A DETSA on a flexible organic material (LCP), suitable for conformal packaging and integration with other components, was introduced and proposed for the UWB range. The measurements agree fairly well with the simulations and this antenna proved to perform well in the whole UWB range. Return loss below -10 dB was measured for the whole frequency range of operation, both when the antenna remained planar and when it was folded. The antenna performed with high gain starting from 7 dBi for low frequencies and up to 12 dBi for the higher frequencies. Near- and far-field measurements in several frequencies covering the whole UWB band indicated that the radiation pattern remained fairly constant and within the specifications for a UWB communications system. Frequency-domain measurements indicated that the antenna, when it was planar or even when it was significantly folded, caused minimum distortion to any transmitted pulse. The antenna on LCP is conformal, can be easily fabricated with relatively low cost, and is a good candidate for a number of UWB applications.

3.2 CPW-fed Elliptical Slot UWB Antenna with a Tuning Uneven U-shaped Stub on Liquid Crystal Polymer (LCP)

The ultra wide band protocol was released in 2002 covering the frequency range from 3.1-10.6 GHz, partly as an attempt to meet the demand for high data rate communications in short distances for mobile and personal applications. Therefore, there is a need for compact-sized, low-cost and high-efficiency antennas with omni-directional radiation patterns. A novel, compact CPW-fed elliptical slot antenna with an uneven U-shaped tuning stub on LCP was proposed to meet these characteristics.

3.2.1 Antenna Design

The fabricated slot antenna is presented in Figure 3.13. It was fabricated on a 350 μm thick, low-loss (tanδ=0.002), low-dielectric constant (ε_r=3), liquid crystal polymer (LCP) with a copper layer that was 18 μm thick. The LCP material is flexible and therefore conformal with an engineered CTE [60]. Standard photolithography was used for the fabrication.

The schematic of the proposed antenna is presented in Figure 3.14 and the dimensions are summarized in Table 3.3 Ansoft HFSS software [61] was used to design the proposed structure and optimize the radiation pattern and return loss. The stub dimensions and the linear tapering affect the matching, while the ellipse size has some effect on the radiation patterns. The proposed antenna is fed by a CPW line with an inner conductor width, W, of 2.2 mm and a gap, g, between the ground and the inner conductor of 0.3 mm. At a distance S=9.9 mm from the board edge, the inner conductor is linearly tapered until its width becomes 0.9 mm to improve the matching between the transmission line and the U-shaped stub. The U-shaped stub consists of a semi-annular ring and two linear segments. The semi annular ring has an outer radius R=5.5 mm and inner

Table 3.3: Elliptical slot antenna dimensions.

D1	40 mm	r	2.5 mm
D2	38 mm	R	5.5 mm
W	2.2 mm	S1	5 mm
g	0.3 mm	S2	6 mm
v	0.9 mm	d	3 mm
S	9.9 mm	L1	30 mm
T	2.5 mm	L2	20 mm
OC	4.1 mm		

radius r=3.5 mm. The left linear segment has length S1=5 mm and width d=3 mm, while the right linear segment has length 6 mm and width d=3mm. The center C of the semi-annular ring is 4.1 mm from the ellipse center O and the ellipse center is 22 mm from the bottom edge. The ellipse has a major axis equal to L1=30 mm and secondary axis equal to L2=20 mm. The overall board dimensions are 40 mm x 38 mm.

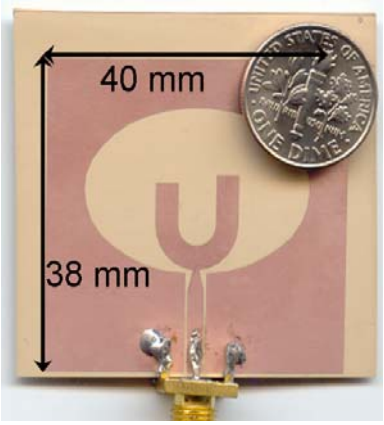

Figure 3.13: Fabricated antenna.

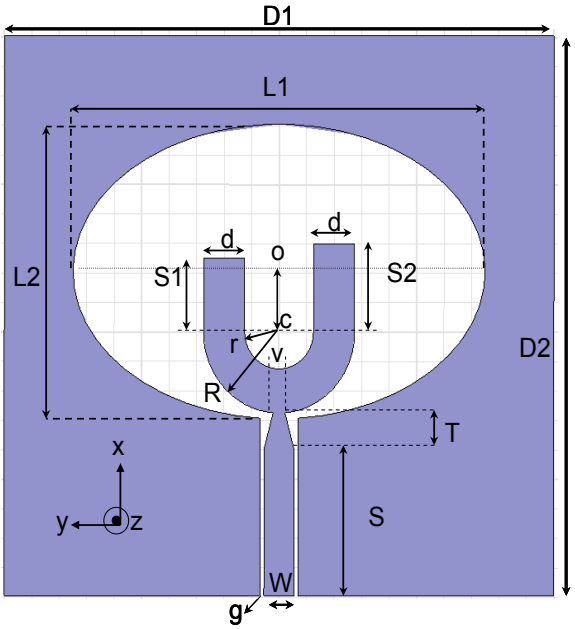

Figure 3.14: Antenna schematic.

3.2.2 Return Loss and Radiation Pattern Measurements

For return loss and radiation pattern measurements, an SMA connector was soldered onto the board. An HP8530 Network Analyzer was used to measure the return loss, which is shown in Figure 3.15 with the simulated return loss. Two main resonances are observed in both the simulated and measured return loss plots, which are controlled by the two linear segments on the U-shaped stub. The simulated return loss is well matched from 3 GHz to over 12 GHz, but the measured return loss is greater than -10 dB only through 10.6 GHz, which is the upper bound for the UWB frequency range.

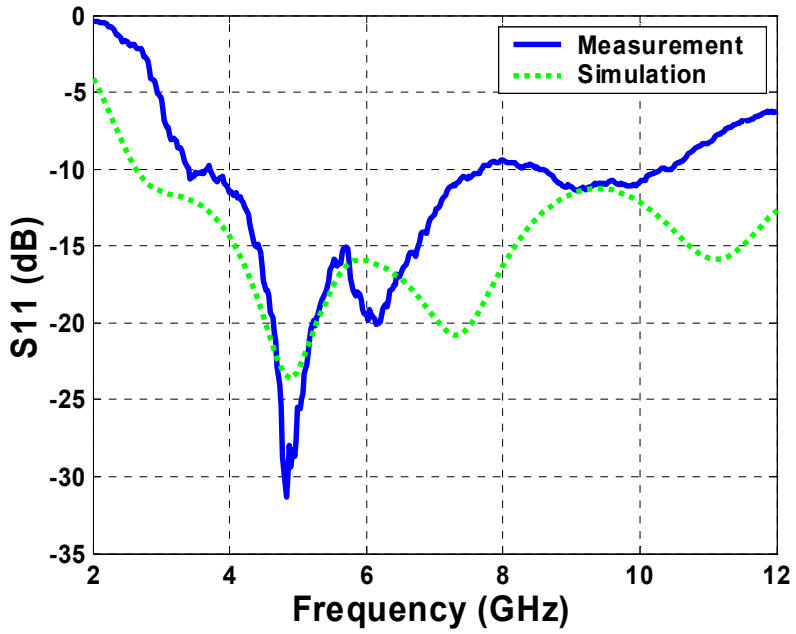

Figure 3.15: Measured and simulated return loss (S11).

Simulated and measured radiation patterns for the slot antenna at 5 and 9 GHz, which are representative of the patterns across the frequency range, are presented in Figures 3.16-3.17. Figure 3.16 presents the E plane (x-z) co-polarization, where $\theta=0^{o}$ corresponds

to z-axis and θ=90^o corresponds to the x-axis. It is seen that the E plane has a null along the x-axis because of the feed line and a pattern that is symmetric around the x-axis. This is a typical monopole radiation pattern. The H plane (y-z) co-polarization plots are presented in Figure 3.17, where θ=0^o is the z-axis and θ=90^o is the y-axis. It is seen that the H plane patterns are almost perfectly omni-directional at 5 GHz, but at 9 GHz, the slot antenna H-plane pattern flattens along the y-axis. The measured gain presented in Figure 3.18 remained higher than 2 dBi, thus exceeding the usual performance of most of the UWB antennas reported in the literature.

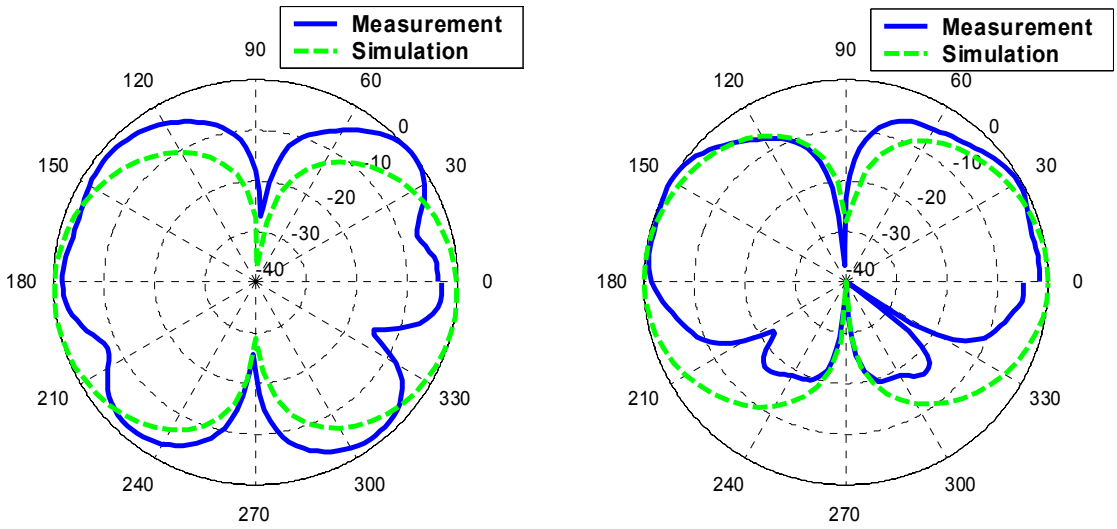

(a) (b)

Figure 3.16: (a) E plane at 5 GHz, (b) E plane at 9 GHz.

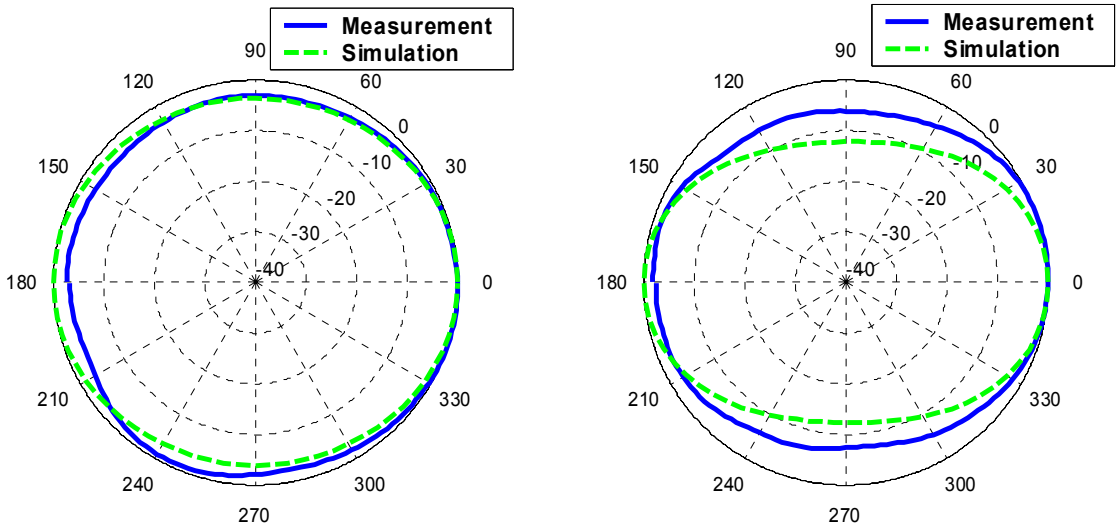

(a) (b)

Figure 3.17: (a) H plane at 5 GHz, (b) H plane at 9 GHz.

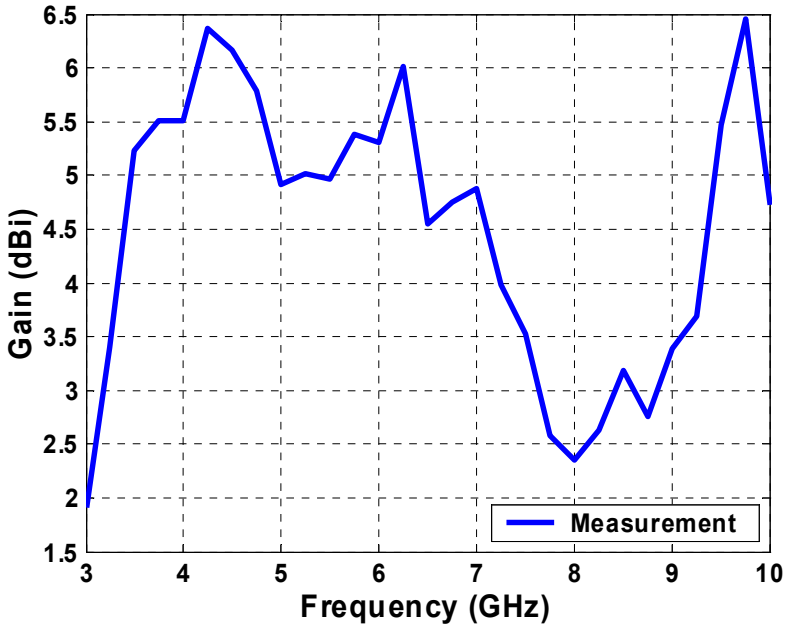

Figure 3.18: Gain measurement.

3.2.3 Summary

The proposed antenna was fabricated on flexible, low loss and low cost LCP material. The presented slot antenna had return loss better than -10 dB in the whole UWB range and had omni-directional radiation patterns. It exhibited relatively high gain, and the measured radiation patterns maintained the omni-directional characteristic in all frequencies in the UWB range. The aforementioned characteristics make the CPW-fed elliptical slot antenna with an uneven U-shaped tuning stub a very good candidate for mobile personal communication devices

3.3 Cactus-shaped UWB Monopole Antenna

The need for compact-sized, low-cost and high-efficiency antennas with omni-directional radiation patterns increases constantly. The combination of these characteristics in a wide frequency range such as the UWB band is a challenging problem and several design concepts have been used in an attempt to provide a satisfactory solution. Two novel cactus-shaped monopole antennas were implemented. The final, optimized design covered less than 40 % of the area occupied by the CPW-fed elliptical slot antenna with an uneven U-shaped tuning stub.

3.3.1 Big Ground Cactus-shaped Monopole Antenna Design

The big ground cactus-shaped monopole was fabricated on a 225 μm thick LCP substrate and standard photolithography was used. The size reduction of the cactus antenna compared to the slot antenna presented in the previous section is obvious from Figure 3.19, where the fabricated prototype is compared in size with a coin. The schematic of the compared antenna is presented in Figure 3.20 and the dimensions are summarized in Table 3.4.

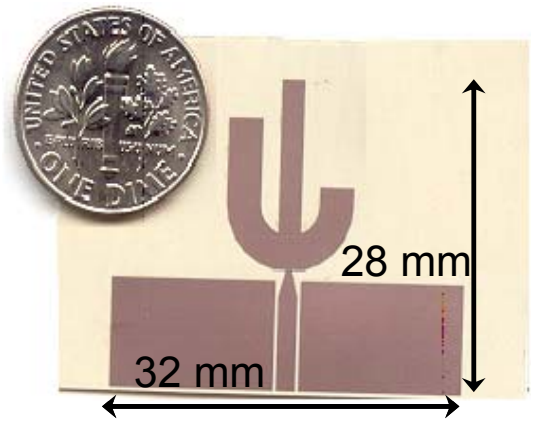

Figure 3.19: Fabricated big ground cactus-shaped monopole UWB antenna.

The improved iteration of the cactus antenna was based on the observation that most of the radiated energy for the CPW-fed slot antenna was confined on the tuning stub. Therefore, a design was attempted without the elliptical slot. Impedance matching over the entire UWB range was impossible with only two linear segments, and to overcome this problem, a third linear segment was added in the feed line direction. The thinner LCP substrate used for the cactus antenna and the addition of the middle linear segment required the linearly tapered transition and the semi-annular segment re-optimization. Consequently, for the cactus antenna, the CPW center conductor width W is 1.78 mm and length d2 is 7.92 mm. A linear taper is used to reduce the center conductor width to d=0.61 mm and is connected to the cactus-shaped stub at distance d1=10.24 mm from the board edge. The two rectangular ground patches have dimensions Gl x Gw, which correspond to 9.44 mm and 14.89 mm respectively. For the primary radiator, a cactus-shaped stub is used. It consists of a semi-annular ring with inner radius r=2.60 mm, an outer radius R=5.72 mm, and three linear segments of different lengths. The middle linear segment is L2=13.00 mm long and W2=2.08 mm wide, while the left and right

segments are L1= 7.28 mm and L3=1.56 mm long, respectively. Both of them are 3.12 mm wide. From the bottom part of the semi-annular ring, a circular sector is detached leaving a chord of length S=2.73 mm. The overall board dimensions for the cactus antenna are 32 mm x 28 mm, resulting in a 40% reduction in area compared to the CPW-fed slot.

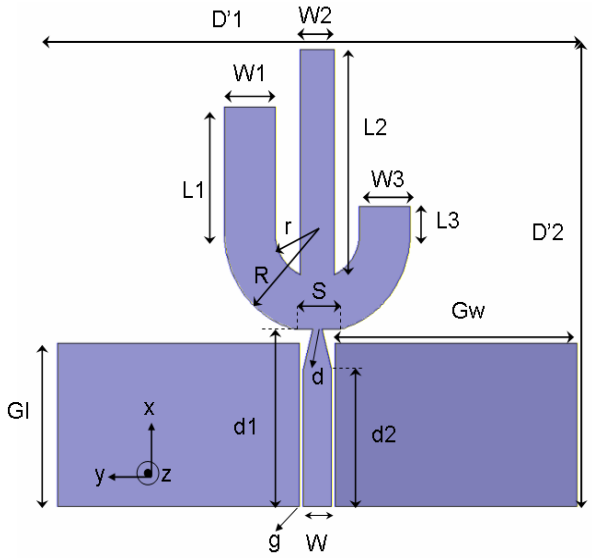

Figure 3.20: Cactus-shaped monopole schematic.

Table 3.4: Big ground cactus antenna dimensions.

D'1	32.00 mm	L1	7.28 mm
D'2	28.00 mm	L2	13.00 mm
Gl	9.44 mm	L3	1.56 mm
Gw	14.89 mm	W1	3.12 mm
d1	10.24 mm	W2	2.08 mm
d2	7.92 mm	W3	3.12 mm
R	5.72 mm	S	2.73 mm
R	2.60 mm	d	0.61 mm
		W	1.78 mm

3.3.2 Return Loss and Radiation Pattern Measurements

For return loss and radiation pattern measurements, an SMA connector was soldered onto the board. An HP8530 Vector Network Analyzer was used to measure the return loss. The simulated and measured return loss for the miniaturized cactus antenna is presented in Figure 3.21.

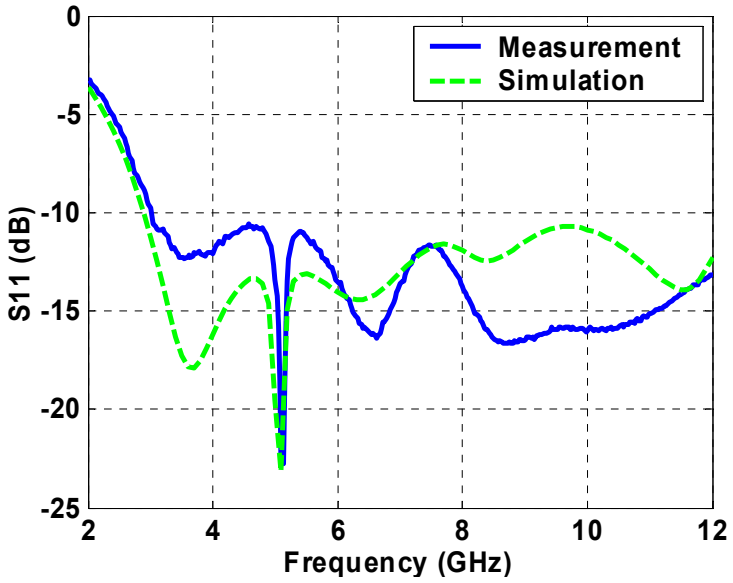

Figure 3.21: Measured and simulated return loss.

The cactus-shaped monopole presents a -10 dB return loss from 2.9 GHz to 12 GHz that overlaps the designated UWB range. Three resonances dominate the return loss, at 3.7, 5.1, and 6.4 GHz one for each linear segment. Generally, the longer the stub is the lower the corresponding resonance appears. This can be seen in Figure 3.22a, where the simulated S11 is plotted for four different length values (L3) of the shortest linear segment. The shortest linear segment controls the higher frequency (6.4 GHz) and the

previously mentioned trend is verified. The matching at the higher frequencies is controlled by the rectangular ground patch's width Gw as can be seen in Figure 3.22b where S11 is plotted for four different Gw values. It is obvious that the width of the ground patch cannot be smaller than 14.89 mm without compromising the matching in higher frequencies, although it would be highly desired for an even more compact design.

For the presented S11 plots there is a small discrepancy between the simulated and measured results. This is partly due to the fact that the UWB range is large compared to the central frequency and is difficult for the simulation tools to give accurate results over the whole band. Moreover there are losses at the connector that cannot be simulated, which cause some additional inconsistency.

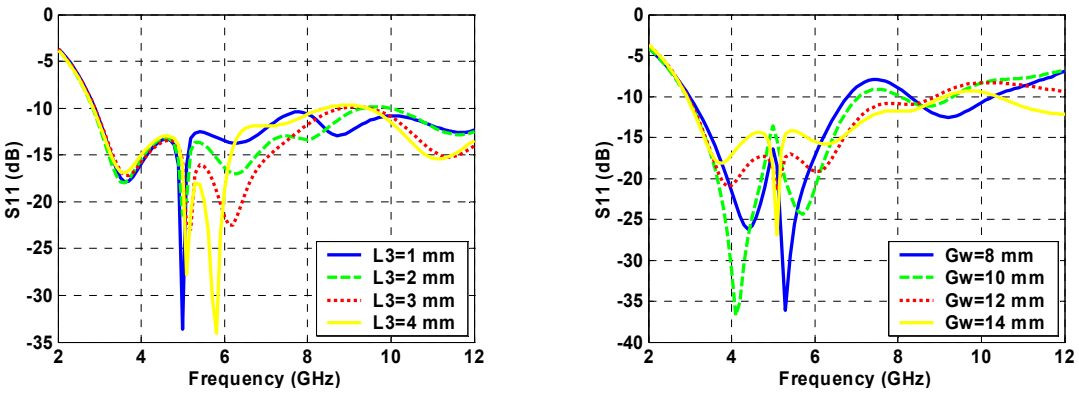

(a) (b)

Figure 3.22: (a) Cactus antenna S11 with L3 variation, (b) Cactus antenna S11 with Gw variation.

Simulated and measured radiation patterns for the big ground cactus-shaped monopole at 5 and 9 GHz, which are representative of the patterns across the frequency range, are presented in Figures 3.23-3.25. Figure 3.23 presents the E plane (x-z) co-polarization, where $\theta=0^o$ corresponds to z-axis and $\theta=90^o$ corresponds to the x-axis. It is

seen that the E plane has a null along the x-axis because of the feed line and a pattern that is symmetric around the x-axis. The H plane (y-z) co-polarization plots are presented in Figure 3.24, where $\theta=0^o$ is the z-axis and $\theta=90^o$ is the y-axis. It is seen that the H plane patterns for the proposed antenna are almost perfectly omni-directional at both 5 GHz and 9 GHz.

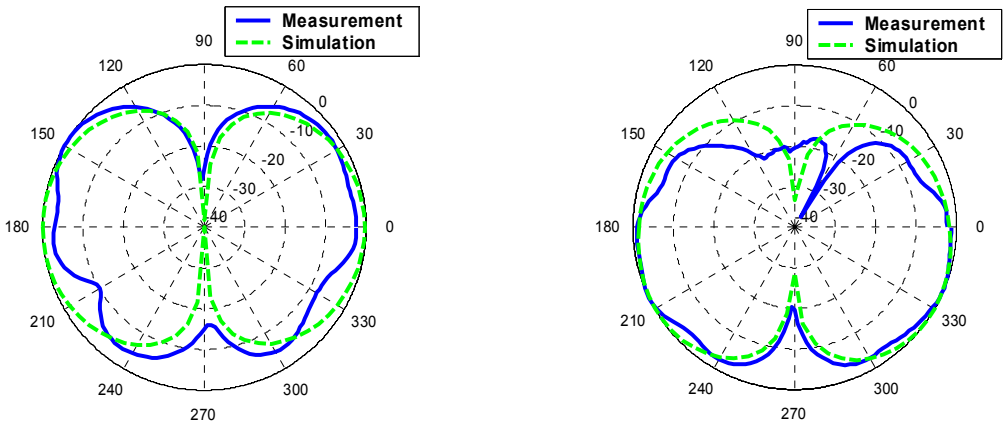

(a) (b)

Figure 3.23: (a) E plane at 5 GHz, (b) E plane at 9 GHz.

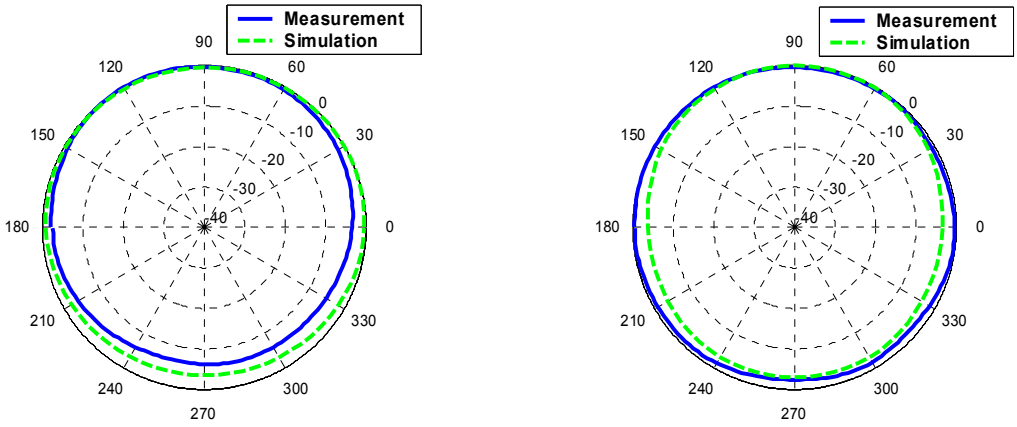

(a) (b)

Figure 3.24: (a) H plane at 5 GHz, (b) H plane at 9 GHz.

The measured and simulated gain is presented in Figure 3.25. The gain that was measured in the z-axis direction was considerably lower than the gain measured for the U-shaped stub slot antenna and this is because the cactus-shaped monopole was more omni-directional than the competitive slot antenna, but at the same time it remained 40% smaller.

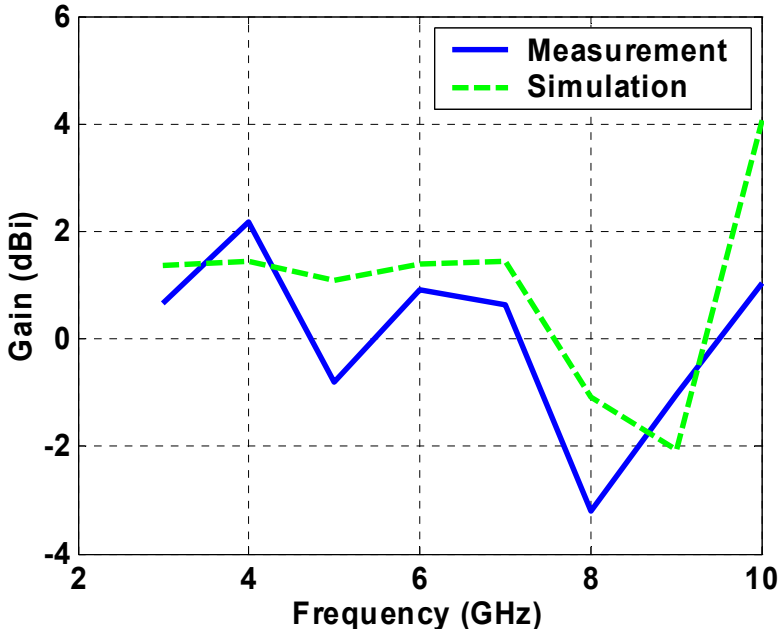

Figure: 3.25. Measured and simulated gain.

3.3.3 Small Ground Cactus-shaped Monopole Antenna Design

The small ground cactus-shaped monopole antenna was fabricated on 225 µm thick LCP with overall board dimensions of 20 x 28 mm^2, covering less than 40% of the area required for the slot antenna and less than 65% of the area required for the big ground cactus-shaped monopole. The 250 µm thick substrate was acquired after two 100 µm thick substrates were stacked and thermo bonded using one 25 µm thick, lower

temperature melting point LCP as a bonding layer between the two 100 μm thick samples. Standard photolithography was used. The fabricated prototype is presented in Figure 3.26.

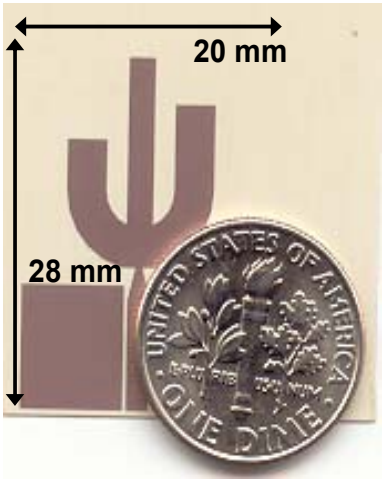

Figure 3.26: Fabricated small ground cactus-shaped monopole.

The antenna consists of a CPW line with a linearly tapered transition that is terminated with a semi-annular ring with two uneven linear segments and an additional linear segment in the direction of the feed line. The central CPW line conductor has width T=1.79 mm; at distance H1=7.92 mm it is linearly tapered down to t=0.60 mm and is terminated with the cactus-shaped monopole. The linearly tapered segment that is used for improved matching is terminated at a distance H2=10.24 mm from the board edge. From the bottom part of the semi-annular ring that terminated the tapered feed line a circular sector is detached, leaving a chord of length C=2.73 mm. Two rectangular patches with dimensions 9 x 8 mm^2 are used as the CPW line ground. The cactus monopole consists of a semi-annular ring with inner radius r=2.60 mm and outer radius R=5.72 mm. The left linear segment has length L1=3.50 mm and width W1=3.12 mm, while the right linear stub has length L3=6.50 mm and W3=3.12 mm. The middle stub's

length is L2=12 mm and its width is W2=2.08 mm. The overall LCP board dimensions are only 20 x 28 mm^2. The antenna schematic is presented in Figure 3.27 and the schematic dimensions are summarized in Table 3.5.

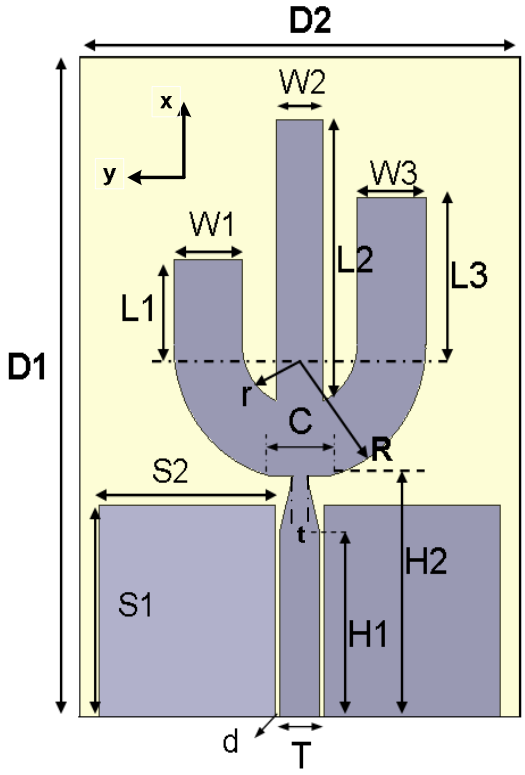

Figure 3.27: Antenna schematic.

Table 3.5: Schematic dimensions in (mm).

D1	28.00	L1	12.00
D2	20.00	L2	3.50
S1	9.00	L3	6.50
S2	8.00	W1	3.12
H1	7.92	W2	2.08
H2	10.24	W3	3.12
T	1.79	R	5.72
t	0.60	r	2.60
C	2.73		

3.3.4 Return Loss and Radiation Pattern Measurements

The measured return loss is presented in comparison with the simulated results in Figure 3.28. The proposed antenna was designed and optimized using Ansoft HFSS. Three resonances can be seen in the return loss, each one controlled primarily by the length of the three linear segments. A resonance in the return loss is created at the frequency at which the length of the linear segment is approximately λ/4. The appropriate distribution of the three resonances within the UWB frequency range, in combination with the size of the ground and the feed line tapering, match (return loss below -10 dB) the cactus antenna from 2.9 GHz to 11.8 GHz, which overlaps the UWB range (3.1-10.6 GHz).

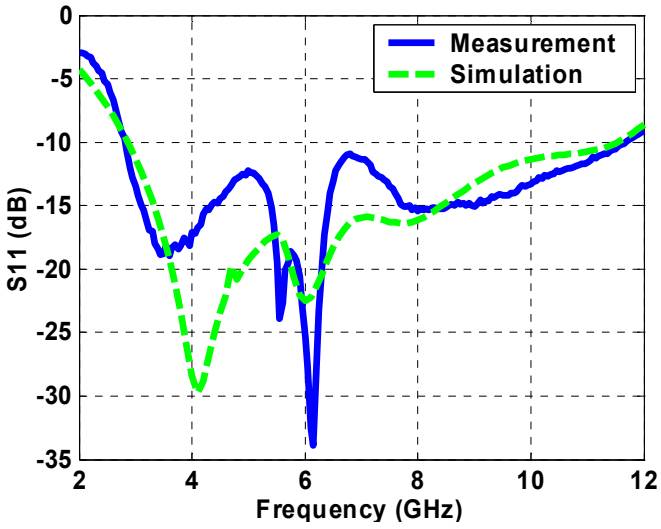

Figure 3.28: Measured and simulated return loss.

In Figure 3.29 the effect of the length of the linear stubs and the width of the ground patches on the return loss is studied through a parametric analysis. If the width of the ground patch S2 gets smaller, the antenna cannot be matched satisfactorily at the lower frequencies, as can be seen in Figure 3.29a (dashed line), while making the ground patch wider causes a similar mismatch at the higher frequencies (dotted line). In all four plots in

Figure 3.29 the contour with the solid line presents the optimized simulation results. Figure 3.29b demonstrates the influence of the shortest stub's length in the position of the higher resonance. Generally the longer the stub is, the lower the resonance shifts and this is a consistent behavior that can be verified with all three plots presented in Figures 3.29b, 3.29c and 3.29d. One of the issues that evolves with the resonances distribution approach is the collapse of a resonance, which can be seen for L1=4.5 mm (dotted line) where the middle resonance is suppressed by the other two. Suppressing a resonance can generally cause mismatch problems (peak in the S11 contour) in the frequency range where the resonance previously existed. A similar problem can be caused when the resonances are too far from each other, which is the case in Figure 3.29c for L2=14 mm. This causes the first resonance to shift lower than 4 GHz, which results in a peak between the shifted first resonance and the second one at 5.9 GHz. The mismatch peak is more intense in Figure 3.29d for L3=4 mm (dashed line) when the second resonance shifts (higher) far from the first one and eventually collapses by merging with the third one. The resulting peak appears at 6 GHz and significantly affects the antenna matching. The importance of the ground patches can be deduced from the observation that the size of the ground patches affects the position and the depth of the three resonances, which change significantly when the S2 parameter changes. On the other hand, when the length of one of the stubs changes, it does not directly affect the position or the depth of the other resonances. Although the length of a certain stub directly affects only one resonance, the cactus-shaped radiator and the ground patches must be designed and optimized as a single object in whole, to achieve good matching. This is why the length of the used stubs, and

therefore the position of the resonances on the presented return loss, is different than the reported S11 for the cactus-shaped monopole with the relatively bigger ground.

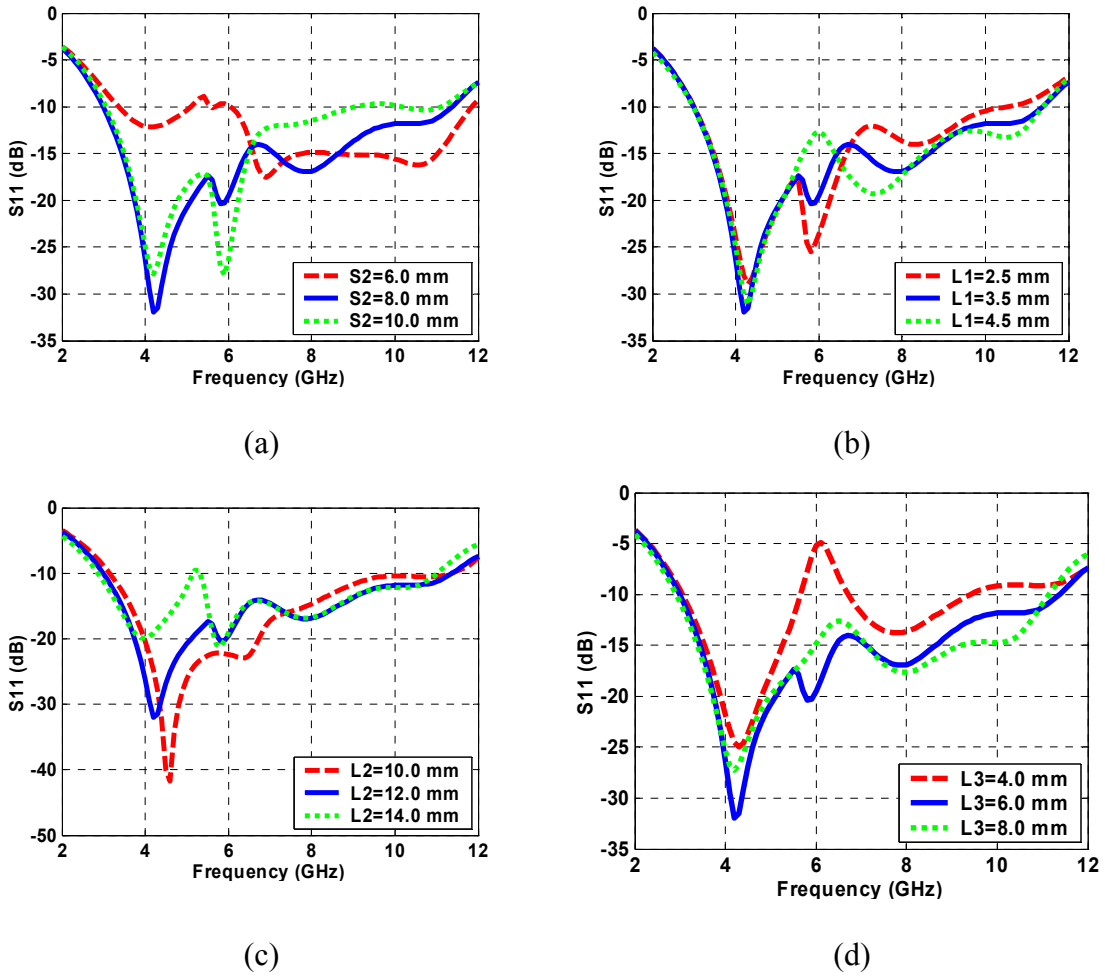

Figure 3.29: Simulated parametric study for the design parameters effect on the return loss. (a) Ground effect, (b) Smallest stub effect, (c) Largest stub effect, (d) Middle stub effect.

The electric field distribution on the cactus-shaped monopole is presented in Figure 3.30. With the chosen representation, the stronger the field is the brighter the used tone is. Consequently it is obvious that most of the radiated power at 4.2 GHz is emitted from the middle stub, while for 5.9 GHz the right stub radiates most of the power. For the radiation of the higher frequency for which a resonance occurs at 8 GHz, the shortest stub on the left is mostly responsible.

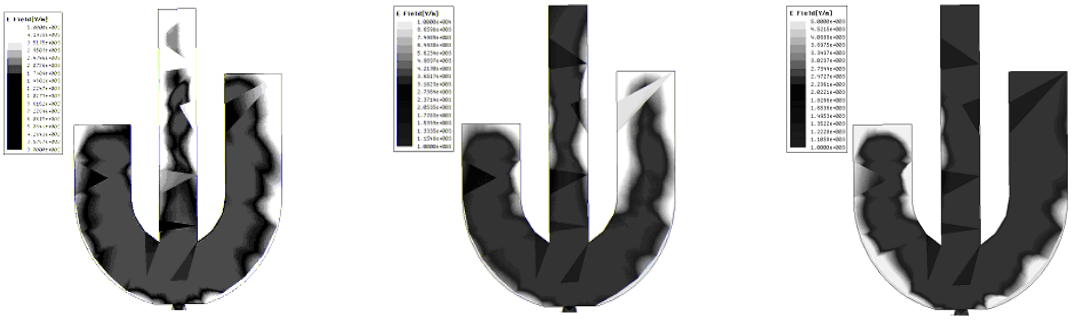

a b c

Figure 3.30: Electric field distribution at (a) 4.2 GHz, (b) 5.9 GHz and (c) 8 GHz.

The cactus-shaped antenna demonstrates typical monopole radiation patterns at the E plane and omni-directional patterns in the H plane. The simulated and measured patterns at 4, 8, and 10 GHz in the E and H planes are presented in Figure 3.31. The patterns retain a consisting shape throughout the UWB range. Relatively good agreement between the simulation and measurement is observed. Based on the antenna orientation with respect to the axes in Figure 3.27 the E plane is the x-z plane and the H plane is the y-z plane. For both cuts, $\theta=0^{o}$ corresponds to the z-axis, while $\theta=90^{o}$ corresponds to x-axis and y-axis for E and H planes, respectively.

The antenna gain was measured by using the substitution method with an antenna of known gain, in this case a 2 to 18 GHz, Q-par Angus Ltd horn antenna. The "known" gain of the Q-par antenna is specified to be accurate to within ±0.8 dB; thus, this becomes the accuracy of the gain measurements presented in this section. The gain was measured in the z-axis direction and is presented in Figure 3.32. The omni-directional patterns retain the gain low, and the gain varies only within 4 db in the whole range. Other than a deep at 6 GHz

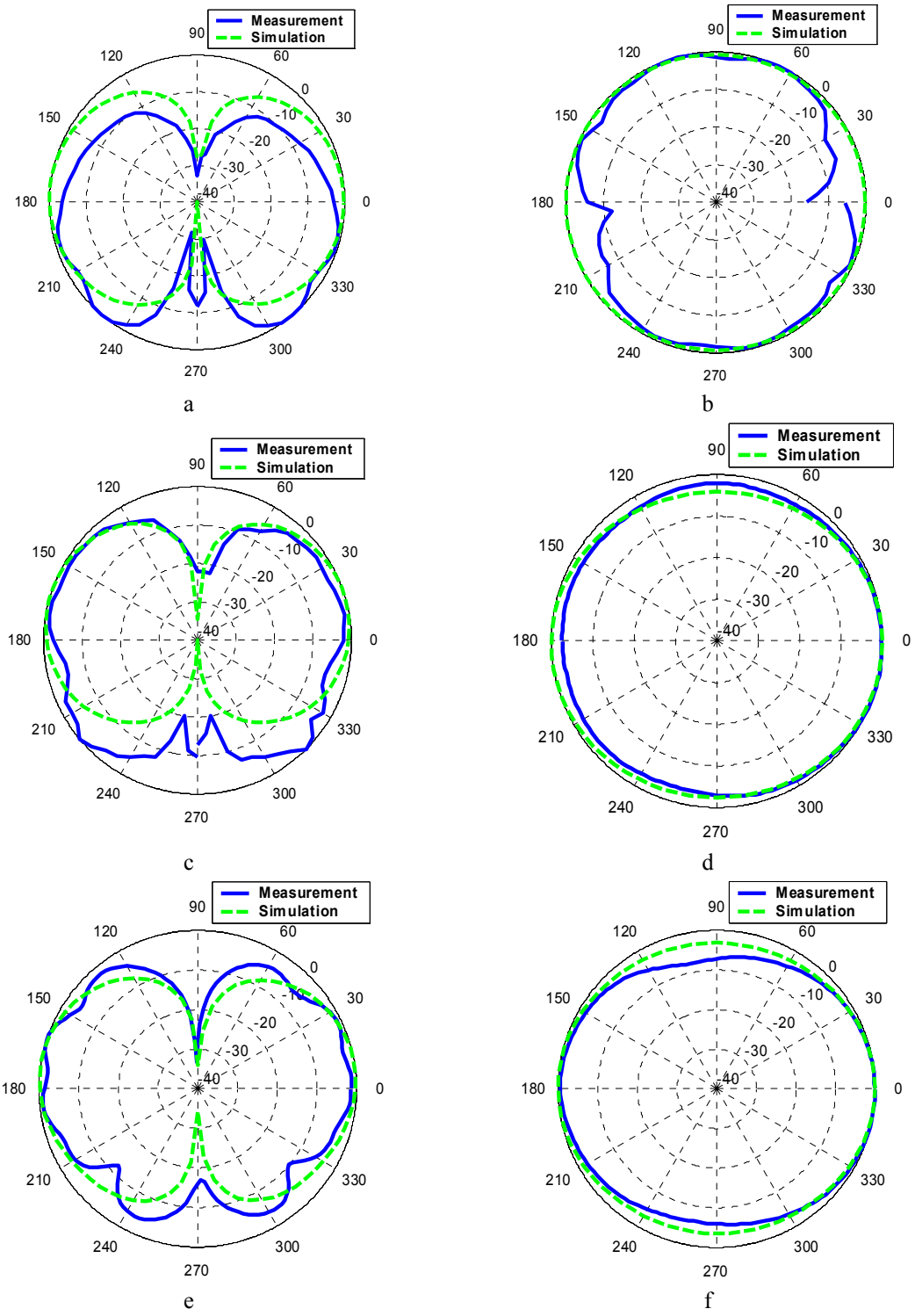

Figure 3.31: Simulated and measured radiation patterns. (a) E plane 4 GHz, (b) H plane 4GHz, (c) E plane 8 GHz, (d) H plane 8 GHz, (e) E plane 10 GHz, (f) H plane 10 GHz.

the gain seems to increase linearly with respect to the frequency, and relatively good agreement is demonstrated between the simulated and the measured results.

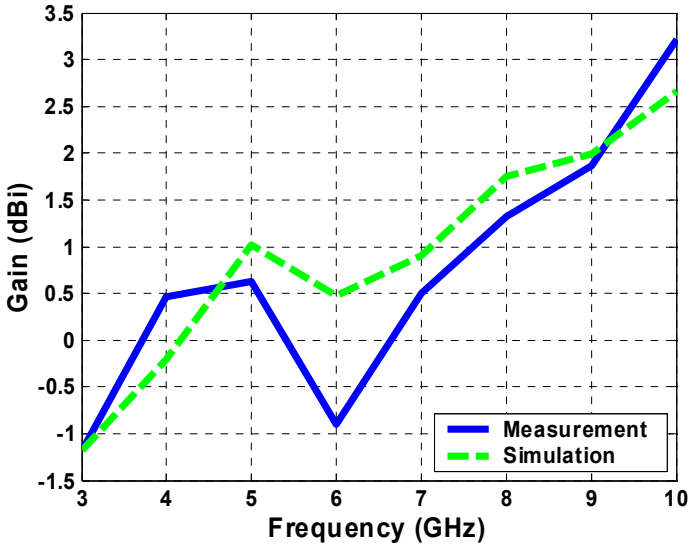

Figure 3.32: Measured and simulated gain in z-axis direction.

3.3.5 Summary

Two novel compact, CPW fed, UWB cactus-shaped monopoles were presented, with good matching in a frequency range from 2.9 GHz to 11.8 GHz, and consistent omni-directional patterns throughout the desired frequency range. The optimized prototype had overall board dimensions only 20 x 28 mm^2 covering less than 40% of the area covered by the original design of the elliptical slot antenna. The analyzed operation principles allow a direct control on the return loss by shifting the position and controlling the depth of the observed resonances. The aforementioned characteristics make the presented antenna a potential candidate for reconfigurable "smart" UWB transceivers for mobile personal communication devices, which will operate in desired UWB sub-bands, according to the specifications of the application.

3.4 Compact Ultra Wide-Band (UWB) CPW-fed Elliptical Monopole on Liquid Crystal Polymer (LCP)

The implementation of a compact CPW-fed elliptical monopole antenna that demonstrates good impedance match and omni-directional radiation patterns in the whole ultra wide band range (UWB) is discussed in this section. The proposed antenna was fabricated on 100 μm thick liquid crystal polymer (LCP) with an overall board dimension of 32 mm x 30 mm. The elliptical monopole antenna is the preliminary design for the implementation of a UWB antenna with reconfigurable band rejection characteristic. The final goal is to implement an antenna which will use switches to reject the received radiation in the frequency band used for WLAN applications.

3.4.1 Antenna Design

The proposed antenna was fabricated on a 100 μm thick LCP substrate. The copper layer was only 3 μm thick and it was sputtered onto the LCP substrate. The compact CPW-fed elliptical monopole schematic is presented in Figure 3.33. The overall size is very small. The length of the board is S1=32 mm and the width is S2=30 mm. It is fed by a CPW line where the central conductor width (W) is 2.94 mm and the slot gaps are s=100 μm wide. The CPW line is linearly tapered to improve the matching of the elliptical radiator to the feeding line. At a distance L2=6.10 mm, the central conductor is linearly tapered down to w=0.85 mm at the point where the line connects to the elliptical radiator. Both ground planes are also tapered linearly in such a way so that the lower side is H2=11.50 mm while the opposite side is H1=12.07 mm. The ground length is only D=9.60 mm. Finally the elliptical radiator has major axis A= 9 mm and secondary axis B=6.75 mm with a ratio B/A=0.75. LCP was preferred because of its low dielectric constant (ε_r=3), low loss

(tanδ=0.002), and the fact that it is suitable for conformal antennas and easy to fabricate with an engineered CTE [60]. Standard photolithography was used for the fabrication. The design dimensions have been optimized in order for the antenna to be matched over a frequency range of 3 GHz to 10 GHz. The antenna schematic dimensions are summarized in Table 3.6.

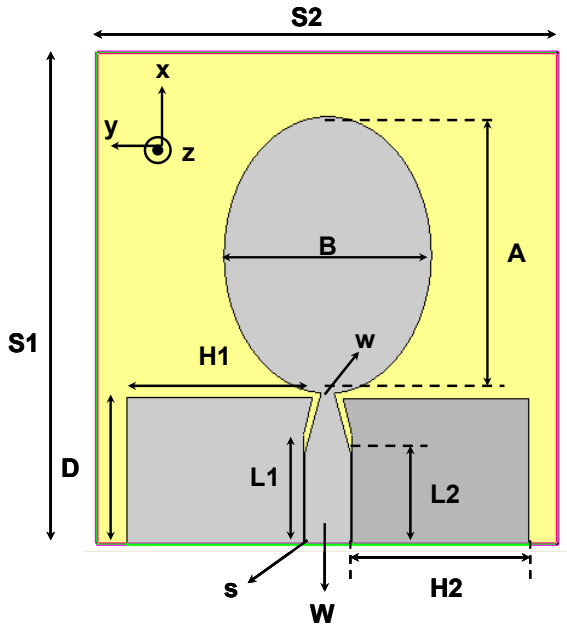

Figure 3.33: Antenna schematic.

Table3.6: Elliptical monopole dimensions.

S1	32.00 mm	B	6.75 mm
S2	30.00 mm	w	0.85 mm
D	9.60 mm	W	2.94 mm
L1	7.23 mm	s	0.10 mm
L2	6.10 mm	H1	12.07 mm
A	9.00 mm	H2	11.50 mm

3.4.2 Return Loss and Radiation Pattern Measurements

For return loss and radiation pattern measurements, an SMA connector was soldered onto the CPW line. An HP 8530A network analyzer was used to measure the return loss. The simulated and measured results are presented in Figure 3.34, demonstrating a very good agreement. The return loss remains below -10 dB over most of the UWB range, and is above -10 dB only over a small frequency band above 10 GHz. Return loss is dominated by two major resonances, one at 4 GHz and a second one close to 9 GHz. The lower resonance is controlled by the ground segment width, H2. Practically, as H2 is increased, the lower frequency resonance is shifted downward. The 9 GHz resonance is primarily affected by the secondary axis length B; as B is reduced, the resonance shifts upward in frequency. If the two resonances are too close to each other, the return loss bandwidth cannot cover the whole UWB range and both lower and higher frequencies remain

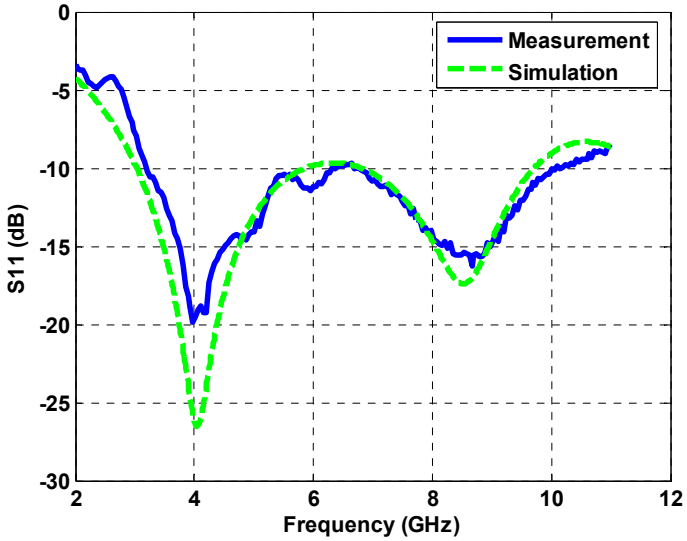

Figure 3.34: Measured and simulated return loss.

unmatched. If the two resonances are too far from each other, S11 is not below -10 dB over a range of frequencies in the middle of the UWB frequency range. Therefore the dimensions were optimized to cover most of the UWB frequency range. Ansoft HFFS was used to simulate and optimize the antenna parameters.

Radiation pattern measurements were taken in E and H planes. In both cases, simulated and measured co-polarization is presented. Only measurements at 5 GHz and 9 GHz are presented, however the radiation patterns are similar over the whole UWB range. Based on the antenna orientation presented in Figure 3.33, E plane cuts (x-z) for the two frequencies are presented in Figures 3.35a and 3.35b where $\theta=0^{o}$ coincides with z-axis and $\theta=90^{o}$ coincides with x-axis. In the E-plane, the x-axis is parallel to the feed line and results in a null in that direction.

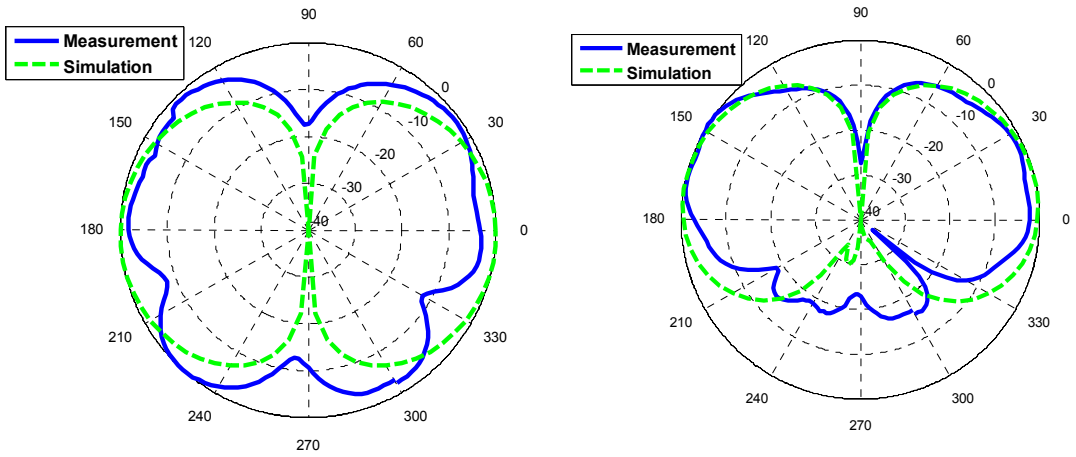

(a) (b)

Figure 3.35: (a) f=5 GHz E plane (x-z), (b) f=9 GHz E plane (x-z).

H plane (y-z) measurements are presented in Figures 3.36a and 3.36b, where it is seen that the pattern is omni-directional. z-axis corresponds again to $\theta=0^{o}$ while, in this case, $\theta=90^{o}$ coincides with y axis. In all cases simulations and measurements are in very

good agreement. Small variations in the pattern and the pattern symmetry in the measured data are due to reflections and blockage caused by the SMA launcher, detector, and cable.

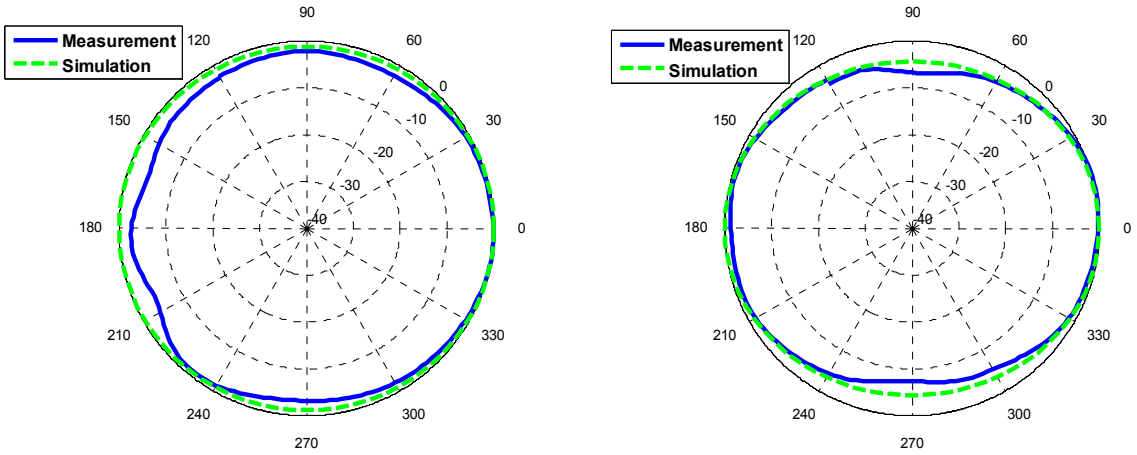

(a) (b)

Figure 3.36: (a) f=5 GHz H Plane (x-z), (b) f=9 GHz H Plane (x-z).

3.4.3 Summary

A compact, CPW-fed, elliptical monopole on an organic material (LCP) suitable for integration with other passive and active components was introduced and proposed for the UWB range. The presented antenna had omni-directional radiation patterns and this characteristic remained consistent with frequency. The elliptical monopole although was slightly bigger than the optimized cactus-shaped monopole, it can be used more easily, for a reconfigurable antenna with band rejection characteristic, which is the final objective.

CHAPTER IV

STUDY OF A CPW LINE TO AN ULTRA WIDEBAND ELLIPTICAL RADIATOR TRANSITION

In this section a transition from a typical co-planar waveguide (CPW) transmission line to an UWB elliptical radiator is studied and proposed as an effective solution in order to improve the matching without compensations with respect to the size of the actual radiator, or the size of the ground. While the transition significantly improves the matching, it does not deteriorate the radiation behavior, as verified by several return loss and radiation pattern measurements conducted for a number of different prototypes. [67]

4.1 Antenna Design

For the antennas' fabrication 100 μmthick Liquid Crystal Polymer (LCP) substrate was used with ε_r=3 and tanδ=0.002 and the laminated Cu was 18 μmthick. The primary radiator is an elliptical monopole with major axis A=18 mm and secondary axis B=15.30 mm. Figure 4.1 presents the details of the basic design and its dimensions are summarized in Table 4.1. The overall width of the ground from edge to edge (W_{g1}), length (L_g) and the distance between the ground and the farthest point of the ellipse are identical in all six prototypes presented in Figure 4.2. What varies in those cases is only the feed line geometry. The antennas presented in Figures 4.1a 4.1b and 1c are fed by typical CPW lines with Z_o=50 Ohms while the prototypes named as Sample 2 and Sample 3 use some kind of linear transition between the standard CPW line and the radiator, which will be the main topic of discussion in this work. Sample 1 and CPW 2 are identical but they are both presented and named differently to make both the reference

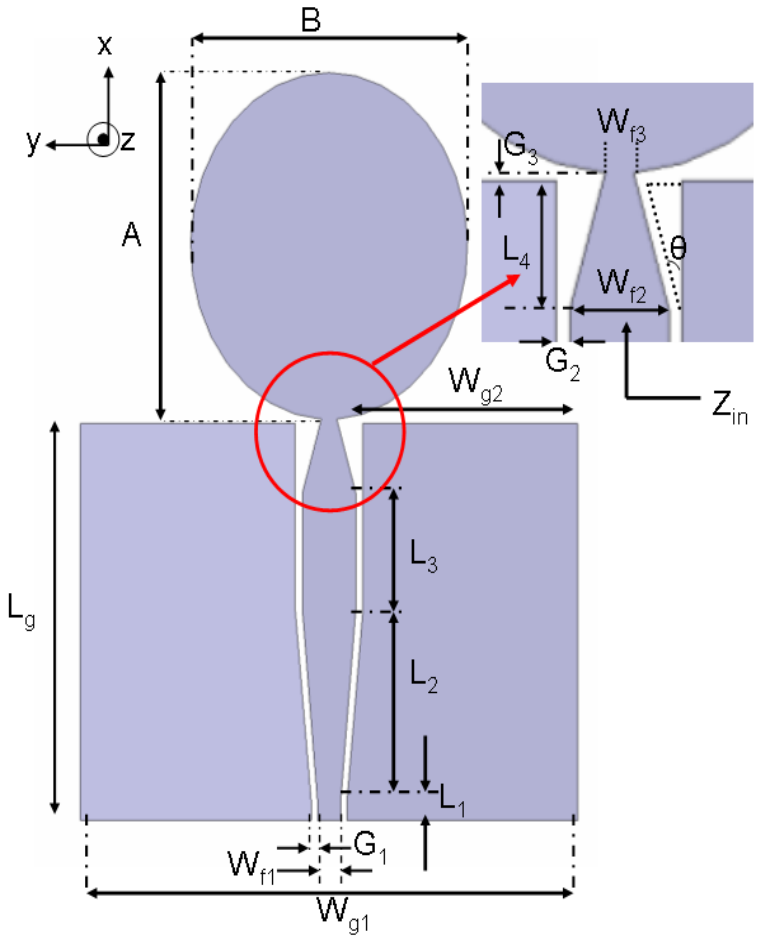

Figure 4.1: Antenna schematic.

Table 4.1 Antenna schematic dimensions

L_1	1.00 mm	W_{f3}	0.85 mm
L_2	10.00 mm	G_1	0.05 mm
L_3	6.00 mm	G_2	0.10 mm
L_4	3.70 mm	G_3	0.11 mm
W_{g1}	26.88 mm	L_g	20.70 mm
W_{g2}	12.25 mm	A	18.00 mm
W_{f1}	0.81 mm	B	15.30 mm
W_{f2}	2.97 mm		

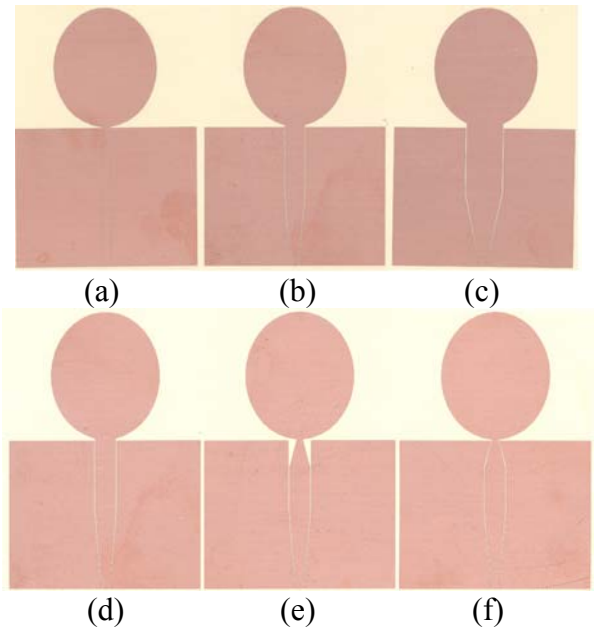

Figure 4.2: Fabricated prototypes: (a) CPW 1, (b) CPW 2 ,(c) CPW 3, (d) Sample 1, (e) Sample 2, (f) Sample 3.

and the comparison between different cases, easier. The equivalent lumped circuit model can be considered a transmission line with Z_o=50 Ohms which is terminated by a broadband load, in this case the elliptical monopole. Although the equivalent circuit would be the same for all thee models which are named CPW 1, CPW 2, and CPW 3 the measured return loss S11 is not the same as can be observed from Figure 4.3 where S11 measurements are plotted for the three cases. This happens because the interface between the CPW line and the actual radiator is not the same, something that proves that the transition between the feed line and the primary radiator (elliptical monopole) is critical for the overall matching and ultimately the performance of the antenna under investigation. In order to acquire accurate S11 measurements, 850-μm pitch probes were used instead of SMA connectors that could alternatively be used, in order to eliminate any unwanted reflections and consequently S11 distortion caused from the connector itself. In all six cases presented in Figure 4.2 the beginning of the CPW line has central

conductor with length W_{f1}=1.28 mm and gap between the central conductor and the ground patches G_1=50 um, which allows the use of the 850 μm pitch probes. CPW 1 has constant cross section while CPW 2 uses a linearly tapered segment with length L_2=10mm to a CPW line with central conductor length W_{f2}=2.97 mm and gap G_2=100 μm. Respectively, CPW 3 uses a linearly tapered transition with length also 10mm to a CPW line with W_{f2}=4.29 mm and G_2=125 μm. The CPW line dimensions used for CPW 2 are also used for Samples 1, 2 and 3. In the case of Sample 2, at distance L_3=6 mm from the beginning of the wider CPW line with W_{f2} and G_2 dimensions, the central conductor is linearly tapered down to W_{f3} =0.85 mm where it intersects with the elliptical radiator. In the case of Sample 3 the ground edge, is also linearly tapered by an angle θ=45^o with respect to the ground edge, as demonstrated in the embedded picture in Figure 4.2.

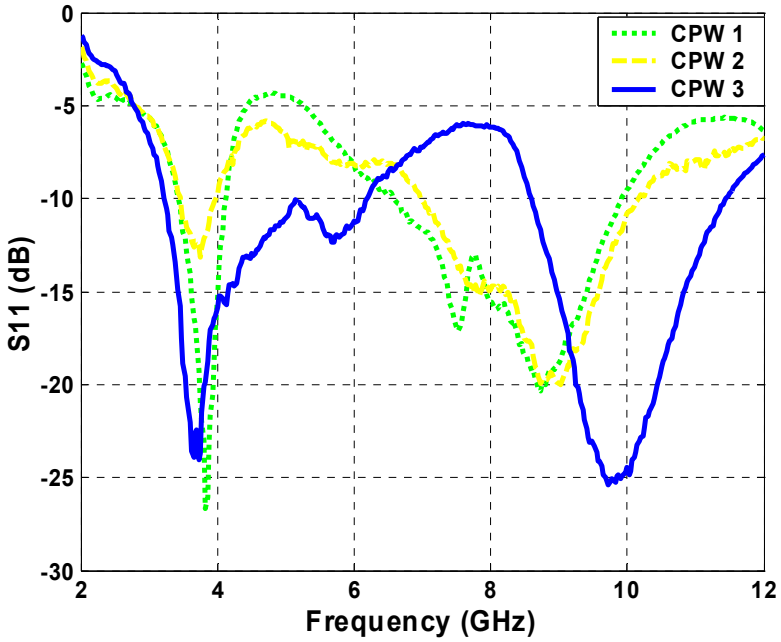

Figure 4.3: Return loss (S11) for elliptical monopoles fed with standard CPW line with Zo=50 Ohms.

4.2 Transition effect on return loss S11.

The return loss measurements for the antennas fed by standard CPW lines presented in Figure 4.3, demonstrate the lack of matching in the entire UWB range (3.1-10.6 GHz). On the other hand the measurements presented in Figure 4.4 prove that Sample 3 with the linearly tapered central conductor and linearly tapered ground is well matched from 3 GHz up to higher than 12 GHz, exceeding the designated UWB band. Measurements in Figures 4.3 and 4.4 demonstrate the importance of the transition between the feed line and the actual radiator. It has been shown that the actual dimensions of a UWB radiator, elliptical [68] or not [69], and the size (both width and length) of the ground [57] affect significantly the return loss for UWB antennas. The present work aims to demonstrate the importance of the transition when both the radiator and the overall ground size remain constant.

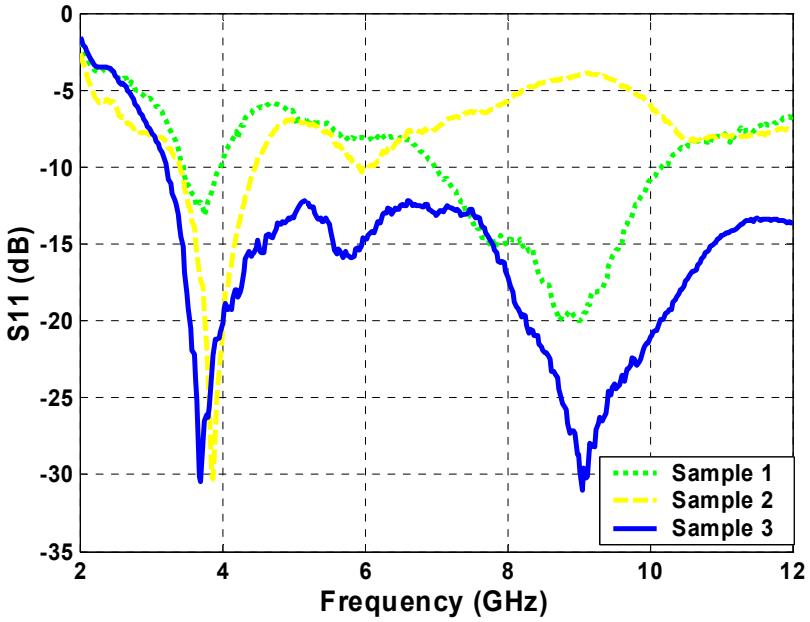

Figure 4.4: Return loss for Sample 1, Sample 2, Sample 3.

In order to investigate the transition mechanism a parametric sweep of angle θ is performed. Ansoft HFSS was used for the simulations. θ is swept from 0^o (Sample 2) to 45^o (Sample 3) with 15^o step. The simulated results of the real and imaginary part of input impedance are presented in Figure 4.5. To eliminate the effect of the transition from the narrow, probe-suitable CPW line to the wider CPW line, the presented Z_{in} is the de-embedded input impedance right before the linearly tapered transition as is shown in the embedded picture of Figure 4.2. As angle θ increases both real and imaginary part decrease. While the variation of the imaginary part is not too important since in all cases the imaginary part fluctuates between plus and minus 20 Ohms in the UWB frequency range, this is not the case for the real part. The real part of the impedance decreases constantly and for $\theta=45^o$ it approaches the Z_o value of 50 Ohms and results in the impressive matching improvement. To verify the trend indicated from the simulations the measured input impedance for Sample 2 ($\theta=0^o$) and Sample 3 ($\theta=45^o$) are presented on a Smith chart, depicted in Figure 4.6. The concentration of Sample 2's contour points to the right of the SWR=2 circle, indicates that the lack of matching is caused, mainly because of the relatively high values of the real part of the impedance. High real part values can be lowered by increasing angle θ, and the confinement of the real part value close to 50 Ohms, results in the good matching as can be seen from the dark contour which falls almost entirely inside the SWR=2 circle.

4.3 Radiation Patterns

Measured radiation patterns for Samples 1, 2 and 3 are presented in Figure 4.7. The measured patterns were taken in both E (x-z) and H (y-z) at 8 GHz. All the presented

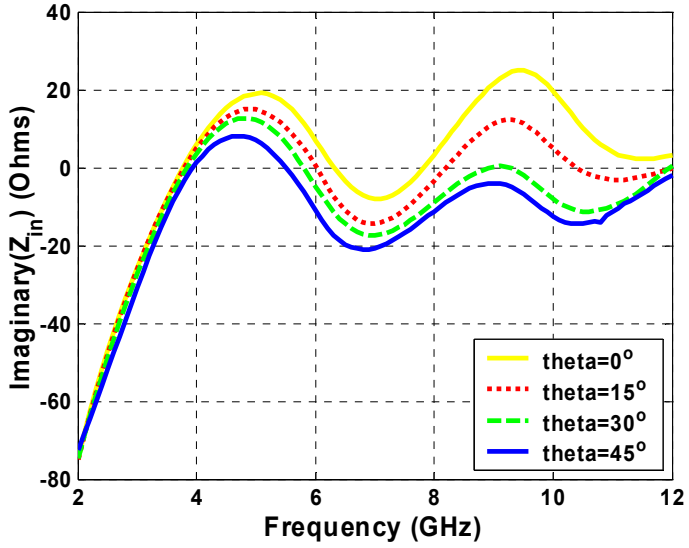

(a)

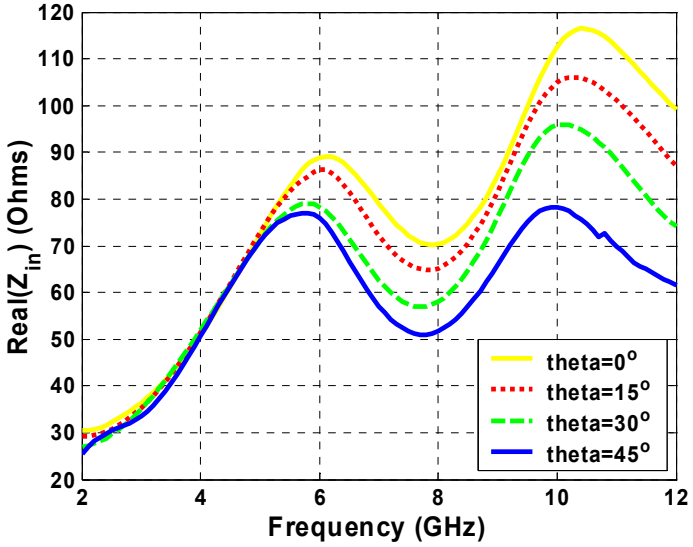

(b)

Figure. 4.5: (a) Imaginary part of input impedance Z_{in}, (b) Real part of input impedance.

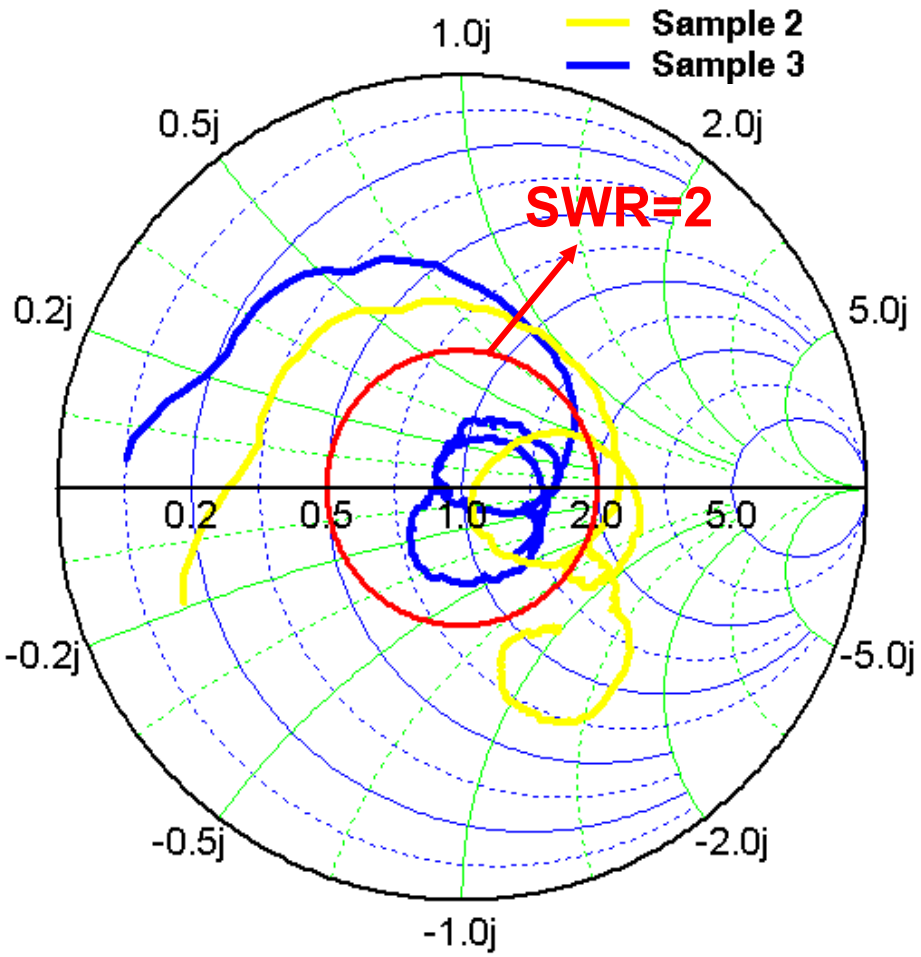

Figure 4.6: Measured input impedance for Sample 2 and Sample 3

contours are normalized independently. The E plane patterns have the characteristic for a monopole butterfly looking shape while the H plane patterns are omni-directional. The patterns for the three samples are almost identical, which is expected because the excited and radiated modes are the same. Consequently the transition improves the return loss behavior without affecting the radiation behavior in any significant way.

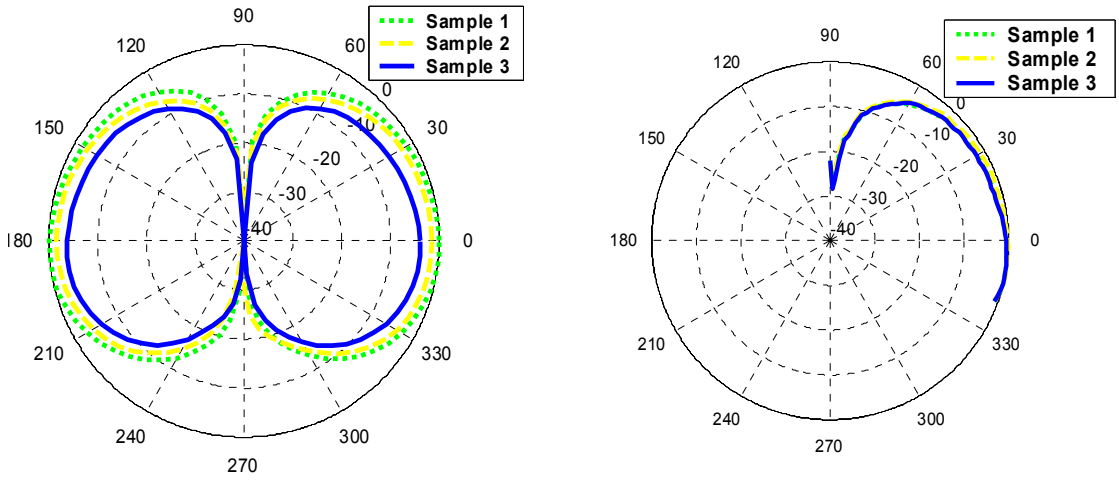

(a)

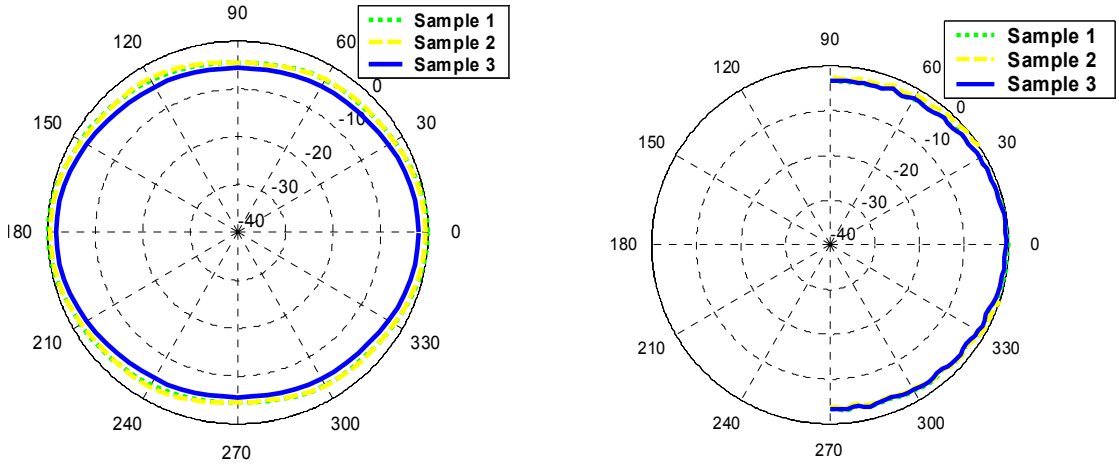

(b)

Figure 4.7: (a) E plane measurements and simulations (b) H plane measurements and simulations

4.4 Summary

The role of the transition from a CPW feed line to an UWB elliptical monopole, concerning the matching is investigated. Five prototypes are fabricated on 100 μm thick LCP material, with identical radiator and ground dimensions, and were tested in an attempt to examine weather the careful design of the transition can improve the matching, and how that affects the radiation properties. The geometrical characteristics of the transmission lines have some impact on the return loss even when the transmission line's characteristic impedance and the total length, remain the same. Although the use of several typical CPW lines does not ensure satisfactory matching throughout the whole UWB band, for the investigated elliptical radiator, the linearly tapered line and ground (Sample 3) reduce the high real part of the equivalent impedance, and can accomplish return loss below -10 dB in the desired frequency range. The matching improvement has practically no effect on the good radiation behavior of the elliptical monopole which remains omni-directional and therefore suitable for a number of UWB, hand-held, personal communications related applications.

CHAPTER V

STUDY OF CONFORMAL OMNI-DIRECTIONAL UWB ANTENNAS ON FLEXIBLE SUBSTRATE MOUNTED ON NON-PLANAR SURFACES FOR WBAN APPLICATIONS

One of the areas where the UWB features can be exploited is the Wireless Body Area Networks (WBAN) [70]. The low-power operation and the low radiated power make the UWB technology very attractive for wearable electronics. The antennas used for this application need to have some additional characteristics such as low weight, thin substrate thickness, and flexibility to conform to the body. In this work [71], the effect of conformal shaped UWB antennas with an omni-directional radiation pattern, suitable for WBAN applications, is studied experimentally. For the generality of the conclusions, three different antennas were fabricated on thin (less than 0.4 mm thick) flexible liquid crystal polymer (LCP) and studied.

5.1 Antenna Designs

To investigate the performance of a UWB antenna when the antenna is mounted on a non-planar surface, three different UWB antennas were used, an elliptical monopole antenna which will be referred to as EM, a polygonal monopole antenna which will be referred to as PM, and a U-stub fed elliptical slot antenna for which the acronym US will be used. The UWB monopole is one of the most attractive solutions for UWB applications and especially wireless body area networks (WBAN), therefore two different prototypes are investigated, while the elliptical slot antenna is an alternative candidate which can be preferred when higher gain is required. All three antennas, which are

presented in Figure 5.1a, were fabricated on liquid crystal polymer (LCP), which has relatively low dielectric constant (ε_r=3) and low loss (tanδ=0.002). For the two monopole antennas, the substrate thickness is 100 μm, while for the US, a thicker LCP substrate of 350 μm was used. The 350 μm thick substrate was acquired after three 100 μm substrates were stacked and thermo bonded using two 25 μm thick, lower temperature melting point LCP as bonding layers between two consecutive 100 μm thick samples. Standard photolithography was used to define the copper pattern. The fabricated prototypes were tested in planar shape and also when they were mounted on two styrofoam cylinders with radii 25 mm and 15 mm respectively. The antennas mounted on the styrofoam cylinders are shown in Figure 5.1b. It is noted that these radii of curvature are probably the smallest that would be required to conform to the human body and, therefore, yield data representative of what is required for a WBAN system.

(a)

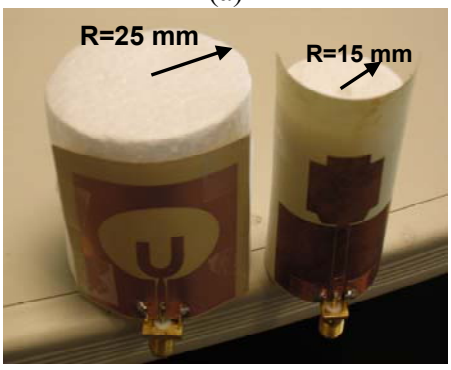

(b)

Figure 5.1: Photograph of fabricated antennas (a) in planar and (b) mounted on Styrofoam cylinders.

The EM was fabricated on an LCP board with overall dimensions 32 x 30 mm^2 and the schematic details are presented in Figure 5.2, while the antenna dimensions are summarized in Table 5.1. The PM, which is described analytically in Figure 5.3, was fabricated on a board with overall dimensions 48 x 44 mm^2, and the dimensions are summarized in Table 5.2. The reason why two monopole antennas were considered was the considerable difference in size between the two proposed designs. The EM covers only 45% of the surface that the PM covers and, therefore, when the monopole is compared with the US antenna which has overall dimensions 40 x 38 mm^2 the factor size must be taken into consideration, especially when the antennas are mounted on cylinders with a big radius compared to the antenna dimensions. Therefore, two monopoles were used, one smaller and another one bigger than the US antenna, which is described in detail in Figure 5.4. The exact design parameter values for US can be retrieved from Table 5.3.

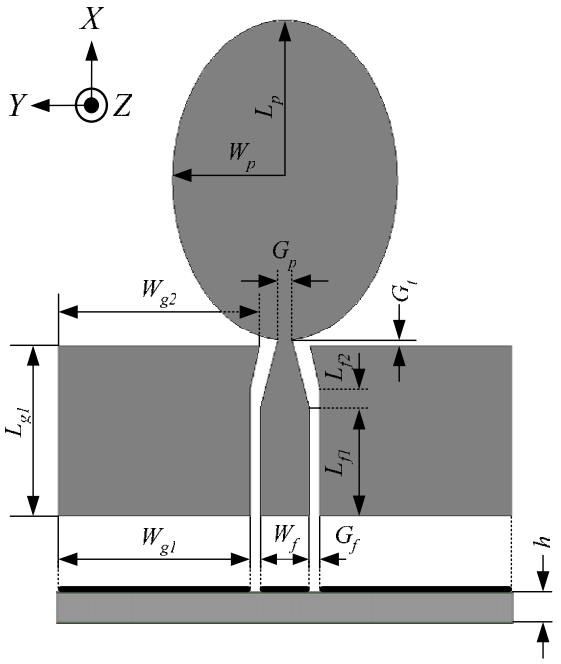

Figure 5.2: Elliptical monopole (EM) schematic.

Table 5.1: Elliptical monopole schematic dimensions (mm).

L_{g1}	9.60	G_f	0.10
L_{f1}	6.10	W_{g1}	11.50
L_{f2}	1.13	W_{g2}	12.07
L_p	4.50	W_p	3.38
G_t	0.32	W_f	2.94
G_p	0.85	h	0.10

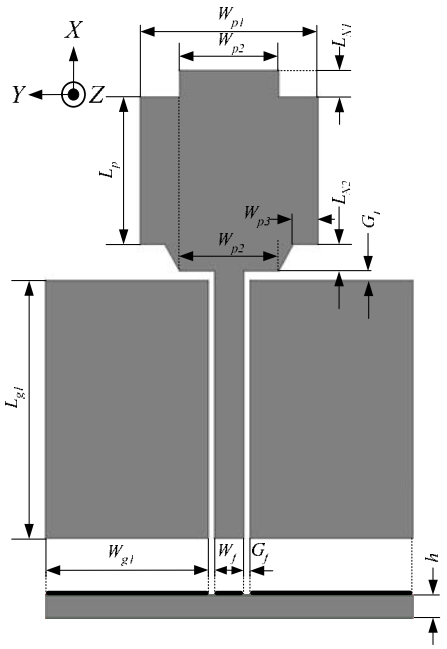

Figure 5.3 : Polygonal monopole (PM) schematic.

Table 5.2: Polygonal monopole schematic dimensions (mm).

L_{g1}	25.00	G_f	0.10
L_p	14.00	W_{g1}	16.46
L_{N1}	2.50	W_f	2.94
L_{N2}	2.50	G_t	0.40
W_{p1}	18.00	h	0.10
W_{p2}	10.00	W_{p3}	1.50

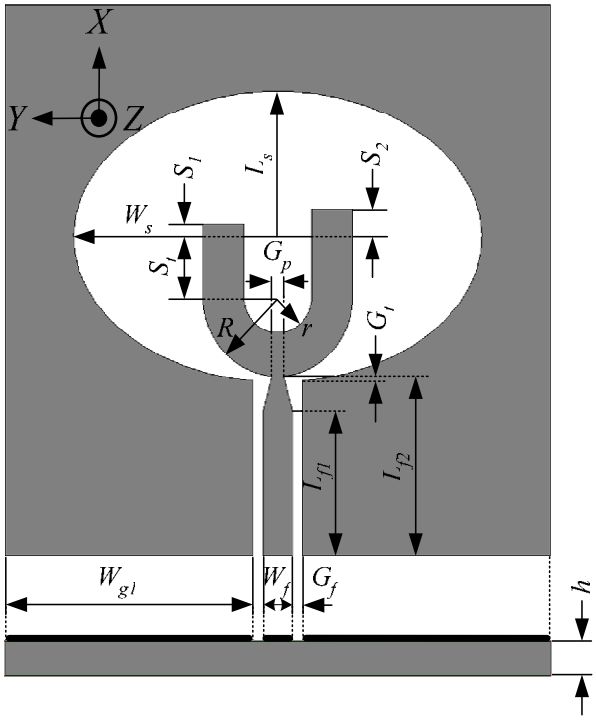

Figure 5.4: U-stub (US) fed slot antenna schematic.

Table 5.3: U-stub slot antenna schematic dimensions (mm).

L_{f1}	9.90	S_1	0.90	W_{g1}	18.60
L_{f2}	13.40	S_2	1.90	W_f	2.20
G_t	9.37	S_t	4.10	G_f	0.30
L_S	10.00	R	5.50	G_p	0.86
W_S	15.00	r	2.50	h	0.35

5.2 Return Loss and Radiation Pattern Measurements

5.2.1 Return Loss

For the return loss measurements, SMA connectors were soldered on the CPW feed lines and the HP 8530 vector analyzer was used. The antennas were measured in planar shape and mounted on two cylinders with radii 25 mm and 15 mm respectively, that were made of styrofoam (ε_r=1.03). The planar state of the antenna can be considered as an antenna mounted on a cylinder with infinite radius and is denoted in the presented figures'

legends as R=inf. The measured return loss results for the three antennas are presented in Figure 5.5. The EP return loss has two resonances that are related to the ground width and the ellipse secondary axis size as explained in [72]. The PM has a similar behavior but is generally better matched. Lastly, the two resonances appearing at the US return loss are related to the elliptical slot size as mentioned in [73].

It can be clearly seen that the measured return loss for the three different radii values of all three prototypes are almost identical. The position of the resonances remains constant and the only difference is observed for the US antenna where the second resonance's depth changes, however in all cases it remains below -20 dB. That small change occurs because the field distribution is concentrated along the ellipse circumference and therefore the area used is larger compared to the monopoles, making the antenna more sensitive when it comes to the S11. Still the difference in absolute values is only 1%. To get an estimation of how sensitive the return loss is with respect to the radius, the PM antenna was wrapped in a cylinder with a radius of only 5 mm and the measured return loss demonstrated very similar behavior with the measurements presented in Figure 5.5b. The size of the PM and the LCP thickness allows the antenna to be folded to that extreme extent (R=5 mm), which is not possible for the EM and US antennas. Consequently, the return loss is not affected significantly by folding, and the good matching throughout the UWB band remains, even for extreme folding cases.

5.2.2 Radiation Patterns

For the return loss and the radiation pattern measurements, an SMA to microstrip launcher was soldered onto the LCP substrate with the launcher tab soldered to the CPW center conductor and two ground tabs soldered to the CPW ground planes. Special care was taken to position the connections symmetrically along the CPW center to avoid excitation of parasitic modes. No tuning stubs were used for impedance matching since the antennas demonstrate good matching in the whole UWB range due to the effective design of the transition. For radiation pattern measurements, the UWB antennas were placed between two pieces of 1.5 cm thick styrofoam to give the antenna mechanical support and hold it in the position of the contour since the LCP substrate is very flexible and conformal.

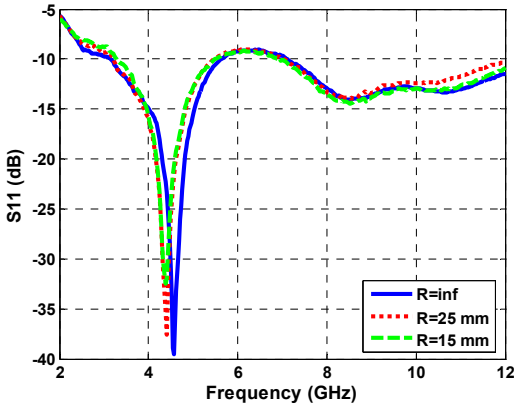

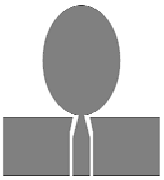

(a)

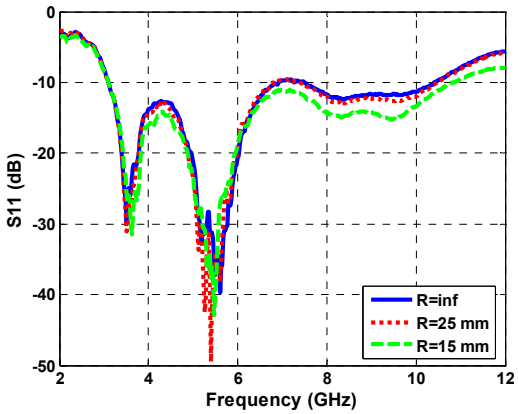

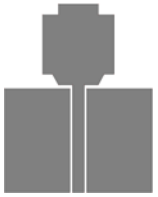

(b)

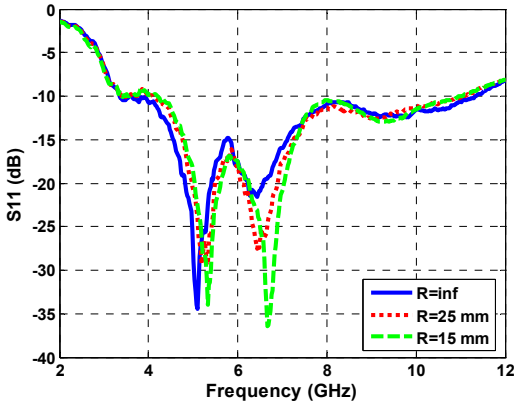

(c)

Figure 5.5: Measured return loss (S11) for (a) Elliptical monopole (EM), (b) Polygonal monopole (PM), and (c) U-stub fed slot (US) antennas.

The radiation pattern measurements were performed in the E (x-z) and H (y-z) planes with the directivity direction being the intersection of the two planes (z axis direction). Each antenna was tested in a far-field range with the UWB antenna as the receive antenna, and a 2 to 18 GHz, ridged-rectangular horn antenna was used as the transmitting antenna. The separation between the two antennas was 118.75 cm. After experimentally determining the maximum transmitted power to achieve the greatest dynamic range without saturating the detector, the detector was calibrated. The rotary stage and the detector voltage recording from the lock-in amplifier were automated. Before each radiation pattern measurement, a laser was used to align the antenna under test to the transmitting antenna to with 1˚, but because the Styrofoam block was cut to the contour shape using a saw, the antenna pointing inaccuracy may be slightly greater. Pattern measurements were taken at 3, 5, 7 and 9 GHz, however for brevity, only patterns at 5 and 9 GHz are presented. The omitted patterns present very similar behavior as a result of the pattern consistency that is observed for all three antennas.

The measured co (solid line) and cross (dashed line) polarizations patterns for the planar antennas in direct comparison with the antennas mounted on a cylindrical surface with radius R=25 mm are presented in Figure 5.6. All of the measured patterns concerning the same antenna are presented in the column under the antenna schematic. E plane patterns for the three antennas at 5 GHz are presented in plots 6a, 6b and 6c while the E plane measurements at 9 GHz are shown in plots 6d, 6e and 6f. The 90^{o} direction in the E plane patterns coincides with the x axis direction as defined with respect to the antennas direction in Figures 5.2, 5.3 and 5.4. In all cases there is a null in the x axis direction, which is due the feed line presence. The omni directional behavior of the antennas under study is obvious in the H plane cuts which are presented with plots 6g, 6h and 6i at 5 GHz and plots 6j, 6k and 6l at the higher frequency at 9 GHz. For the H plane patterns, the 0^{o} direction, which is horizontal, coincides with the z axis, which is also the directivity direction. The two monopoles have more omni directional patterns compared to the US

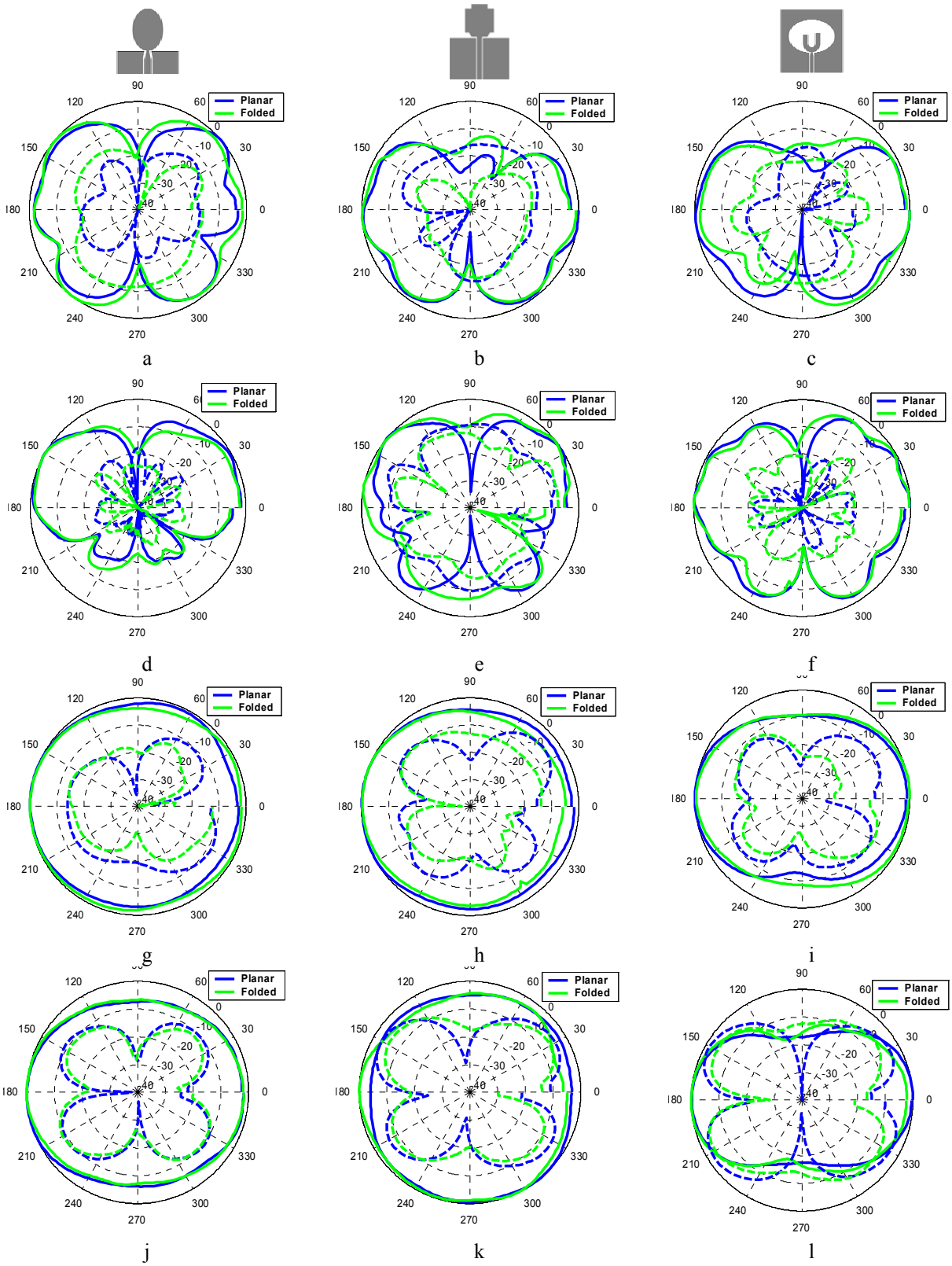

Figure 5.6: Measured radiation patterns for planar and folded antenna mounted on a 25 mm radius styrofoam cylinder. (a), (b), (c): E plane at 5 GHz (d), (e), (f) :E plane at 9 GHz, (g), (h), (i): H plane at 5 GHz and (j) (k), (l): H plane at 9 GHz.

antenna, which has an ovaL-shaped H plane pattern and higher directivity, which is verified by the gain measurements presented next. The cross polarization level in H plane is higher compared to the E plane verifying the results presented in [74] for both cases. In all of the radiation patterns, the agreement between the planar and folded antennas is remarkable. Even the shape of the cross polarization in most of the cases demonstrates a very good agreement between the planar and folded antennas while at the same time the directivity direction remains constant along the z axis. Thus, the radiation pattern is not affected by conforming the antennas around a cylinder in the transverse direction.

5.2.3 Gain Measurements

The antenna gain was measured by using the substitution method with an antenna of known gain, in this case, a second 2 to 18 GHz, Q-par Angus Ltd horn antenna. The "known" gain of the Q-par antenna is specified to be accurate to within ±0.8 dB; thus, this becomes the accuracy of the gain measurements presented in this paper. The gain measurements were taken in the directivity direction which coincides with the z axis direction as it is defined in Figures 5.2, 5.3 and 5.4, and are presented in Figure 5.7. While the three antennas demonstrate different gain behavior, in all three cases very similar behavior is observed between the planar antennas and the folded (R=25 mm) ones. Specifically the EM has relatively lower gain at the lower frequencies verifying the behavior reported in [73] while the PM demonstrates lower gain for the frequencies higher than 8 GHz. On the other hand the US performs with consistently higher than 2.5 dBi gain throughout the UWB frequency range. Regardless how high or how stable the measured gain is, both in the monopoles' case and the slot antenna's case, the measurements prove that the gain performance of the tested UWB antennas remains constant while the antennas are folded.

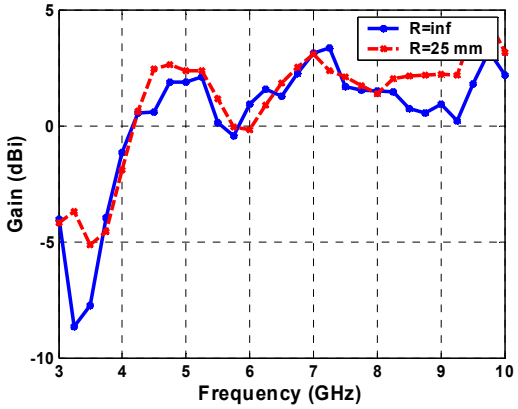

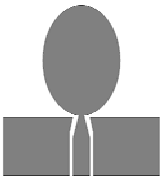

(a)

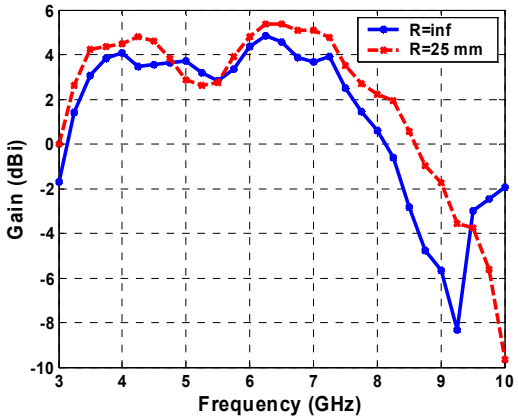

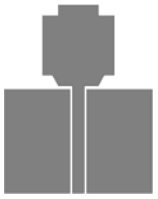

(b)

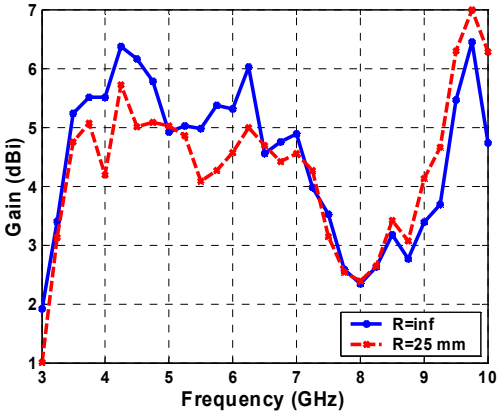

(c)

Figure 5.5: Gain measurements for (a) Elliptical monopole (EM), (b) Polygonal monopole (PM), and (c) U-stub fed slot (US) antennas.

5.3 Frequency Domain Measurement for Distortion Estimation

5.3.1 Experimental Setup

To estimate the effect of folding the conformal UWB antennas on a transmitted pulse, a frequency domain measurement was taken using the HP 8530 A network analyzer. The measurement setup is presented in Figure 5.8. Two antennas are used one as a transmitter and another identical antenna as a receiver. The two antennas are aligned so that their directivity directions face each other. The distance between the tested antennas was set at 1.5 m ensuring that is greater than the far field distance which is defined by $2D^2/\lambda$ where D is the maximum antenna dimension and λ is the free space wavelength. The far field distance, which corresponds to the antenna with the largest dimensions and the wavelength corresponding to 10.6 GHz, is less than 0.2 m. The antennas are tested in planar shape and while they are mounted on cylinders with radii 25 mm and 15 mm as shown in Figure 5.1. In all three cases, for the planar (R=inf) and the

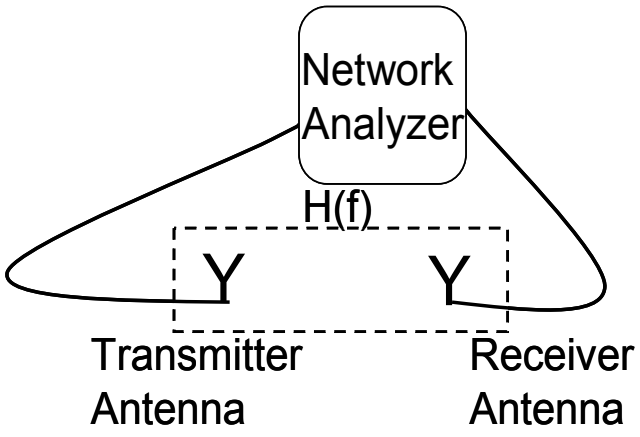

Figure 5.8: Setup for the system: transmitter - channel – receiver, frequency domain measurement.

two folded ones, the S21 measurement which represents the transfer function H(f) of the system transmitter antenna - wireless channel – receiver antenna was taken from 3.1 GHz to 10.6 GHz covering exactly the frequency range allocated from FCC for UWB communications. The measurements were taken in a laboratory environment with tables, chairs, and other equipment to better represent a realistic communications environment than would be offered if the measurement was taken in an anechoic chamber.

5.3.2 Distortion Estimation

The raised cosine pulse was used to get an estimate of how much a transmitted pulse is distorted by the system: antenna – channel – antenna and what is the effect on the transmitted pulse when the antennas are not planar but mounted on cylindrical surfaces instead. The idea is to use the measured transfer function H(f) with the analytical spectrum S(f) of an analytically defined transmitted pulse s(t). [56] The analytical expression of the raised cosine pulse, which is very popular for several modulations because it has low (zero) intersymbol interference (ISI), is given by (5.1) while its spectrum is given by (5.2). For the pulse defined in (1) Ts = 1/BW is used, where BW=(10.6 – 3.1) GHz and the roll-off factor is α=0.5.

$$s_{RC} = F^{-1}\left\{H_{RC}(f)\right\} = \frac{\sin(\pi t/\mathrm{T}s)}{\pi t/\mathrm{T}s}\frac{\cos(a\pi t/Ts)}{1-4a^2t^2/Ts^2} \tag{5.1}$$

$$H_{rc} = \begin{cases} Ts & 0 \le |f| \le (1-a)/2Ts \\ \dfrac{Ts}{2}\left[1-\sin\dfrac{\pi Ts}{a}\left(|f|-\dfrac{Ts}{2}\right)\right] & (1-a)/2Ts \le |f| \le (1+a)/2Ts \\ 0 & (1+a)/2Ts \le |f| \end{cases} \tag{5.2}$$

The spectrum of the received pulse is consequently R(f)=S(f)H(f) and the received pulse in time domain can be extracted using the inverse Fourier transform $r(t)=F^{-1}\{R(f)\}$. An estimation of the added distortion from the UWB system can be made using the correlation defined by (5.3) between the transmitted pulse s(t) and the received pulse r(t). x(i) and y(i) are the compared waveforms, m_x and m_y are the respected mean values. When the compared waveforms are identical, the $\max_d\left(Corr\left(d\right)\right)$ equals to one, and it is zero when the waveforms are orthogonal.

$$Corr(d)=\frac{\sum_i\left[\left(x(i)-m_x\right)\left(y(i-d)-m_y\right)\right]}{\sqrt{\sum_i(x(i)-m_x)^2}\sqrt{\sum_i(y(i)-m_y)^2}} \tag{5.3}$$

The sent and received raised cosine pulses can be seen in Figures 5.9a, 5.9b and 5.9c for the EM, the PM, and the US respectively. Four contours are presented in each plot, the sent pulse with the light solid line, the received pulse for the planar antennas (R=inf) with the dark solid line, and the two received pulses for the conformal antennas (R=25mm and R=15mm) which are plotted in dashed lines. The similarity among the received pulses for the different conditions under which the antennas operate is obvious. Table 5.4 summarizes the maximum correlation of the three received pulses with the sent pulses. The lowest value is 0.83 for the EM mounted on the small cylinder while for most of the other cases the correlation is higher than 0.9 proving that firstly, the systems can recognize a transmitted pulse with high accuracy, and secondly, folding the antennas does not constitute a disadvantage in their performance and, consequently, they can be used mounted on non-planar surfaces and still perform with the same reliability.

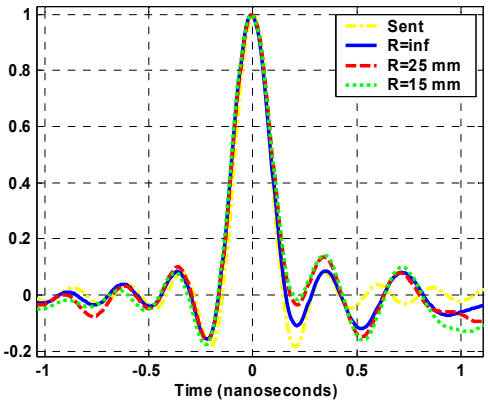

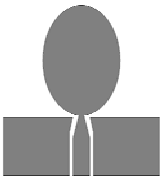

(a)

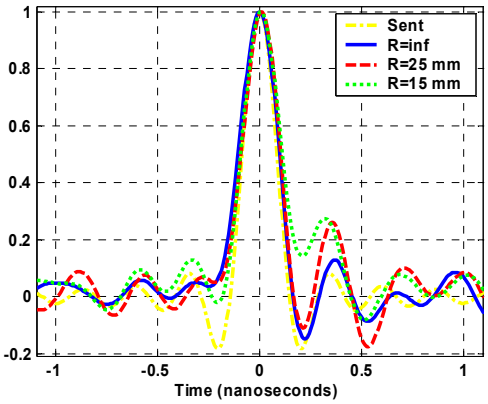

(b)

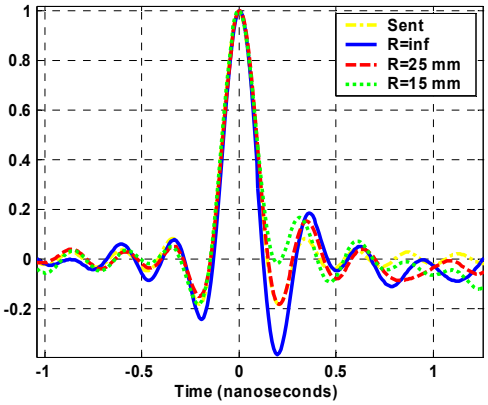

(c)

Figure 5.9: Sent and received raised cosine pulse for planar and folded antennas. (a) Elliptical monopole (EM), (b) Polygonal monopole (PM), and (c) U-stub fed slot (US).

Table 5.4: Correlation of received with transmitted pulses for raised cosine pulse.

	R=00 mm	R=25 mm	R=15 mm
EM	0.91	0.86	0.83
PM	0.95	0.91	0.90
US	0.94	0.93	0.92

Since the spectrum of the used pulse and some other pulse characteristics affect significantly the performance of a communication system, the pulse influence should be de-embedded and eliminated in order to evaluate exclusively the performance of a UWB system with conformal antennas and compare it more accurately with a competitive system that uses the antennas in their unfolded planar state. Therefore, the measured H(f) were transformed in time domain using the inverse fast Fourier transform (I-FFT) and the calculated impulse responses of the systems with the planar and folded antennas are compared in Figures 5.10a, 5.10b and 5.10c for the three AUT. A similar method was used in [75]. Since the bandwidth of the measured H(f) is limited, the time description should have an infinite tail, however the presented impulse responses are zoomed for clarity, in order to include only the main lobe and part of the tail. The origin in time axis is set arbitrarily since the important parameter is the pulse duration and the zero on the time axis has no significance and the pulses are normalized. The correlation results of the impulse responses of the folded antennas with respect to the impulse response of the planar antennas are summarized in Table 5.5, where the obvious similarity in the responses observed in Figure 5.10 is confirmed.

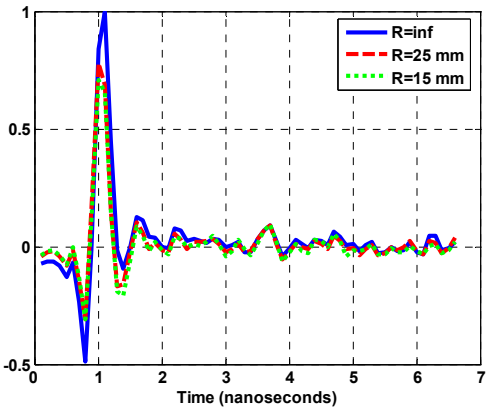

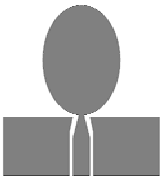

(a)

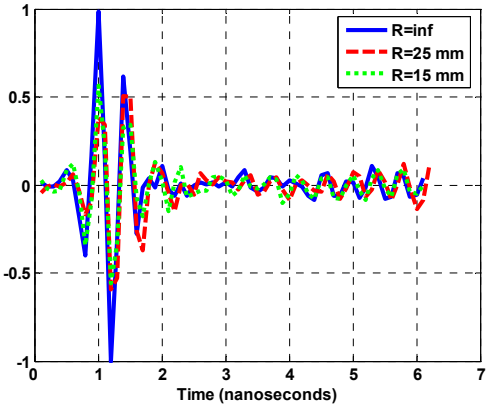

(b)

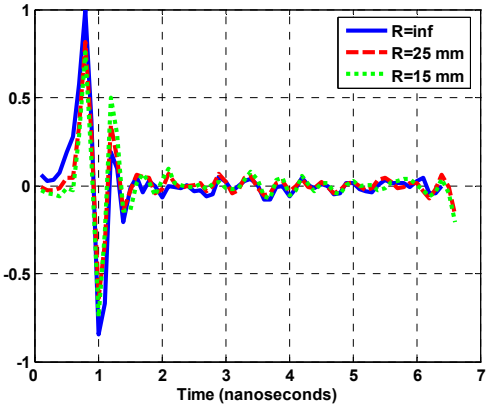

(c)

Figure 5.10: Time impulse response (I-FFT of transfer function) (a) Elliptical monopole (EM), (b) Polygonal monopole (PM), and (c) U-stub fed slot (US).

Table 5.5: Correlation of I-FFT for planar with I-FFT for folded antennas.

	R=25 mm	R=15 mm
EM	0.95	0.94
PM	0.88	0.82
US	0.94	0.86

5.4 Summary

Three antennas operating in the UWB range, two monopoles and a slot are presented as candidates for conformal packaging and for WBAN applications. These antennas were chosen because they have a variety of substrate thicknesses, shapes, and sizes to obtain results that are as general as possible and are not related exclusively with a certain type of UWB antenna. This research shows that the antennas aimed for WBAN applications or any other application, where the shape of the antenna will be non-planar, can be studied and optimized in their planar (unfolded) configuration, which is significantly easier compared to studying a conformal antenna, and still can be trusted to operate equally well in their non-planar shape. Return loss measurements, radiation pattern and gain measurements show no significant variation between a planar antenna and an antenna folded in the transverse direction mounted on cylindrical surfaces with radii 25 mm and 15 mm. Additionally, the impulse response of a simple UWB communication system using conformal antennas and the added distortion to a transmitted pulse are almost identical with those of a system using antennas in their standard planar shape. Therefore a variety of required UWB antennas for conformal packaging applications, can be designed, optimized and tested in their planar shape and can still be used reliably in non-planar topologies.

CHAPTER VI

UWB ELLIPTICAL MONOPOLES WITH RECONFIGURABLE BAND NOTCH USING MEMS SWITCHES ACTUATED WITHOUT BIAS LINES

FCC released the Ultra Wide Band protocol that covers the frequency range from 3.1-10.6 GHz in 2002, as an attempt to meet the demand for high data rate communications in short distances for mobile and personal applications. However the designated band overlaps with the HIPERLAN/2 bands (5.15-5.35 GHz, 5.470-5.725 GHz) and the IEEE 802.11a bands (5.15-535 GHz, 5.725-5.825 GHz) which can interfere with the UWB communication systems. Therefore there is a need for UWB antennas with band rejection characteristics in the aforementioned frequency bands. Since today's communications environment changes constantly there is also a need for reconfigurable designs which will utilize the environment changes in order to achieve higher performance. This work presents two prototypes fabricated on LCP with reconfigurable rejection band (band notch) in the frequency range between 5 GHz and 6 GHz. The first prototype uses a $\lambda/2$ U-shaped slot and the second prototype two $\lambda/4$ inverted L-shaped stubs as resonating elements. Micro electro mechanical system (MEMS) switches are used to activate and deactivate the resonating elements and based on a new switch topology the switches are actuated without the need of DC bias lines [76].

6.1 Antenna Design

The antenna used for the integration of the reconfigurable resonating elements that result in a reconfigurable band notch, is a CPW line fed elliptical monopole. 100 μm thick LCP (ε_r=3, tanδ=0,002) was used and 3 μm of Al was sputtered on top of 0.2 μm Ti and

standard photolithography was applied. LCP samples were polished to reduce the surface roughness and allow the MEMS switch fabrication. The two fabricated prototypes are presented in Figure 6.1 MEMS switch fabrication and integration will be discussed in a following section.

The elliptical radiator has major axis A=18 mm and secondary axis B=15.30 mm. Figure 6.2 presents the details of the schematic design and its dimensions are summarized in Table 6.1. The overall width of the ground from edge to edge is W_{g1}=26.88 mm, and the ground length is L_g=20.7 mm. For the feeding of the elliptical monopole a CPW feed line with central conductor width W_{f2}=3.89 mm and gap G_2=100 μm resulting in a characteristic impedance (Z_o) of 50 Ohms, is used. In order to use the 850-μm pitch probes for measurements, the CPW line is linearly tapered down to another more narrow CPW line with 50 Ohm characteristic impedance (W_{f1}=1.28 mm and G_1=50 um) that has length only L_1=1 mm . A customized transition from the standard CPW line (W_{f2}, G_2) to the ellipse was used to improve the matching. The matching improvement can be seen in Figure 6.3 where the input impedance of two antennas, one referred to as "Standard CPW" and one referred to as "Reference" are presented on a Smith chart. The "Standard CPW" does not use any transition and a standard CPW line with the above mentioned geometrical characteristics (W_{f2}, G_2) is terminated with the elliptical radiator. The "Reference" is identical with the antenna presented in Figure 6.2 without the slot or the two open stubs. It is referred to as "Reference" because it will be compared to the antennas with the reconfigurable resonating elements. Figure 6.3 proves that although a typical CPW line cannot establish good matching for this elliptical monopole the use of the appropriate

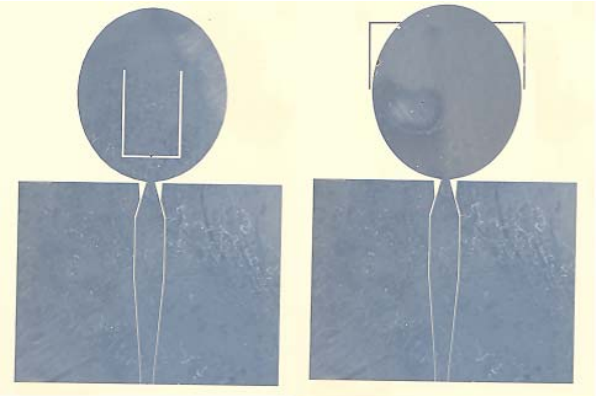

Figure 6.1: Fabricated prototypes with MEMS.

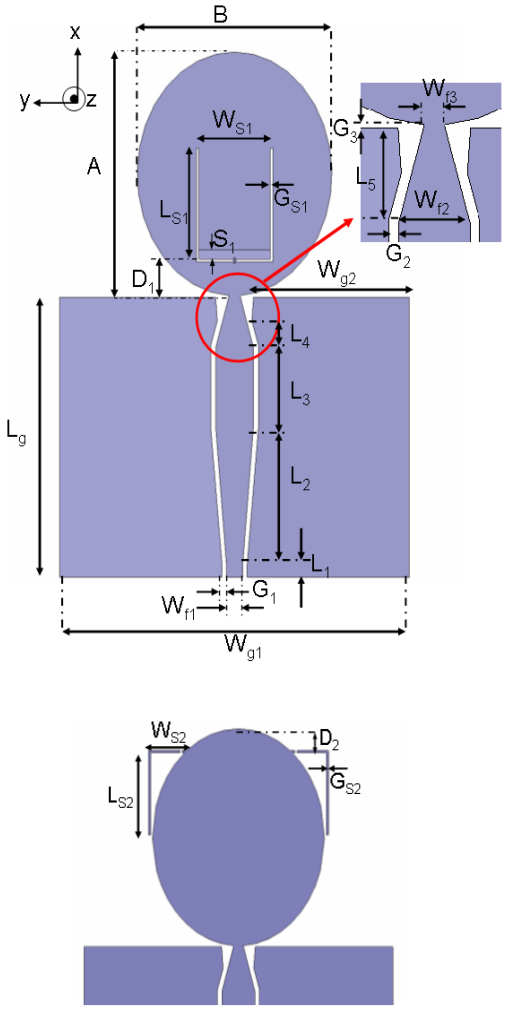

Figure 6.2: Antenna Schematic.

Table 6.1 Antenna schematic dimensions

L_1	1.00 mm	W_{S2}	3.41 mm	W_{f3}	0.85 mm
L_2	10.00 mm	G_{S2}	0.20 mm	S_1	0.70 mm
L_3	6.00 mm	L_{S2}	6.80 mm	G_1	0.05 mm
L_4	1.93 mm	D_2	1.80 mm	G_2	0.10 mm
L_5	3.70 mm	W_{g1}	26.88 mm	G_3	0.11 mm
W_{S1}	5.60 mm	W_{g2}	12.25mm	L_g	20.70 mm
G_{S1}	0.20 mm	W_{f1}	13.76 mm	A	18.00 mm
L_{S1}	8.8 mm	W_{f2}	38.80 mm	B	15.30 mm
D_1	2.60 mm				

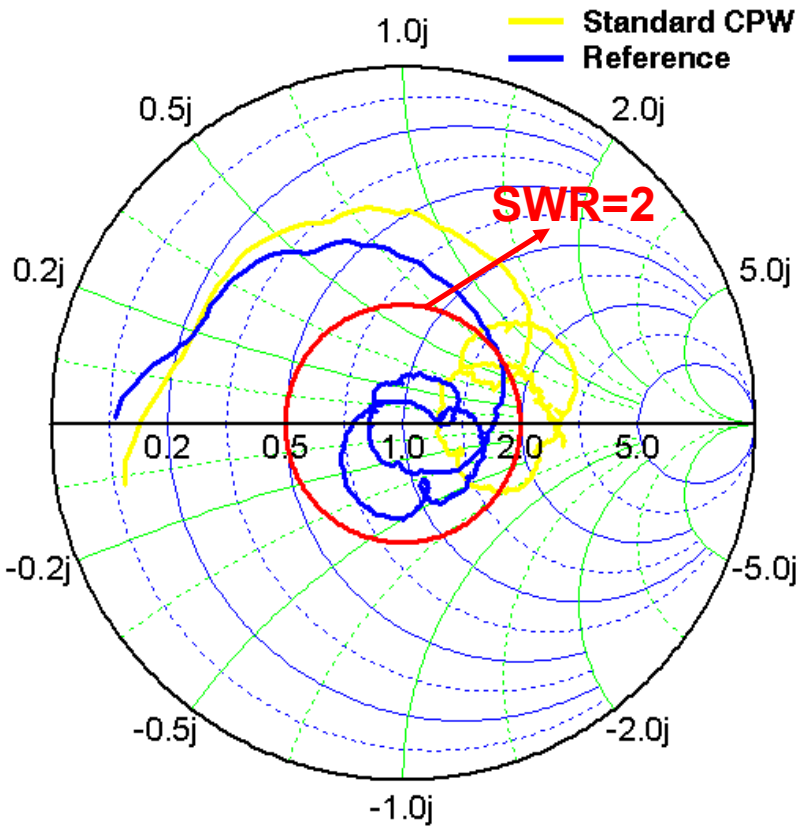

Figure 6.3: Input impedance for "Standard CPW" and "Reference" antennas on Smith chart.

transition can achieve SWR less than 2 in the whole UWB range. The two lines represent measurements taken between 2 to 12 GHz. The segment of the "Reference" line that falls outside the SWR=2 circle corresponds to the frequency range from 2 GHz to 3 GHz which is not part of the UWB frequency range. Two different approaches are used to acquire a reconfigurable band notch between 5 and 6 GHz. In the first case a U-shaped slot is used and in the second case two inverted L-shaped open stubs are used. The U-shaped slot is presented in Figure 6.1a and its lowest edge is positioned at a distance D_1=2.6 mm from the nearest ground edge. It consists of two parallel segments of length L_{S1}=8.8 mm and a third segment with length W_{S1}=5.6 mm. In the middle of this third segment a MEMS switch is integrated in order to selectively short the 0.2 mm wide slot. Another very thin slot (only 3 μm wide) is created parallel to the third segment at a distance S_1=0.7 mm from it. Therefore an isolated rectangular segment is defined which serves as the floating DC ground which is necessary for the MEMS switch actuation. For the design shown in Figure 6.1b two inverted L open stubs with width G_{S2}=200 μm and total length 10.41 mm (L_{S2}+W_{S2}+G_{S2}) cause the band notch. Both stubs are placed at a distance D_2=1.8 mm from the top point of the ellipse. Two MEMS switches are used to electrically connect and disconnect the two stubs to the elliptical radiator. The switches are positioned 0.4 mm far from the ellipse. Bias lines are not needed in neither the slot nor the stubs case for the MEMS switch actuation because of the switch topology.

6.2 Operation Principles

In both cases the idea remains the same. In the U-shaped slot case the total length of the slot is approximately λ/2, and the two inverted L-shaped stubs have length approximately

λ/4 at 5.8 GHz resulting in resonating elements. At the vicinity of that frequency the radiation is blocked and the frequency notched is created.

6.2.1 Theory

The U-shaped slot resonates and therefore creates a band notch at the frequency that is related to its geometry dimensions as defined by: $f_U \approx \frac{c}{4\left(L_{S1} + \frac{W_{S1}}{2} - G_{S1}\right)}$ where c is the speed of light [77]. The surface current distribution presented in Figure 6.4a shows how the U-shaped slot resonates at 5.8 GHz and how this behavior is cancelled when the slot is shorted (Figure 6.4b), or at a different frequency (8 GHz current distribution is presented in Figure 6.4c). The directions of the current in the inner and outer side of the slot are opposite and they cancel each other as explained in detail in [77], [78]. As a result the antenna does not radiate at that frequency and a frequency notch is created around the frequency of 5.8 GHz. When the slot is shorted the total length of the slot is divided in two, and consequently it cannot support the resonating currents and radiation occurs as if the slot was not present. A transmission line model, similar to the approach introduced in [77], is presented in Figure 6.5 which explains the slot effect. The presence of the slot is modeled as a λ/4 long stub. When the slot is not shorted the stub is considered to be an open stub. On the transmission line it will appear as an ideal short and the incident energy will be reflected and thus it will not be delivered to the load to be radiated (Figure 6.5a). When the MEMS switch is in down position the stub is considered as shorted and under the λ/4 transformer effect it will appear as an ideal open on the line and therefore the incident power will be delivered to the load and it will be radiated.

Similarly the inverted L-shaped stubs resonate approximately at a frequency defined by: $f_{inverted\_L} \approx \frac{c}{4(W_{S2} + L_{S2})}$ where again c is the speed of light. Figure 6.4d shows how the two stubs resonate at 5.8 GHz. When the two stubs are not connected to the elliptical radiator no currents flow through the stubs (Figure 6.4e) but even when they are connected they do not resonate at a different frequency (8 GHz current distribution is presented in Figure 6.4f). At the resonance frequency, the direction of the current on the inverted L-shaped stub, and the direction of the current along the nearby edge of the radiator, are opposite to each

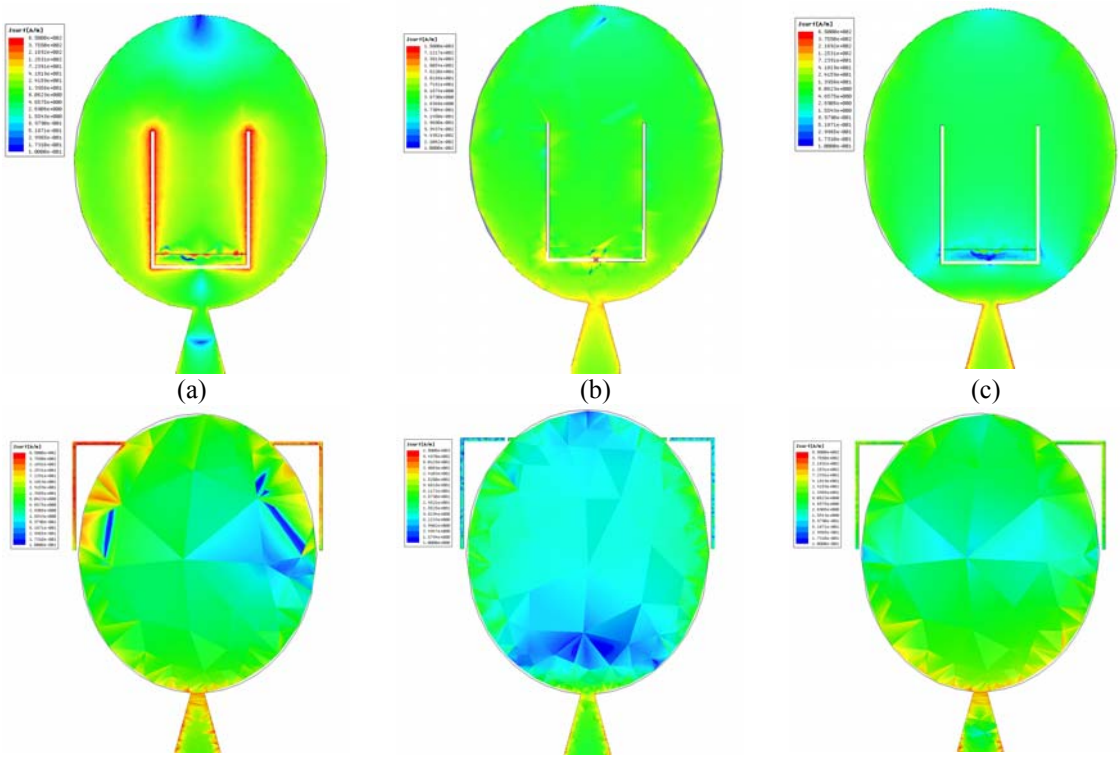

Figure 6.4: Field distribution (a) Open slot at 5.8 GHz (b) Shorted slot at 5.8 GH (c) Open slot at 8 GHz (d) Shorted stubs at 5.8 GHz (e) Open stubs at 5.8 GHz (f) Shorted stubs at 8 GHz.

other as presented in [79]. Therefore they cancel each other and the antenna does not radiate. Once more a transmission line model is used to interpret the inverted L stubs effect on the radiation mechanism where the presence of the two stubs is modeled as a λ/4 long stub. When the MEMS are in up position the stub is disconnected from the primary transmission line (Figure 6.5c) and it has no effect on the incident power which is radiated from the load. When the MEMS are in down position the open stub appears as ideal short on the transmission line and the incident power is reflected as appears in Figure 6.5d.

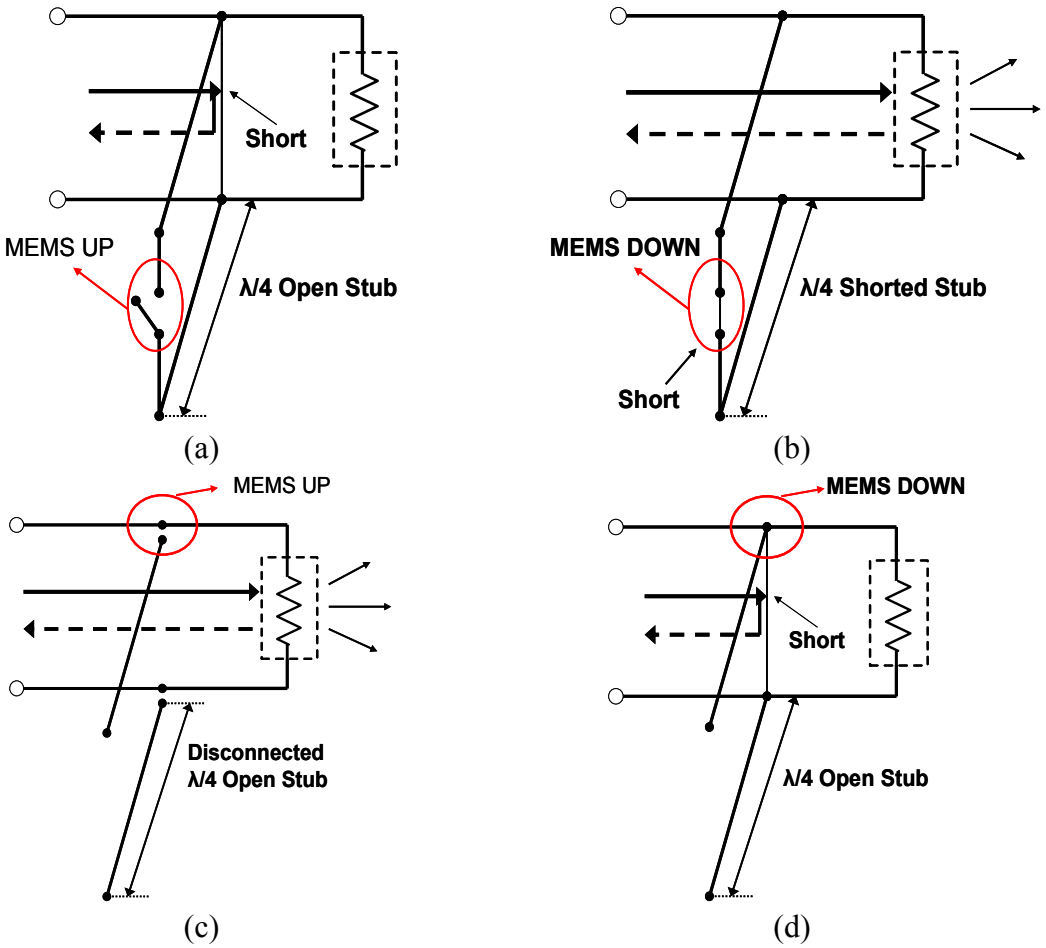

Figure 6.5: Transmission line model for (a) U-shaped slot with MEMS Up (b) U shaped slot with MEMS down (c) Inverted L stubs with MEMS up (d) Inverted L stubs with MEMS down.

6.2.2 Parametric Study

There is a direct inversely proportional relation between the frequency of the band notch and the total length of the resonating elements as can be deduced from the approximation formulas presented in the previous section. This trend is verified numerically from the simulations presented in Figure 6.6. Figure 6.6a shows the simulation results when L_{S1} varies for an antenna with a U-shaped slot where the additional thin slot (3 μmwide) is not present. This simple is referred to as "Simple Slot". When it is compared with the antenna that uses the additional thin slot (similar to the schematic in Figure 6.2) to create the isolated floating ground, which is referred to as "Thin Slot", it can be seen that longer length L_{S1} is required in order to have the frequency notch between 5 and 6 GHz (Figure 6.6b). Specifically for the "Simple Slot" L_{S1}=8.5 mm when for the "Thin Slot" a little longer length L_{S1}=8.8 is needed to cause a band notch in the same frequency range. Additionally for "Thin Slot" when the same length L_{S1}=8.5 is used, the band notch shifts higher, around 6.5 GHz as can be seen in Figure 6.6b. Similar behavior is observed for the length of the inverted L stubs which is presented in Figure 6.6c. The longer the length L_{S2} is, the lower the frequency of the band notch shifts.

Another important parameter is the position of the resonating element. Especially for the U-shaped slot it seems from the simulation return loss results that, the position of the slot is critical. The cut-off frequency is very sensitive with respect to the slot position as can be seen in Figure 6.7a and special care is needed for the selection of the right distance D_1. This probably happens because the slot is close to the feed line transition and therefore the developed currents are stronger. On the contrary a small variation on the

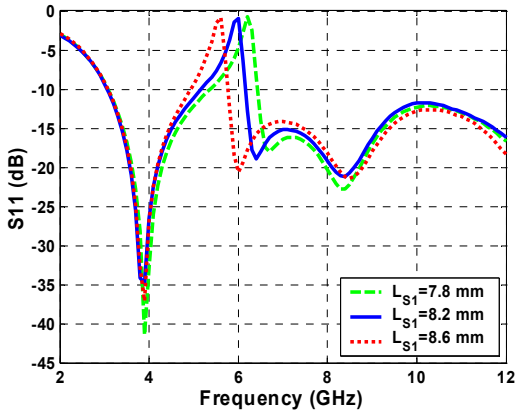

(a)

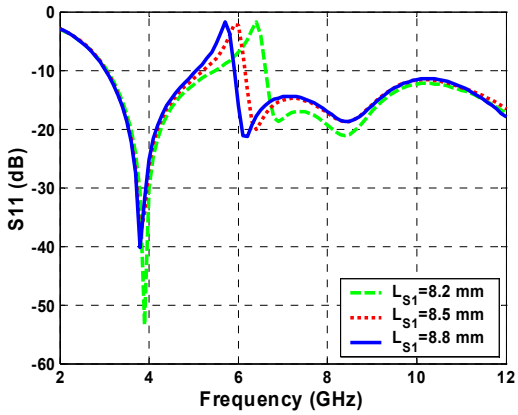

(b)

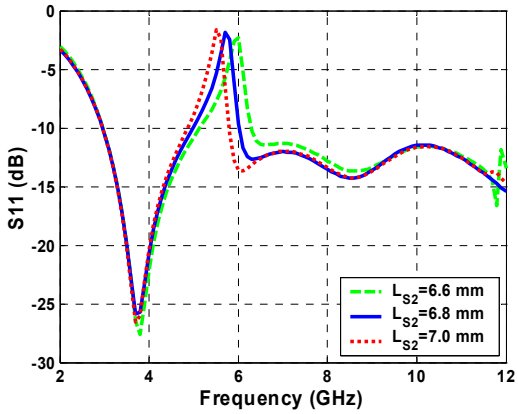

(c)

Figure 6.6: Slot/Stub length effect on return loss (a) Simple slot, (b) Thin slot, (c) Stubs.

distance D_2 of the two stubs from the top point of the ellipse does not seem to affect the band notch significantly because the currents at the edge of the ellipse are not as strong as they are at the intersection of the transition with the elliptical radiator.

6.3 MEMS Switches Fabrication and Integration

6.3.1 MEMS Switches Fabrication

Fabrication and MEMS integration was performed in six general steps. First, the LCP material was polished using an alumina slurry until the surface roughness was approximately 10nm. This roughness is comparable to that of a polished silicon wafer. Therefore, the original polymer roughness has no effect on the switch or the antenna performance. Second, the bottom seed layer was electron-beam deposited. Third, a silicon nitride layer was deposited using Plasma Enhanced Chemical Vapor Deposition (PECVD), patterned, and etched using a Reactive Ion Etch (RIE). Fourth, a sacrificial photoresist layer was patterned to define the switch height. Fifth, a 1.5 μm thick Ti-Al layer was electron-beam deposited and etched to define the switch membranes. Lastly, the switches were released by soaking in photoresist stripper and dried using CO2 at the supercritical point. The schematic of the fabricated switches is shown in Figure 6.8b. Figures 6.8a and 6.8c present switches with different spring constant that require different actuation voltage. Insertion loss, return loss and additional information about the used switches can be found in [80]. The post height is 3 μm and the bridge length 400 μm. A metal pad beneath the switch should be present to attract the charged metal. The metal pad must be placed under a thin dielectric material (such as silicon nitride) to prevent direct metal bridge to metal pad contact. Otherwise, no charge will develop and the switch will not actuate. The fabricated switches are shown in Figure 6.9. They have an

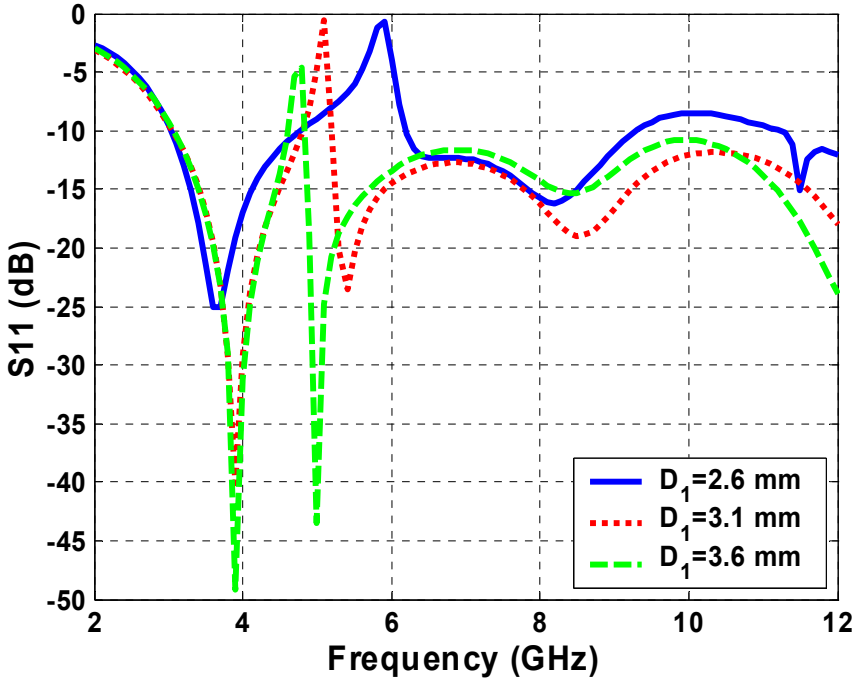

(a)

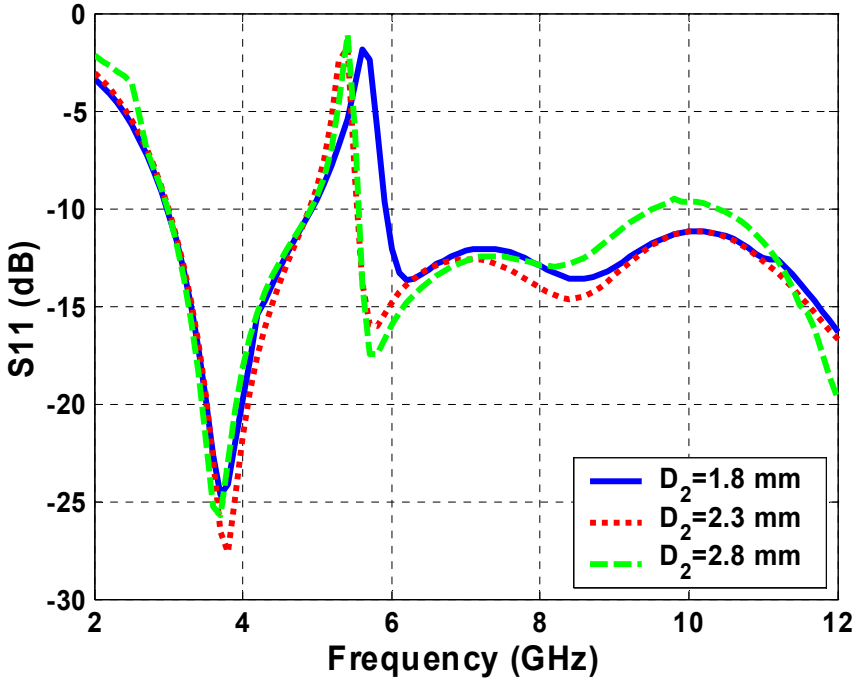

(b)

Figure 6.7: (a) Slot position effect, (b) Stub position effect.

"ON" state (MEMS down) resistance of about 1.7 ohms, and an "OFF" state capacitance of approximately 35 fF. The minimum voltage for the switch actuation is measured at 26.19V.

6.3.2 MEMS Switches Integration

Usually, the actuation voltage is applied via a DC bias line. However, in order to prevent RF leakage into the DC path, careful attention needs to be given to the DC bias lines themselves. This can be implemented in different ways: a) By using a quarter-wavelength transmission line connected to a quarter-wavelength open-circuit radial stub. Alternatively, a half-wavelength transmission line without a radial stub can be used with a reduced bandwidth. b) High-resistance lines have been investigated to provide a wider bandwidth alternative [81]. Aluminum doped Zinc Oxide (AZO) is one such example, used for biasing in [82]. Thin-films of this kind are generally deposited using combustion chemical vapor deposition (CCVD), which uses very high temperatures. This is not a problem for materials like silicon, but it is much higher than the melting point of the organic substrate (315 ^{o}C) used in this work. In any case each MEMS switch would require a different DC bias line. This would have a pronounced effect on the antenna performance. Additionally for the U-shaped slot antenna, because of the geometry, the use of bias lines is impossible with any single layer fabrication. Therefore, the solution of DC bias lines is not advisable. The proposed alternative to these approaches is to eliminate the need for individual switch DC bias lines. Instead, the biasing is handled through the antenna structure itself. Here, the DC voltage and the RF signal are both applied to the antenna through the same signal conductor of the CPW feed line. In the U-shaped slot antenna case the post is placed on the CPW line segment and the bridge is

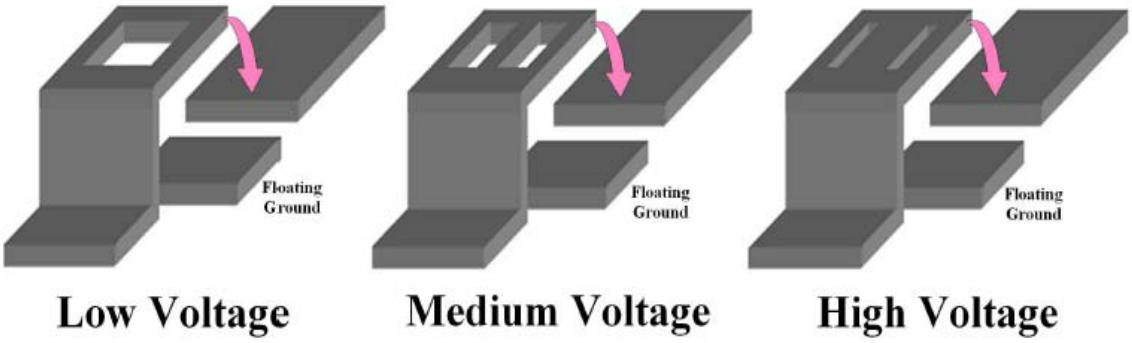

(a) (b) (c)

Figure 6.8: Switch topology.

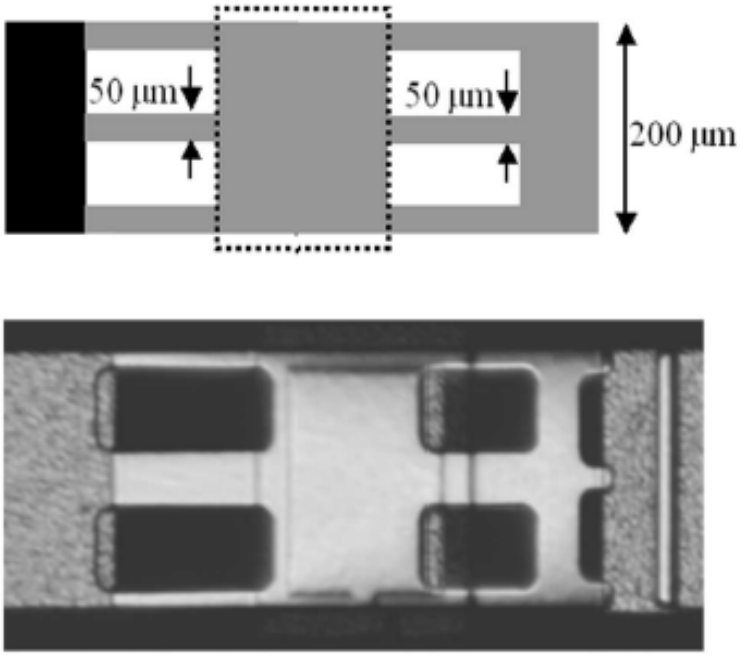

Figure 6.9: Switch schematic.

over the isolated rectangular patch which is surrounded by slot segments. In the inverted L stubs antenna case the posts are fabricated on the elliptical radiator side and the bridges are over the isolated stubs which serve as the floating ground. When a DC voltage of approximately 27 V is applied on the post segment, the bridge is pulled down and the switch switches to "ON" position.

6.4 Measurements Discussion

6.4.1 Return Loss Measurements

For return loss measurements an Agilent 8510 vector network analyzer is used and the input signal is launched through 850 μm pitch GSG probes. The DC voltage for the MEMS actuation is applied through the RF cables and it follows the same path with the RF signal. An S11 measurement is taken when the MEMS are up (OFF state) without applying any DC voltage and another measurement is taken when 28 V DC voltage is applied and the MEMS' bridge goes down, switching to the ON state. The return loss measurements are compared with the "Reference" antenna which is a sample without any resonating elements. Figure 6.10a shows the return loss measurements for the U-shaped slot antenna. The measured S11 plots for the "Reference" antenna and the U-shaped slot antenna when the MEMS membrane is down (MEMS Down) are in very good agreement and when the switch membrane is in up position (MEMS Up) a frequency notch appears between 5 and 6 GHz. In Figure 6.10b the same results are presented for the antenna with the inverted L stubs. The only difference is that the band notch appears when the switch is in down position (MEMS Down) and the "Reference" antenna has similar return loss behavior with the antenna with the switch not actuated (MEMS Up). The presented return

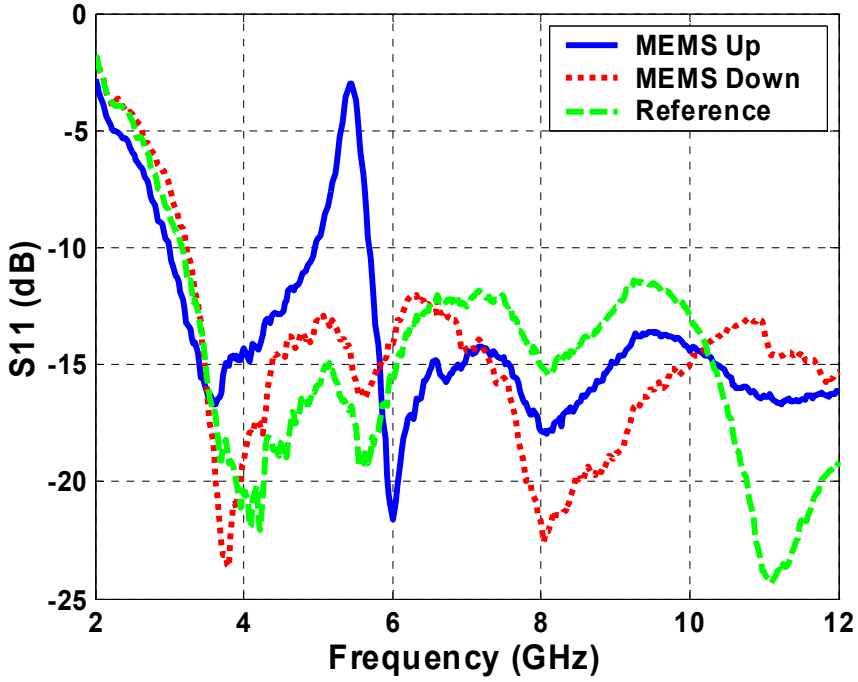

(a)

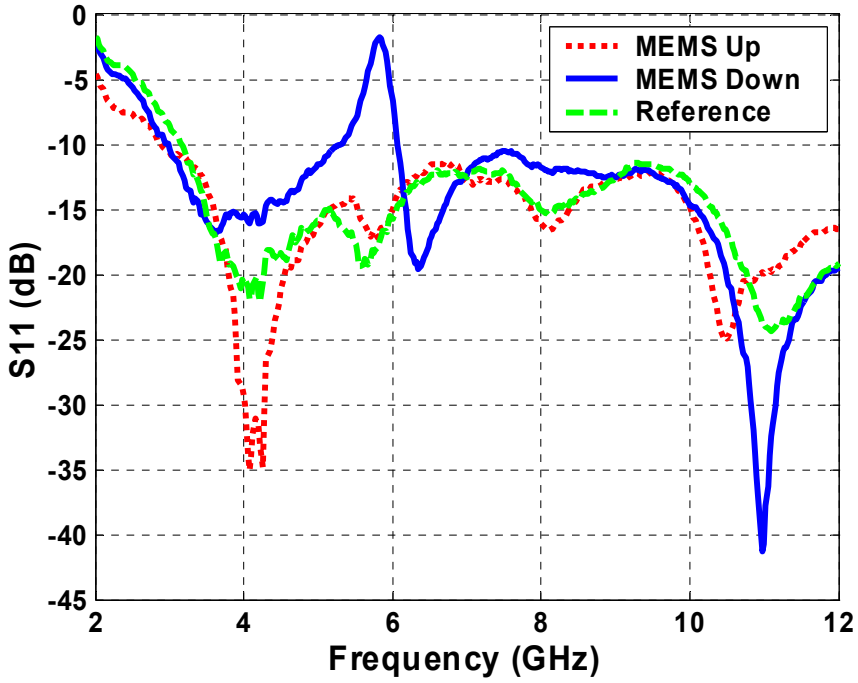

(b)

Figure 6.10: (a) Return loss for antenna with MEMS reconfigurable slot, (b) Return loss for antenna with MEMS reconfigurable stubs.

loss measurements verify the good performance of the MEMS switches and the effectiveness of the suggested integration.

6.4.2 Radiation Pattern Measurements

For radiation pattern measurements instead of the antennas with the integrated MEMS, prototypes where the OFF state was realized with an open circuit, and the ON state was realized with a short circuit, were used. Measurements at 4 and 8 GHz are presented in both E (x-y) (Figures 6.11, 6.12) and H (x-z) planes (Figures 6.13, 6.14). The two states (shorted and open which correspond to ON and OFF states of a MEMS switch) of the reconfigurable antennas are compared with the "Reference" antenna. In all cases the patterns are normalized independently. The general conclusion is that the addition of the resonating elements does not significantly affect the radiation principles of the antennas under detection since the measured patterns are very similar.

6.4.3 Gain Measurements

The antenna gain was measured by using the substitution method with an antenna of known gain, in this case, a second 2 to 18 GHz, Q-par Angus Ltd horn antenna. The "known" gain of the Q-par antenna is specified to be accurate to within ±0.8 dB; thus, this becomes the accuracy of the gain measurements presented in this paper. The gain measurements (Figure 6.15) were taken in the directivity direction which coincides with the z axis direction as it is defined in Figure 6.2. As can be seen the presence of the resonating elements and the frequency mismatch cause a significant degradation on the gain value which is obvious from the dips in the plots that correspond to the gain for the

shorted stubs and open slot antennas. The gain behavior in the other frequencies is similar in all three cases as can be verified from Figure 6.15.

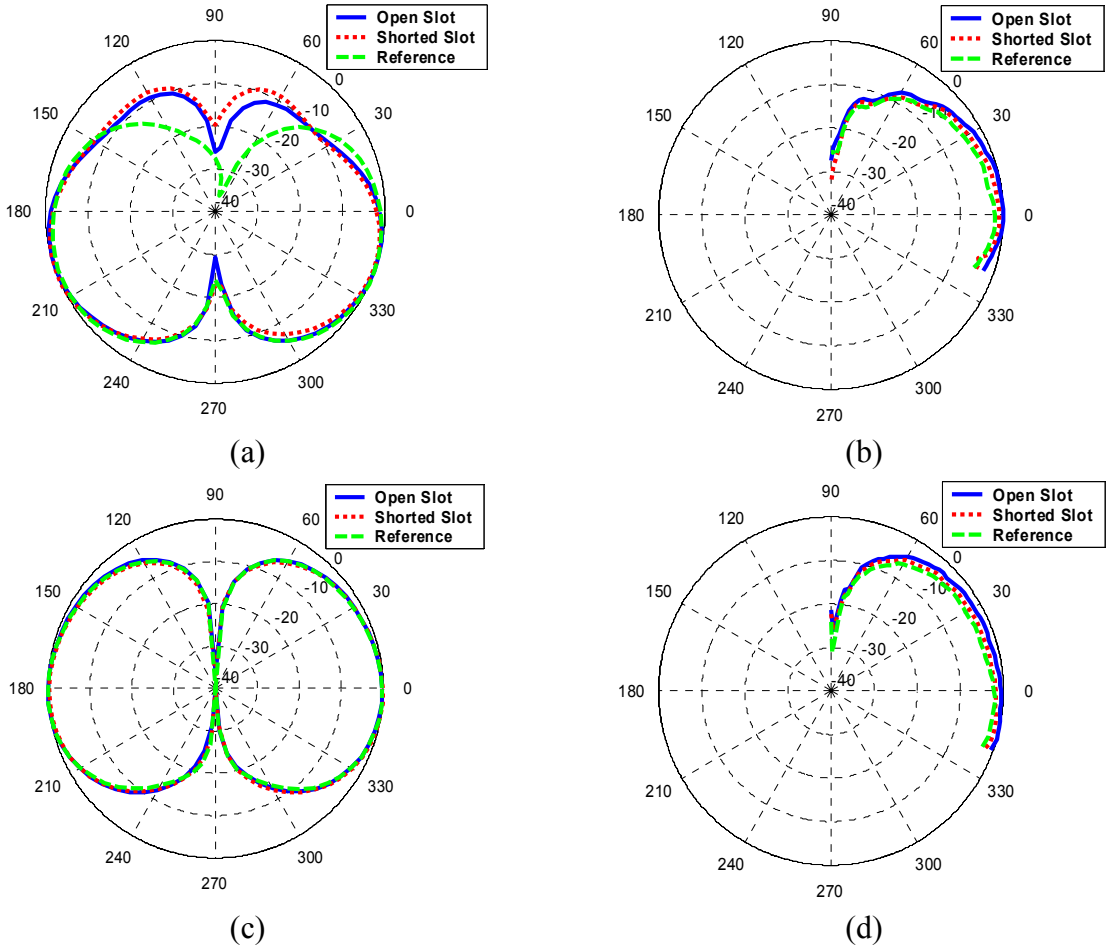

Figure 6.11: U-shaped slot, E plane (a) Simulation at 4 GHz (b) Measurement at 4 GHz (c) Simulation at 8 GHz (d) Measurement at 8 GHz.

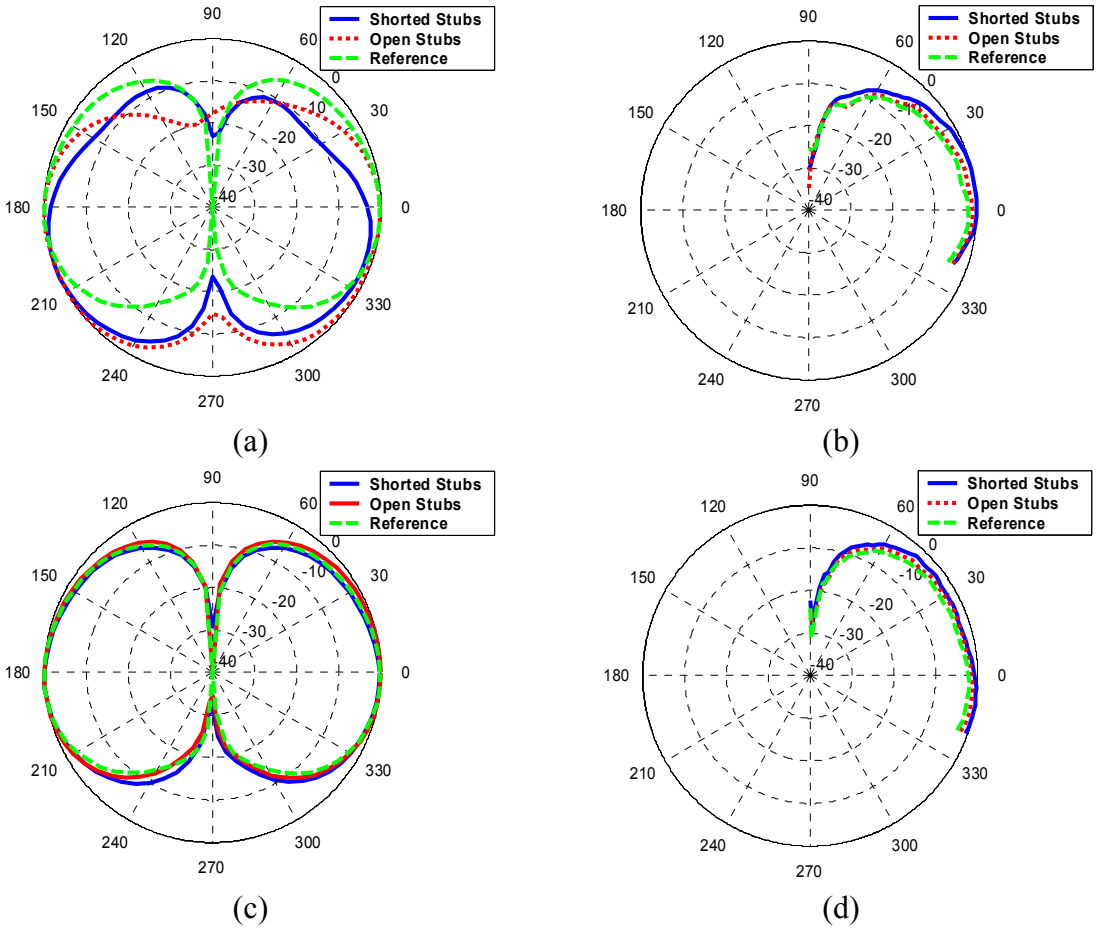

Figure 6.12: L-shaped stubs, E plane (a) Simulation at 4 GHz (b) Measurement at 4 GHz (c) Simulation at 8 GHz (d) Measurement at 8 GHz.

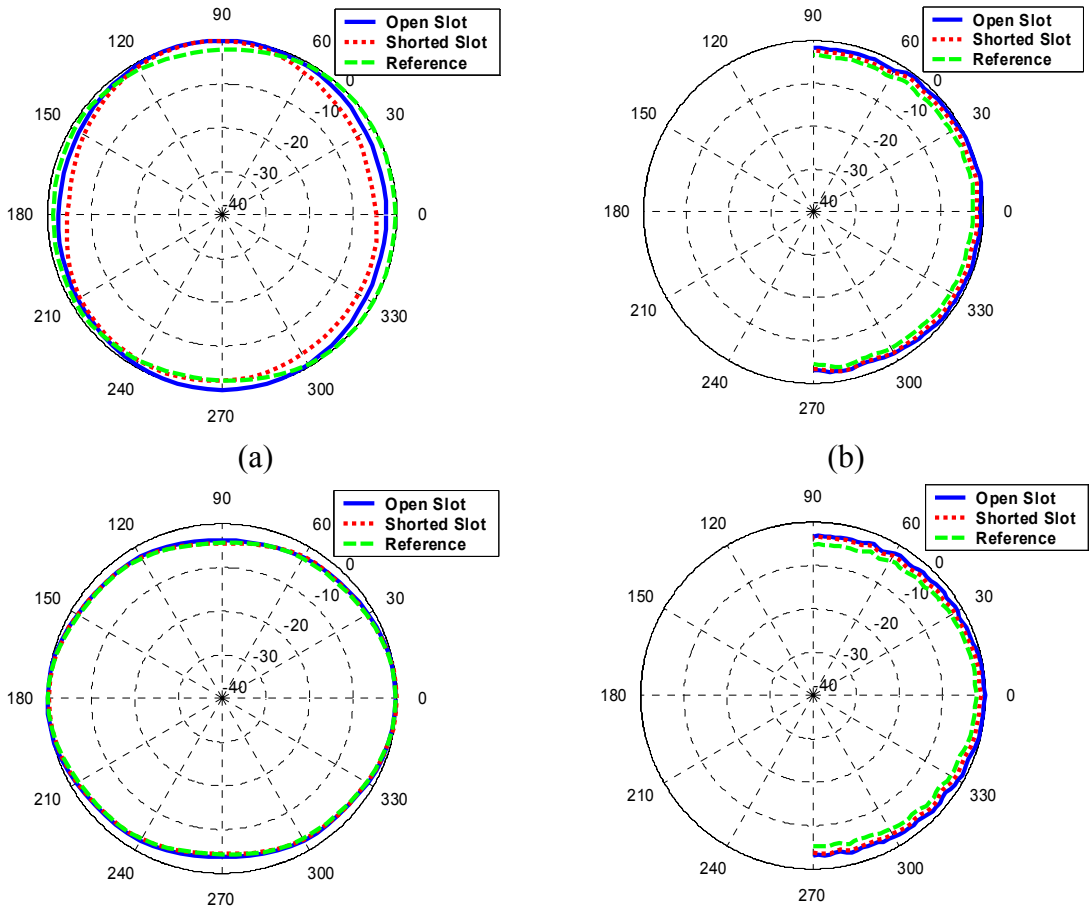

Figure 6.13: U-shaped slot, H plane (a) Simulation at 4 GHz (b) Measurement at 4 GHz (c) Simulation at 8 GHz (d) Measurement at 8 GHz.

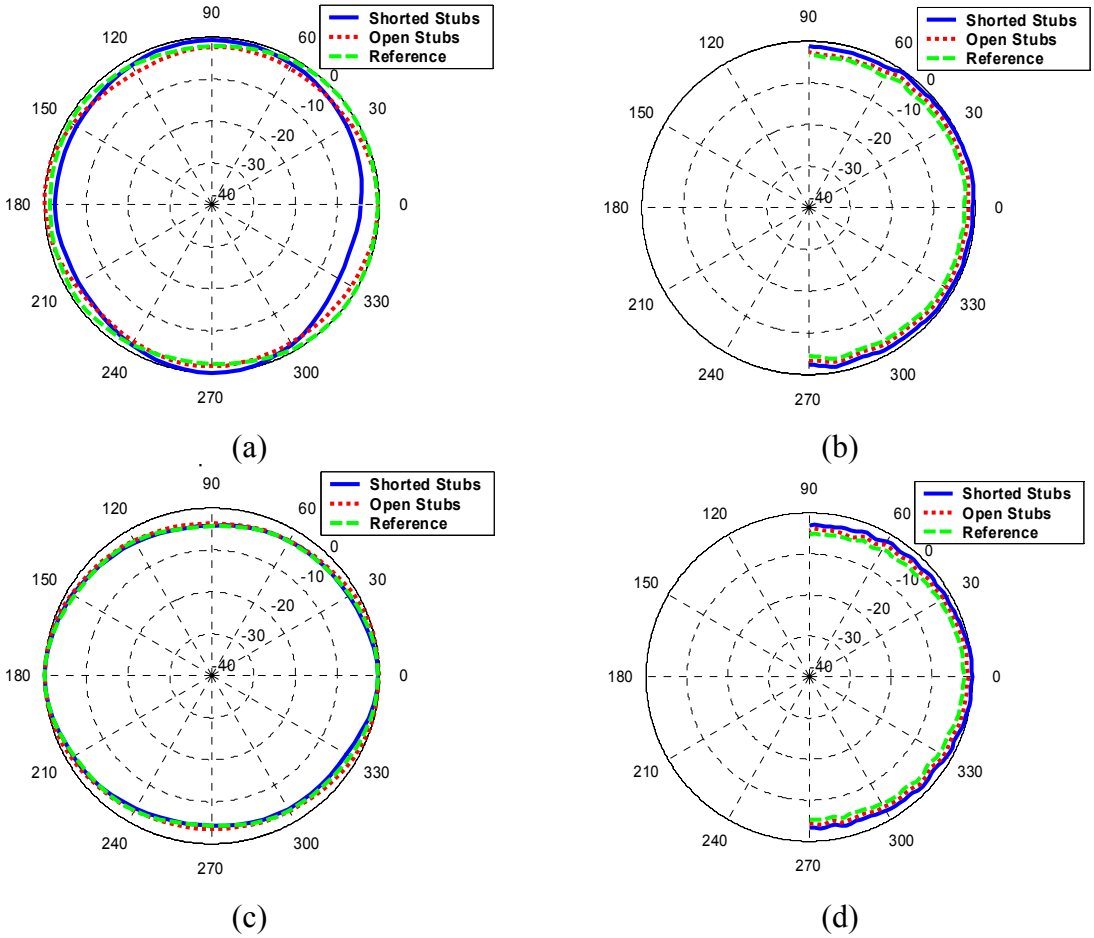

Figure 6.14: L-shaped stubs, H plane (a) Simulation at 4 GHz (b) Measurement at 4 GHz (c) Simulation at 8 GHz (d) Measurement at 8 GHz.

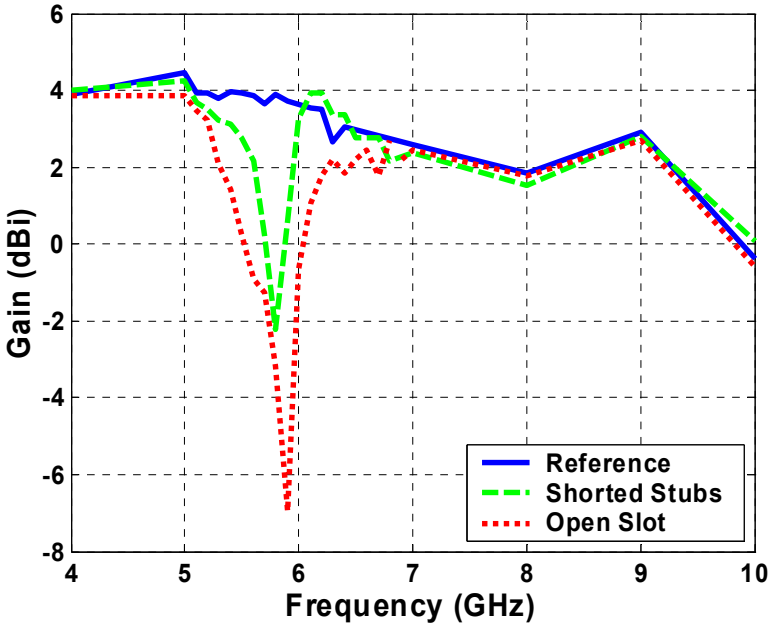

Figure 6.15: Gain measurements.

6.5 Summary

The use of resonating elements integrated with MEMS switches has been exploited to implement two UWB monopoles with reconfigurable band notch in the wireless LAN frequency range. The basic antenna design is an elliptical radiator fed with CPW line, fabricated on thin organic material. In the first case a U-shaped slot of approximate length λ/2 causes the frequency notch and its effect is cancelled by a MEMS switch that shorts the slot. The antenna with shorted slot has the same response with an antenna without any slot, and consequently the state of the single switch defines the presence or not of the rejection band. In the second case two inverted L-shaped open stubs are used and two MEMS switches are used to connect and disconnect the stubs with the elliptical radiator. The electrical connection of the stubs with the radiator causes the creation of the rejection band and apparently when the stubs are not electrically connected the antenna

operates as a typical UWB radiator with radiation band that covers the whole UWB range (3.1-10.6 GHz). Reconfigurability is achieved with MEMS switches that are actuated through the RF signal path, without the need of DC bias lines. The use of MEMS switches which do not need bias liens is very important for reconfigurable antennas because the presence of additional lines on the radiator degrades the radiation performance of any antenna, and especially of a broadband antenna because RF leakage through the bias lines cannot be avoided. Numerical results, transmission line models, and eventually measurements verify the good performance of the proposed antennas which can be good candidates for next generation, high performance and high versatility cognitive radios.

CHAPTER VII

PATTERN AND FREQUENCY RECONFIGURABLE ANTENNAS USING PIN DIODES

The multitude of different standards in cell phones and other personal mobile devices require compact multi-band antennas and smart antennas with reconfigurable features. The use of the same antenna for different purposes, preferably in different frequencies is highly desirable. Moreover, as the number of users of the same spectrum increase, there is an increasing probability of interference between users. Thus, antennas with reconfigurable null positioning are critical.

This work presents the use of pin diodes to reconfigure the impedance match and modify the radiation pattern of an Annular Slot Antenna (ASA). The planar antenna is fabricated on one side of a Duroid substrate and the microstrip feeding line with the matching network is fabricated on the opposite side of the board. The central frequency is 5.8 GHz and, by reconfiguring the matching circuit, the antenna was also designed to operate at 5.2 GHz and 6.4 GHz. Pin diodes are also used to short the ASA in pre-selected positions along the circumference, thereby changing the direction of the null in the plane defined by the circular slot changes. As a proof of concept, two pin diodes are placed 45º on both sides of the feeding line along the ASA and the direction of the null is shown to align with the direction defined by the circular slot center and the diode. Consequently a design that is reconfigurable in both frequency and radiation pattern is accomplished [83].

7.1 Theory of Operation

7.1.1 Design Concept

The annular slot antenna consists of a circular slot on a square, metal ground plane that is fed by a microstrip line fabricated on the opposite side of the substrate as can be seen in Figure 7.1. The mean length of the slot circumference is approximately $3\lambda_s/2$ at the design frequency where λ_s is the equivalent wavelength in a slot transmission line with slot width w [84], which is small compared to λ_s. The microstrip feed line terminates in an open circuit that is approximately $\lambda_g/4$ from the ring where λ_g is the guided wavelength on the microstrip line. At the intersection of the microstrip line and the slot, magnetic coupling occurs, which, due to the $3\lambda_s/2$ ring circumference, creates a null in the radiation pattern in the direction of the microstrip feed line. In Figure 7.1 and all subsequent figures x-y axes are used. The x axis corresponds to $\varphi=0^o$ and the y axis to the $\varphi=90^o$. The radiation patterns and all references on angle positions are consistent with the aforementioned notation. The radiation pattern and the null positioning are explained in detail in the theory section. To change the direction of the null, pin diodes are used to create short circuits across the slot. Generally a null appears opposite to the position where the short is placed, but the short position must be tuned to compensate for discontinuity in the slot fields caused by the feed line to achieve the desired null direction with accuracy. The simulation results indicate that a null can be created anywhere between 15^o and 165^o by adding a short in the opposite direction. For a non-reconfigurable design, the short circuits may be hard-wired slotline short circuits as shown in Figure 7.1, but in the reconfigurable design, they are implemented with pin diodes. The short in the slot results in a reformation of the electric field distribution along

the slot leading to a shift of the null in the short direction. It also changes the equivalent load at the input of the microstrip transmission line; therefore, reconfigurable matching stubs are required to keep the antenna matched at the design frequency during null reconfiguration. Linear matching stubs are also used to match the antenna at different frequencies when the slot configuration is kept constant. As a proof of concept, the antenna is designed to operate at 5.2 and 6.4 GHz in addition to the initial frequency of 5.8 GHz. To reconfigure the matching network, pin diodes are used to connect or disconnect the stubs from the microstrip transmission line and consequently shift the resonance to the desired frequency.

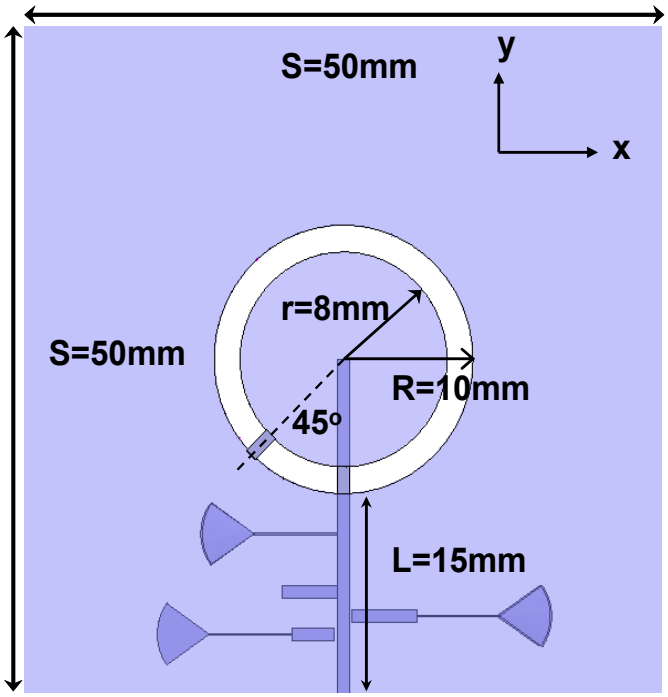

Figure 7.1: Annular Slot Antenna schematic. The feeding line with the matching stubs are on the bottom and the annular slot antenna is on the top side of the substrate. The short is placed at φ=225º, else 45º far from the feeding line.

7.1.2 Pattern Reconfigurable Principles

The radiation patterns of the shorted ASA yield a null in a direction different than the feeding line direction, which is the case for the regular, unperturbed slot. The simulated x-y plane radiation patterns for the case of a hard-wired short circuit at 225º are presented in Figure 7.2. In that plane the E field is polarized in φ direction, parallel to the slot plane. The null is created in the x-y plane instead of the broadside direction because it is meant to decrease the effect of an interferer coming from a direction different than the directivity (maximum field value) direction, which is parallel to z axis. At 5.8 GHz, for which the slot dimensions are optimized, a null exists exactly opposite to the slot short with respect to the slot center. At 6.4 GHz, the null appears approximately 10º

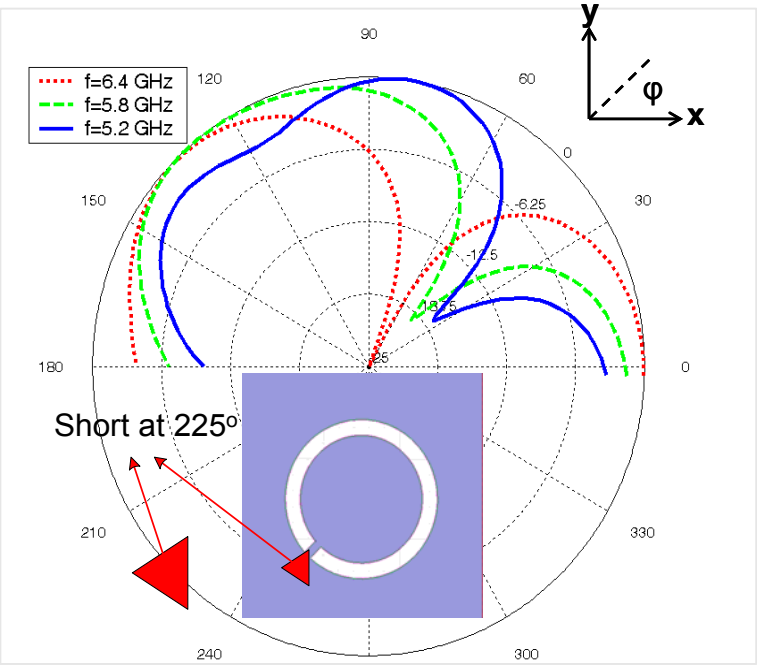

Figure 7.2: Simulated normalized radiation patterns on the x-y plane with a short circuit at 225º. The null direction for the slot without any short would be in the 90º direction with respect to the plot labeling.

closer to the 90^o direction, while at 5.2 GHz, the null deviates from the 90^o direction and moves closer to the 0^o direction by 5º. Similarly, placing a short circuit at 315º, results in a null in the radiation pattern at 135º for 5.8 GHz. As a more general concept, when a frequency lower than the design frequency is used, the null shifts towards the $\varphi=90^o$ direction while it shifts towards the $\varphi=0^o$ direction when a higher frequency than the design frequency is used.

As discussed, varying the null position changes the impedance of the antenna and requires a reconfigurable matching circuit. When a short is placed at 45º from the feeding line, as shown in Figure 7.1, a single stub with length 4.21 mm and width 0.92 mm at a distance of 7.27 mm from the feeding point is used to match this short position at 5.8 GHz. When the short is removed, simulating the case that the diode is not biased, a second stub must be added as a shunt matching device at the feeding line in order that the resonance frequency remains constant. The technique to define the stubs' length and their position is explained in the next section. Return loss simulation and measurements are presented in Figure 7.3, where it is seen that a 5.8 GHz resonant frequency is maintained regardless whether or not a short exists. The 4.5 GHz parasitic resonance, when no short circuits occur on the ring, is easily removed by filtering it with a microstrip passband filter that can be cascaded to the antenna geometry.

To qualitatively explain the shift in the null direction when a short is placed along the slot, a novel but simple model using magnetic dipoles is introduced and briefly discussed. The field distribution as a result of a numerical simulation using HFSS is presented in Figure 7.4. Based on the field distribution, the dipole model presented in Figure 7.5 is proposed, which consists of three magnetic dipoles of length $\lambda_s/2$ with

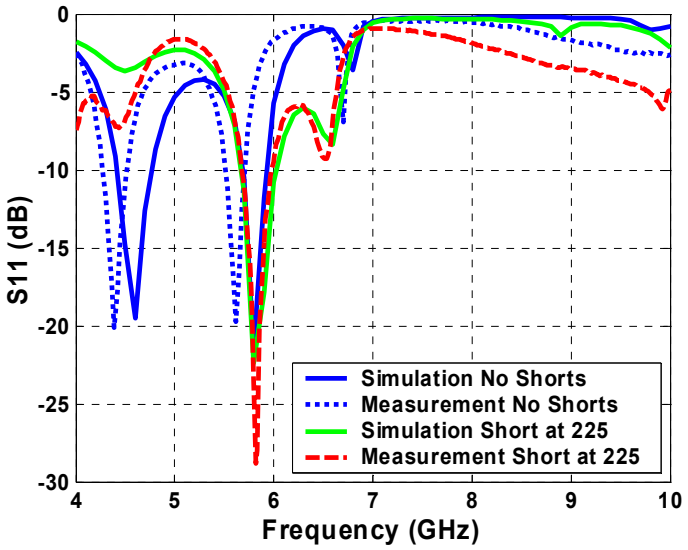

Figure 7.3: Simulation and measurement results for the null reconfigurable design. The first two lines refer to the design without any short. The numbers in the label refer to the hard-wired short position compared to the polar plot label in Figure 7.2.

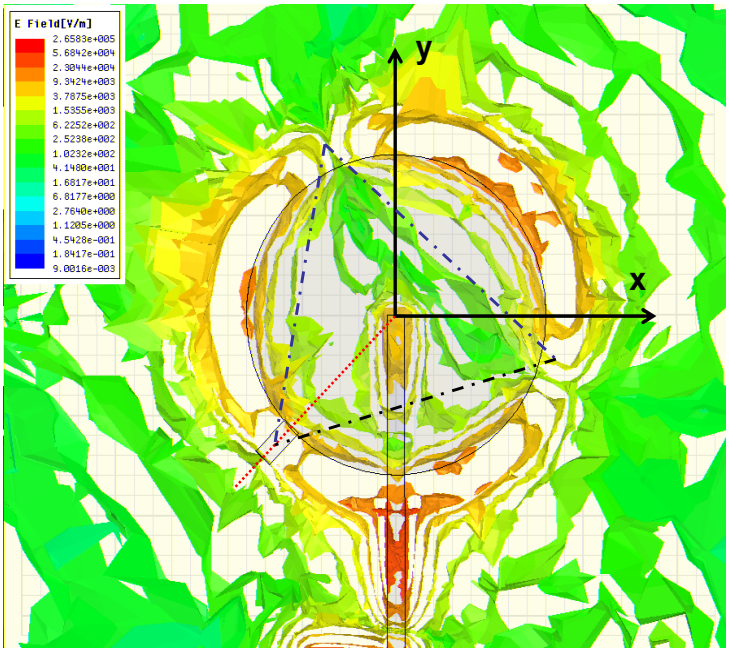

Figure 7.4: Electric field distribution for f=5.8 GHz when a short is placed at 225º. The dipoles model is superimposed for comparison.

sinusoidal magnetic current excitation. The $\lambda_s/2$ magnetic dipole is the dual equivalent to the $\lambda/2$ electric dipole. The electric field component E on a plane that includes an electric dipole with length 'l' is given by [85]. Based on the duality principle [85] the E field derived from a magnetic dipole is presented in (7.1), where k is the wavenumber, r is the distance from the dipole's center and M_o the amplitude of the magnetic current excitation. The angle θ is the elevation angle measured from the z axis which is parallel to the dipole. The dipoles for the proposed model lay on x-y plane therefore the azimuthal angle φ is used in (7.2) but the expression applied for each one dipole is still the expression in (7.1).

$$E(\theta) \propto -j\frac{M_o e^{-jkr}}{2\pi r}\frac{\cos\left(\frac{kl}{2}\cos\theta\right)-\cos\left(\frac{kl}{2}\right)}{\sin\theta} \tag{7.1}$$

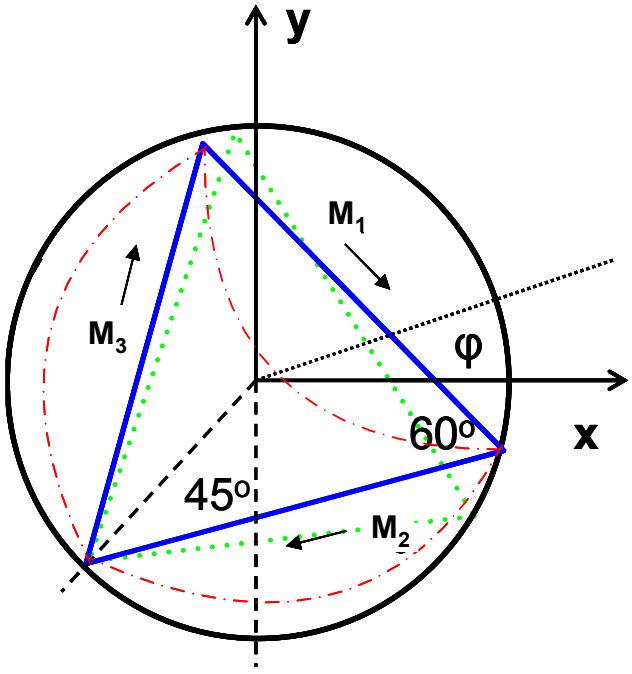

Figure 7.5: Magnetic dipoles model of ASA with short circuit at 225º. Three dipoles are used in equilateral triangle orientation (Blue solid lines are for 5.8 GHz and green dotted lines for 5.2 GHz).

The superimposed electric field as a result of all three dipoles is given by (7.2) and is plotted in Figure 7.7 in polar coordinates.

$$E = \left| e^{j\delta_1} E_1(\phi + \frac{\pi}{4}) + e^{j\delta_2} e^{-jkd_2} E_2(\phi + \frac{\pi}{4} + \frac{2\pi}{3}) \right.$$
$$\left. + e^{-j\delta_3} e^{-jkd_3} E_3(\phi + \frac{\pi}{4} - \frac{2\pi}{3}) \right| \tag{7.2}$$

The phase shift $\pi/4$ is used to take into consideration the respective dipoles' orientation with respect to the reference axes. There is also a $2\pi/3$ angle between two consecutive dipoles which must be considered. In Figure 7.6 the magnetic current and phase distribution along the annular slot, are presented as derived from the electric field distribution presented in Figure 7.4. The magnetic current distribution presented in Figure 7.6 matches the magnetic current distribution calculated and measured for the shorted annular slot, presented in [86].

For expression (7.2) the amplitude and phase for each magnetic current excitation must be estimated. The phases and amplitudes for the dipoles' currents for f=5.8 GHz are calculated from the solid lines in Figure 7.6 using the technique applied in [87]. The phases, δ_1, δ_2 and δ_3 are the phases of the current excitations and are calculated as the mean values of the continuous phase distribution in the corresponding segment, as shown in Figure 7.6b. Therefore from Figure 7.6b the phases are estimated as δ_2=-20^o, δ_1=-180^o and δ_3=20^o. The current amplitudes are normalized with respect to the strongest current M_2, which is the current on the segment where the excitation is applied. From Figure 7.6a $M_1=0.9M_2$ and $M_3=0.7M_1$ are deduced. The amplitudes descent in that order, because of the traveling wave which is excited on the ring that attenuates as it propagates away from the excitation source. The path difference between E_1 and E_2, is $d_2=(\lambda/4)\cos(60-\varphi)$ while the path difference between E_1 and E_3 is $d_3=(\lambda/4)\cos(120-\varphi)$ and can be easily deduced

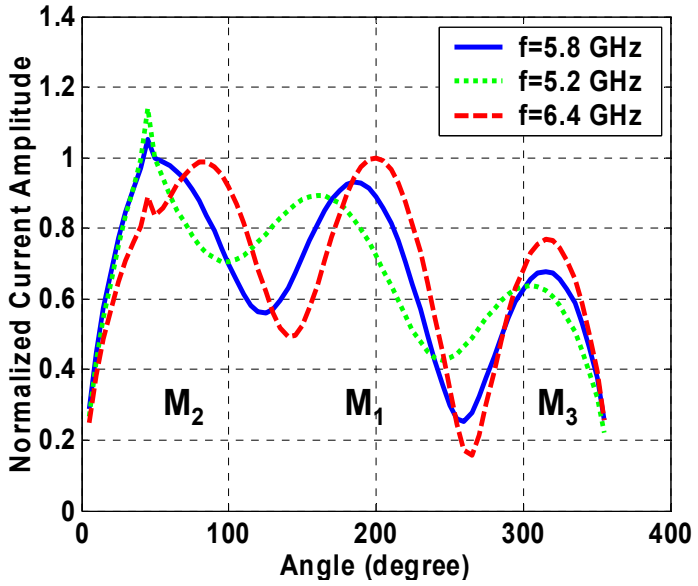

(a)

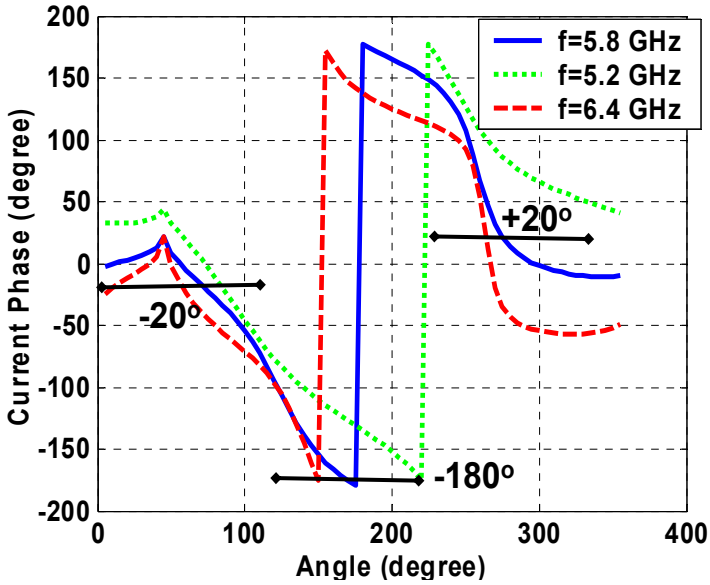

(b)

Figure 7.6: (a) Magnetic Current amplitude distribution along the annular slot, (b) Magnetic current phase distribution along the annular slot. The 0 corresponds to the short position. The singularity at 45° is due the excitation source. The phases and normalized amplitudes correspond to M_2, M_1 and M_3 from left to the right.

geometrically. The normalized magnetic current excitations and the phases used, apply for any design frequency for which the annular slot length is $3\lambda_s/2$. The antenna prototype can be scaled for a different frequency without affecting the validity of the model.

The analytical model predicts the null position and matches the numerical solution with satisfactory precision as shown in Figure 7.7 for the central frequency, f=5.8 GHz. Measurements and the numerical solution show a shift in the null position as the frequency changes, which is predicted by the dipole model. At a different frequency, the slot circumference is no longer $3\lambda_s/2$ and a different field distribution occurs. As a result the magnetic dipoles do not maintain their orientation with respect to the axes, but they rotate slightly instead. For the lower frequency, the wavelength is about 10 % longer and therefore the magnetic dipoles structure is rotated clockwise with the point at the short fixed. The current distribution for f=5.2 GHz, for the dipole with M_2 excitation requires a longer segment along the ring (dotted line Figure 7.6a) compared to the current 5.8 GHz. The $\lambda_s/2$ length at 5.2 GHz is about 10% longer than the one for 5.8 GHz so the dipoles structure is rotated clockwise with the point at the short fixed (dotted straight lines in Fig. 5). The dipole with currents M_1 and M_3 behave accordingly. The dipole with M_2 needs to be slightly shorter than $\lambda_s/2$ since it terminates at the short position and it overlaps with the feeding line. However it still remains close to $\lambda_s/2$. Therefore the same analytical expression (2) is used with the offset angle to be slightly greater than $\pi/4$. That results in the rotation of the entire radiation pattern by the same offset angle clockwise as can be seen in Figure 7.2. For the same reason, the use of a higher frequency at 6.4 GHz results a counter-clockwise rotation of the null direction. The proposed model aims primarily to give a qualitative explanation in the null shifting; therefore absolute agreement with the

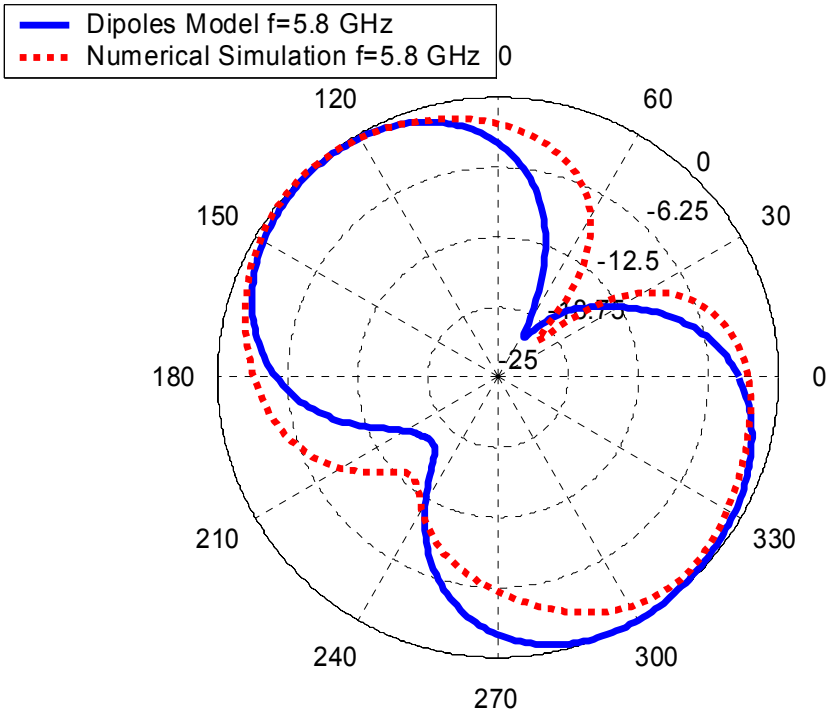

Figure 7.7: Analytical expression plot of ASA with short circuit at 225º compared to the numerical solution for the amplitude of E field.

numerical solution should not be expected. The microstrip feed line and the matching circuits, which are only on one side of the ASA only, destroys the symmetry. Therefore the null is stronger in the direction opposite to the feeding line as can be seen in Figure 7.7 where the simulation results in all 4 quadrants are presented.

7.1.3 Reconfigurable Matching Network

The ASA using various feeding techniques has been shown to have a relatively wide bandwidth compared to a patch or other narrowband antennas [88]-[89]. For the design dimensions used in this prototype, simulations predict radiation efficiency greater than 80% over the frequency range from 4.8 GHz to 6.5 GHz. Since the radiating element can

radiate over a wide range, the matching network must also support a broad bandwidth. Moreover, the use of diodes to create shorts in the annular ring for null reconfiguration also affects the input impedance, and this also must be accounted for in the matching circuit. Instead of a broadband matching network, a reconfigurable matching network employing stub tuners was designed to support three narrowband frequency ranges. At the center frequency of 5.8 GHz, the input admittance was determined from the simulations, and this admittance was transferred along the 50 Ω microstrip line to the point where the admittance had a real part of 0.02 siemens (=1/50 siemens) and a random imaginary part. At that point, an open circuit microstrip stub was placed parallel to the transmission line to cancel the imaginary part. For the other frequencies, the impedance at the port needs to be determined with the first matching stub in place so the other two frequencies are matched using the combination of two stubs for each one of them. Those additional stubs have been shown not to affect in any way the radiation pattern. As an extension of section's 7.1.2 experiment for the validation of the frequency reconfigurability, the short on the slot is placed at 45º from the feeding line, namely at 225^{o}. Because of symmetry, the same matching stubs can be used when the short is placed at the symmetrical position 45º towards the opposite direction, which is at 315^{o}. In order to investigate the effect of the diodes, three different designs with the correct matching network hard wired for each of the three frequencies were tested. The return loss plots are presented in Figure 7.8. Simulations and measurements are in good agreement, with a small shift downwards for the 6.4 GHz resonance, which could be a result of fabrication inaccuracy and imperfect connector soldering.

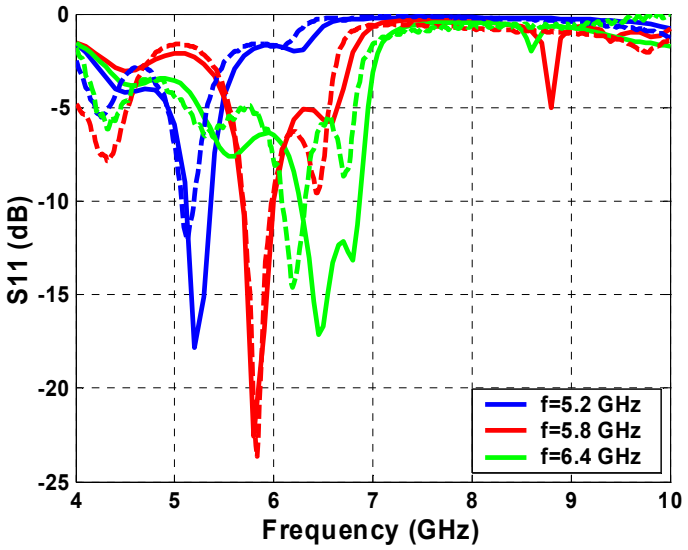

Figure 7.8: Simulation and measurement are presented for the three different frequencies. Simulation is presented in solid line and measurement is presented in dashed line.

7.2 Antenna Design Description

7.2.1 Pattern Reconfigurable Principles

A layout of the front side of the antenna with the matching stubs designed as described in section 7.2.3 is presented in Figure 7.9. For shorting and opening the stubs to the feeding line, ASI 8001 PIN diodes are used, which will be referred to as 'small' diodes. Their length is less than 200 μm. On the annular slot, MBP-1035-E28 PIN diodes are used, which will be referred to as 'big' diodes. They are long enough to cover the 2 mm slot width. The matching network for the frequency reconfigurable design with a "big" diode biased at 45º along the ASA is shown in Figure 7.9. Three stubs of length L1, L3, and L2 are used to match the slot antenna to 5.2, 5.8, and at 6.4 GHz respectively. The DC bias lines are used to apply the DC voltage to the small diodes. When neither of the small diodes is biased, the antenna is matched at 5.8 GHz, by forward biasing the diode on the stub of length L1, the antenna is matched at 5.2 GHz, and by forward biasing the diode

on the stub of length L2, the antenna is matched to 6.4 GHz. The reconfigurable matching network dimensions are presented in Table 7.1.

In Figure 7.9 the 200 μm gaps (between the tapering small triangles and the feeding line) for the small diodes can be seen. The radial stubs are 70º wide and all the microstrip lines are 0.92 mm wide which results in a Zo of 50 Ω. The thin feeding lines are 120 μm wide and are used as DC bias lines. Their respective lengths are optimized for the frequency used, so they are equivalent to an open for the RF signal while they are perfect conductors for any applied DC current. The dc lines however are thin enough (very high RF impedance) to prevent leakage for the frequencies for which they are not optimized. Tapered segments are used to match the wider linear stubs to the small diodes in order to minimize reflections.

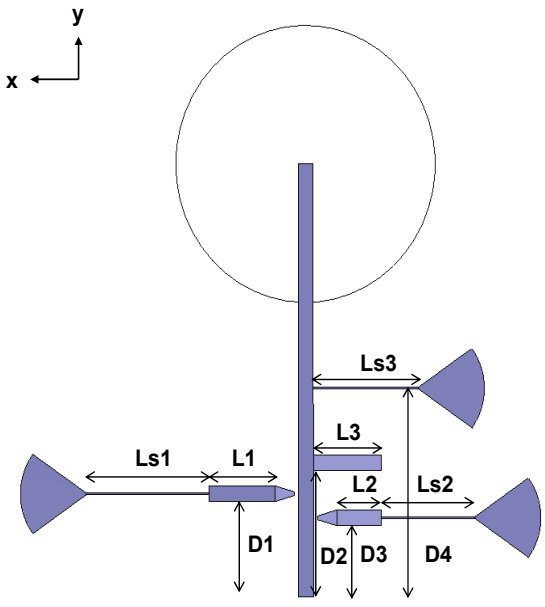

Figure 7.9: ASA frequency reconfigurable design matching network.

Table 7.1. Dimensions of circuit elements for frequency reconfiguration and null at 45º.

Symbol	Value in mm
D1	5.49
D2	7.27
D3	4.10
D4	12.08
L1	4.05
L2	2.75
L3	4.21
Ls1	7.60
Ls2	5.75
Ls3	6.50

7.2.2 Null Position Reconfigurable Design

For the null reconfigurable design, two stubs are used to match the antenna for the two cases; when there is a short at ±45º away from the feeding line, and when no short exists along the circumference. Consequently one small diode is used for the activation of the matching stubs and two big diodes for the null control. When the small diode is not biased and one of the two big diodes is biased, the antenna is matched at 5.8 GHz. Note that this corresponds to the same matching network in Figure 7.9. When none of the big diodes are biased and the small diode is biased, the antenna is matched at 5.8 GHz and a null appears in the direction opposite to the feeding line. As a result, for a fixed frequency at 5.8 GHz a null in three different directions (-45º, 0º, and +45º) can be created. The matching network design is presented in Figure 7.10 and the dimensions are presented in Table 7.2.

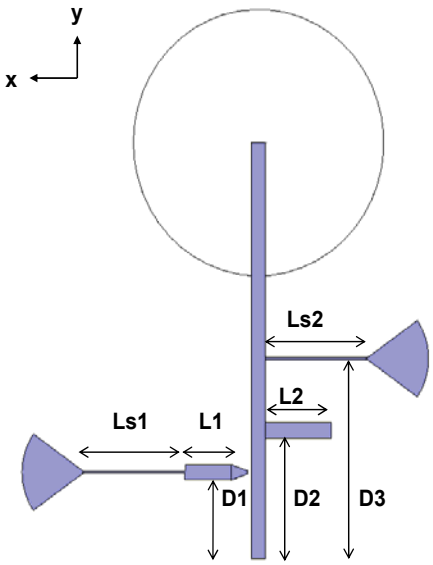

Figure 7.10: ASA Null reconfigurable design matching network.

Table 7.2: Dimensions of circuit elements
for null reconfiguration at 5.8 GHz.

Symbol	Value in mm
D1	4.75
D2	7.27
D3	12.08
L1	2.97
L2	4.21
Ls1	6.50
Ls2	6.50

7.2.3 Antenna Fabrication

The antenna was fabricated on a 635 μm thick Rogers RO3006 substrate with ε_r=6.15 and tanδ=0.0025. The antenna is fed by a 50 Ω microstrip line. A standard photolithography technique was used for fabrication. The copper thickness was 18 μm and the alignment between the two copper layers was achieved by drilling holes on the substrate using a laser method. Big and small diodes can be seen in Figure 7.11 and Figure 7.12, respectively. A current smaller than 10 mA, was used to forward bias the diodes. For the small diode bias, dc bias lines were used and a wire carrying the bias was soldered to the radial stub. For the big diodes, the ground plane was grounded and a wire was soldered to the inner section of the ring. For return loss and radiation pattern measurements a 3.5 mm SMA connector was soldered at the beginning of the feeding line.

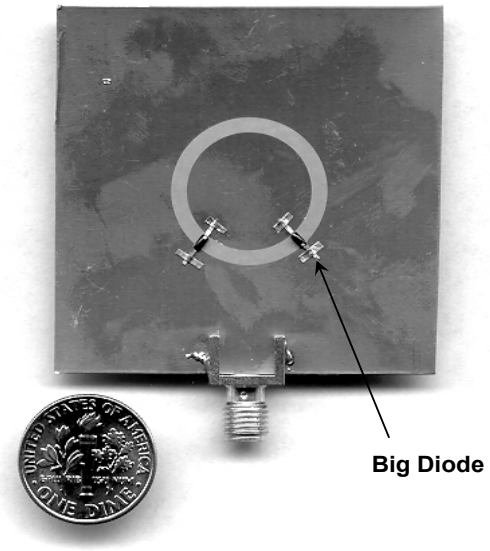

Figure 7.11: Photograph of the front side of the annular slot antenna. Two MBP-1035-E28 PIN diodes are observed, soldered symmetrically 45^o from the feeding line.

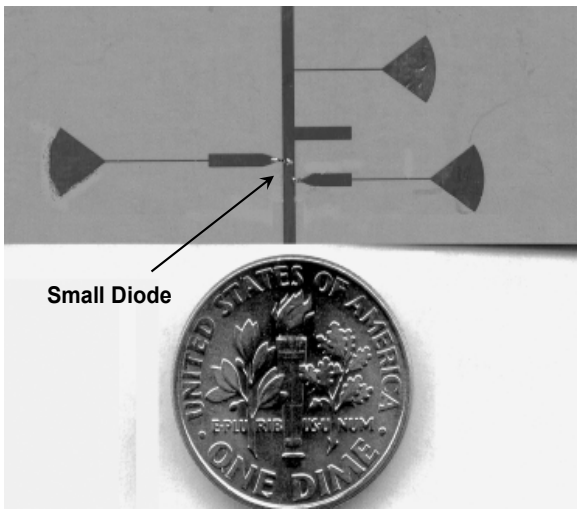

Figure 7.12: Photograph of the back side of the frequency reconfigurable design. Two ASI 8001 PIN diodes are observed connecting the matching stubs to the feeding line. The dc bias lines are also visible.

7.3 Experimental Results Discussion

7.3.1 Diodes' Effect in Return Loss

The small diodes are used to electrically connect the matching stubs to the transmission line. When the diodes are soldered onto the board but are not biased, they are equivalent to a small capacitive load (0.08 pF) and behave as if they do not exist for the frequencies of interest. That was verified in both return loss measurements and radiation pattern measurements. Return loss measurements to demonstrate the "small" diode effect are shown in Figure 7.13.

When the diode is biased, the circuit is designed to match at 5.2 GHz, which is close to the measured resonant frequency in Figure 7.13. When the diode is not biased, the antenna is designed to be matched at 5.8 GHz. The measurement with the diode not biased is compared to the reference hardwired design of Figure 7.13 with no diodes on, and very good agreement is observed.

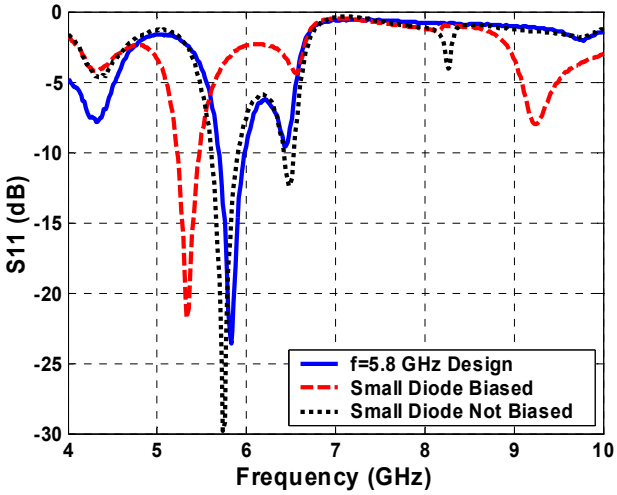

Figure 7.13: Small diode effect in the frequency reconfigurable design for the 5.2 GHz stub.

A small shift in the resonance frequency is consistently observed when a big diode is biased along the slot. The capacitive load on the circumference results in a downwards shift of the resonance frequency as discussed in [90]. For the null reconfigurable design, the coexistence of two diodes on the slot with one of them forward biased and the second one reverse biased results in a parasitic resonance close to 6.5 GHz, as seen in Figure 7.14. This is because of the additional capacitive load as a result of the reverse biased diode. The parasitic resonance can be filtered with a cascaded microstrip passband filter for the single frequency (5.8 GHz) null reconfigurable antenna. For the extension to multiple frequencies, the parasitic will be taken care of with the appropriate matching configuration. For the simulation, the reverse biased diode was simulated as a perfect open and that is why the parasitic resonance does not appear in the simulation. There is still a good resonance at the design frequency which is consistent for all three directions of the null and is measured at 5.65 GHz which is less than 3% off the design frequency.

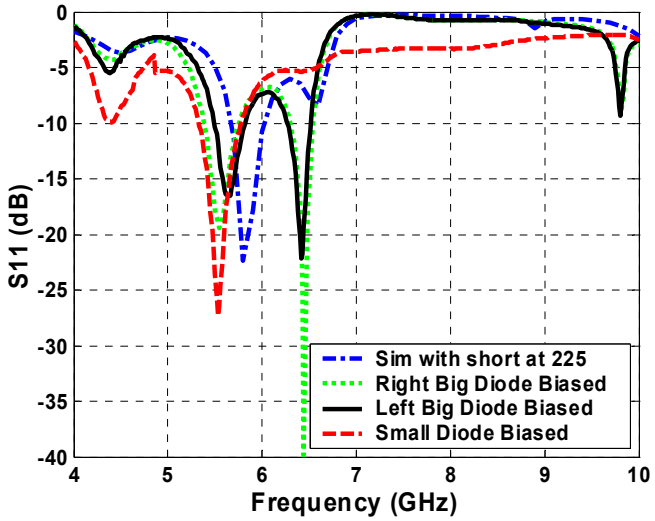

Figure 7.14: Diodes effect in return loss measurement for the null reconfigurable design. The design frequency was 5.8 GHz.

7.3.2 Radiation Pattern Measurements

A far field antenna test range was used to characterize the ASA. In the test range, the ASA was the receiving antenna that rotated through the ϕ plane while a 5.4-8.2 GHz, 15 dB standard gain horn was used as the fixed, transmitting antenna; the two antennas were separated by 1 m. The transmitted RF signal was AM modulated by a 20 MHz signal that was detected by a diode detector and measured by a lock-in amplifier. Control of the rotary stage, lock-in amplifier, and data recording was automated. To bias the diodes, wires were soldered to the center of the ASA and the radial stubs of the matching circuit. In addition, a bias tee was used to ground the microstrip line and to isolate the applied bias from the diode detector. Because the ASA radiates backward as well as forward, the coaxial launcher, bias tee, and detector were sandwiched between 1 cm thick pieces of absorbing material. During test, it was observed that the substrate corners had to be rounded to minimize reflections and diffractions at the corners that caused ripples in the

radiation pattern. Before characterizing the ASA, a variable attenuator was used to vary the input power in order to calibrate the diode detector and determine the radiated power that results in maximum detector sensitivity.

7.3.3 Diodes Effect in Radiation Pattern

The effect of both the small and big diodes on the radiation patterns was investigated and is presented in the current section, and the radiation patterns are compared to the simulation results (ideal elements) and to the hard-wired design measurements presented earlier. In Figure 7.15, the measured radiation patterns for the E_{φ} component of the electric field, which is the component parallel to the antenna substrate, for all three frequencies and a hardwire short at 225º are shown, In addition, the measured radiation pattern at 5.2 GHz for a regular slot without any short along the slot is shown.. The results in Figure 7.15 have similar behavior to the simulated results presented in Figure 7.2 in section 7.1. The shift in the null direction with respect to the frequency that was explained in a previous section is hereby verified experimentally.

Figure 7.16 and Figure 7.17 present the measured radiation patterns for frequencies of 5.2 GHz and 6.4 GHz respectively with diodes used to short the slot. They were in very good agreement with the simulation and the hard-wired measurements. This proves that the PIN diode is a suitable switch for this application. The effectiveness of the small diodes has been verified in designs other than antennas, like filters [91] and it only has to do with the matching network. The parasitic capacitance and resistive load of the big diodes that differentiate them from the ideal short circuit, on the other hand, have been hereby proven experimentally not to distort the radiation pattern in comparison to the

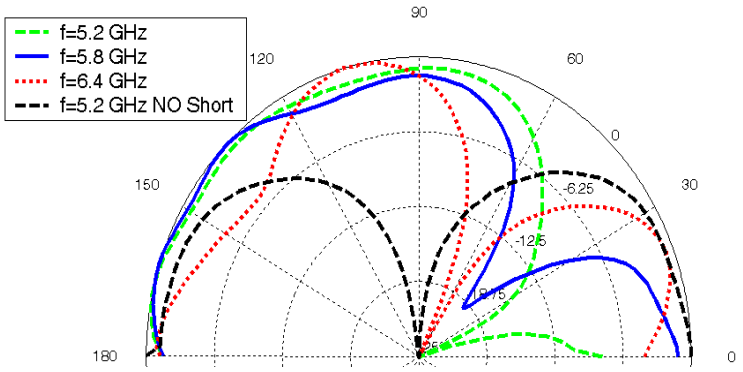

Figure 7.15: Measured radiation patterns for the design frequencies when a hard- wired short is placed at 225^{o}.

ideal elements. The short was placed in symmetrical positions with respect to the feeding line direction in order to show that the results are not dependent on the side of the short and are not affected from the non symmetric matching stubs. The behavior of the antenna is equivalent for both sides of the short.

In the plots presented in Figures 7.16 and 7.17, the measurements were taken for different samples in order to compare and evaluate the effect of small and big diodes independently. For the null reconfigurable design (Figures 7.18 and 7.19) all measurements were taken for the same sample on which three diodes are used and biased individually to steer the null in the three directions and maintain a constant resonant frequency. In order to get the nulls in the side directions, the corresponding big diode is biased. In order to get the null in the feeding line direction, the small diode on the matching stub L1 in Figure 7.10 is biased in order to maintain the resonance frequency constant at 5.65 GHz while none of the big diodes is biased. In Figure 7.18 and Figure 7.19 where the simulated and measured results are presented, respectively, it is obvious

that the steering of the null is achieved with high precision. The slot dimensions are optimized for the frequency of 5.8 GHz.

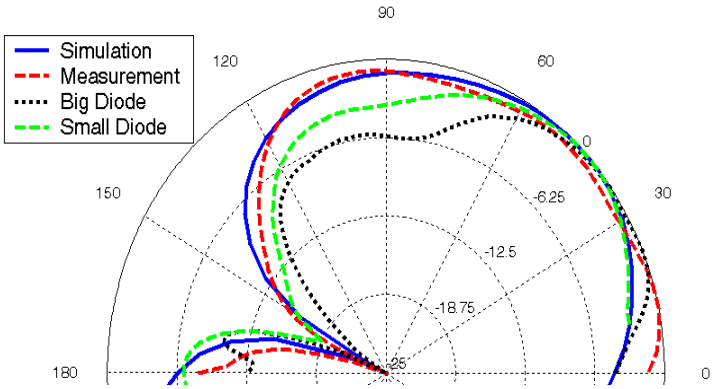

Figure 7.16: Radiation patterns for the 5.2 GHz frequency design when the short is placed at 315^{o}. Simulation, measurement with hard-wired short, measurement with the big diode biased, and measurement with the small diode biased are presented.

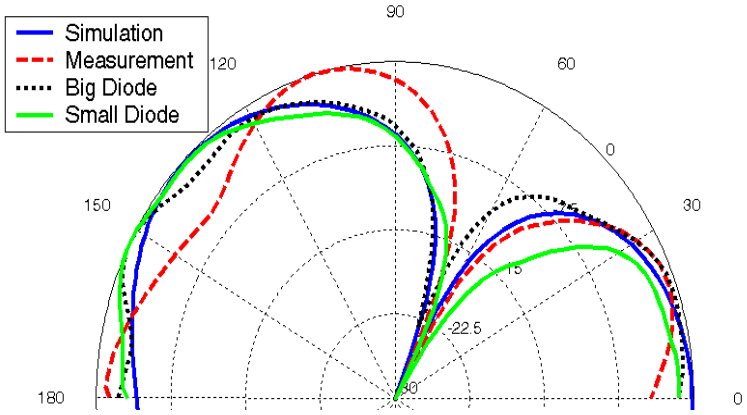

Figure 7.17: Radiation patterns for the 6.4 GHz frequency design when the short is placed at 225^{o}. Simulation, measurement with hard-wired short, measurement with the big diode biased, and measurement with the small diode biased are presented.

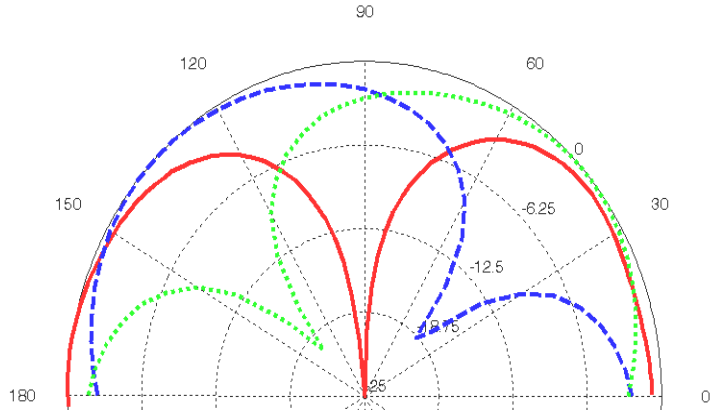

Figure 7.18: Simulated radiation patterns in x-y plane for the null reconfigurable design at f=5.8 GHz. The null is directed at 45^{o}, 90^{o}, and 135^{o} direction. The 90^{o} direction is the null direction when no short is used.

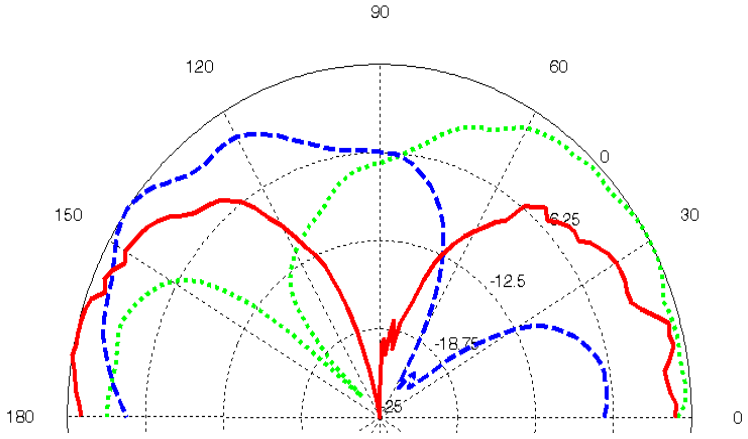

Figure 7.19: Measured radiation patterns in x-y plane for the null reconfigurable design at f=5.65 GHz. The null is directed at 45^{o}, 90^{o}, and 135^{o} direction using two PIN diodes placed at 225^{o} and 315^{o}. The 90^{o} direction is achieved when none of the diodes is biased.

7.4 Summary

A new design for both pattern and frequency reconfigurable annular slot antenna was presented. Matching stubs are used to match the antenna to three different frequencies, 5.2 GHz and 6.4 GHz in addition to the initial central frequency at 5.8 GHz. PIN diodes are used to connect or disconnect the stubs creating a reconfigurable matching network. The radiation pattern control is achieved by activating/deactivating shorts on the slot. As a result the null is redirected to a different direction. As a benchmarking approach, the shorts are implemented by use of pin diodes. When each diode is forward biased, it is equivalent to a short, and when it is reverse biased, it behaves as a capacitive load. In the latter case, when no diodes are forward biased, the slot antenna behaves like the unloaded slot antenna and the null appears in the feeding line direction. The results for this antenna are presented at three separate frequencies. Any other frequency can be matched using the same technique as long as the radiation efficiency for that frequency is satisfactory. The same applies with the position of the shorts. The possible directions are not limited to the ones used in this paper but in that case also, the matching stubs need to be redesigned and optimized for the preferred short direction, since the short direction affects the equivalent load at the end of the transmission line. The measured results are compared to the simulations and are found to be in very good agreement. The proposed antenna is compact and easy to integrate with other microwave components.

CHAPTER VIII

CONCLUSION

The design and implementation of compact reconfigurable antennas for UWB and WLAN applications has been investigated. UWB elliptical monopoles with reconfigurable band rejection in the WLAN frequency range have been implemented, using MEMS switches actuated without the need of DC bias lines. For WLAN applications, an annular slot antenna was implemented that demonstrates reconfigurable frequency operation and radiation pattern capabilities, using PIN diodes. These are the first such illustrations. Reconfigurable antennas can be used for next generation cognitive radio systems. In the process and in addition to those prototypes several other UWB antenna designs were also investigated and led to a design methodology for designing compact broadband antennas. Taking advantage of LCP's flexibility the properties of UWB radiators in non-planar shapes were studied and demonstrated that their performance is very similar to the performance of their planar counterparts. Something that indicates that antennas for a number of conformal applications, like wearable electronics, can be designed and tested in planar shapes and still be trusted to operate equally well in non-planar shapes.

A double exponentially tapered slot antenna with high gain was implemented. The flexibility of the prototype and the directive radiation patterns make it a good candidate for portable or wearable personal radar devices. The need for more compact and omni-directional antennas for mobile and personal communication applications led to the design of the U-stub fed elliptical slot, and in an improved iteration, the design of the cactus-shaped monopoles that demonstrate remarkable size and radiation pattern

characteristics that make them excellent candidates for such applications. The design of the cactus-shaped monopoles demonstrated a broadband matching technique. Good matching was achieved by modifying the equivalent load of the feed line. That was achieved by altering the geometrical features of the antenna.

In the attempt of designing compact omni-directional antennas, CPW fed elliptical monopoles were built. The matching difficulties were overcome with the implementation of a broadband transition from a CPW line to the elliptical radiator that reduced the high real part of the input impedance without changing the radiator and therefore degrading the radiation characteristics of the monopole.

Several of the fabricated antennas were tested when they were mounted on non-planar surfaces. Return loss, radiation pattern and channel measurements, demonstrated the applicability of conformal UWB antennas.

Two kind of resonating elements were integrated using MEMS switches with a version of the elliptical monopole to provide reconfigurable band rejection in the frequency range occupied by WLAN applications. A $\lambda/2$ long U-shaped slot was used in one case and two inverted L-shaped $\lambda/4$ long stubs were used in the second case. The presence of the band rejection protects a UWB radio from high noise levels coming from neighboring WLAN transmitters, while its elimination improves the available bandwidth when the noise level is low.

Finally a reconfigurable annular slot antenna in both frequency and radiation pattern was presented. PIN diodes were used to connect and disconnect the matching stubs that control the frequency operation, and another type of PIN diodes is used to direct the null of the radiation part in a desired predefined direction.

REFERENCES

[1] R. R.Tummala, "SOP: What is it and why? A new microsystem-integration technology paradigm - Moores law for system integration of miniaturized convergent systems of the next decade," IEEE Trans. Adv. Packag., vol. 27, pp. 241–249, May 2004.

[2] R. R. Tummala, and J. Laskar, "Gigabit wireless: System-on-a-Package technology," Proc. IEEE, vol. 92, pp. 376–387, Feb. 2004.

[3] K. Lim, S. Pinel, M. Davis, A. Sutono, C. Lee, D. Heo, A. Obatoynbo, J. Laskar, M. M. Tentzeris, and R. R. Tummala, "RF-System-on-Package (SOP) for wireless communications," IEEE Microwave, pp. 88–99, March 2002.

[4] Rogers Corporation advanced circuit materials website. [Online]. Date accessed: Dec.2003. Available: http://www.rogerscorporation.com/acm/index.htm.

[5] Taconic microwave materials website. Various materials data sheets. [Online]. Date accessed: Jul. 2005. Available: http://www.taconic-add.com/.

[6] C. Q. Scrantom, and J. C. Lawson, "LTCC technology where we are and where were going-II," in Technologies for wireless applications, IEEE MTT-S Symp., pp. 193–200, February 1999.

[7] B. Hunt, and L. Devlin, "LTCC for rf modules." IEE Seminar on Packaging and Interconnects at Microwave and mm-Wave Frequencies, June 2000.

[8] K. Jayaraj, T. E. Noll, and D. R. Singh, "A low cost multichip packaging technology for monolithic microwave integrated circuits," IEEE Trans. Antennas Propagat., vol. 43, pp. 992–997, September 1995.

[9] E. C. Culbertson, "A new laminate material for high performance PCBs: Liquid crystal polymer copper clad films," in IEEE Electronic Components and Technology Conf., pp. 520–523, May 1995.

[10] C. Khoo, B. Brox, R. Norrhede, and F. Maurer, "Effect of copper lamination on the rheological and copper adhesion properties of a thermotropic liquid crystalline polymer used in PCB applications," IEEE Trans. Comp., Packag., Manufact. Technol. A, vol. 20, pp. 219–226, July 1997.

[11] L. Chen, M. Crnic, L. Zonghe, and J. Liu, "Process development and adhesion behavior of electroless copper on liquid crystal polymer (LCP) for electronic packaging application," IEEE Trans. Comp., Packag., Manufact. Technol. B, vol. 25, pp. 273–278, October 2002.

[12] B. Farrell, and M. S. Lawrence, "The processing of liquid crystalline polymer printed circuits," in IEEE Electronic Components and Technology Conf., pp. 667–671, May 2002.

[13] PMTEC LCP Materials Symp., Huntsville, AL, Oct. 29, 2002.

[14] M. F. Davis, S.-W. Yoon, S. Pinel, K. Lim, and J. Laskar, "Surface mountable liquid crystal polymer package with vertical via transition compensating wire inductance up to v-band," in IEEE MTT-S Int. Microwave Symp. Dig., vol. 2,pp. 1155–1158, June 2003.

[15] Z. Wei and A. Pham, "Liquid crystal polymer (LCP) for microwave/millimeter wave multi-layer packaging," in IEEE MTT-S Int. Microwave Symp. Dig., pp. 2273–2276, June 2003.

[16] Anon., FCC First Report and Order on Ultra-Wideband Technology, February, 2002.

[17] Date accessed: June 2006 http://www.multispectral.com

[18] R. A. Scholtz, D. Pozar, and W. Namgoong, "Ultrawideband Radio: A Tutorial," EURASIP Journal on Applied Signal Processing (Special Issue on Ultrawideband Radio), pp. 252-272, vol. 3, 2005.

[19] C. Balanis, Antenna Theory: Analysis and Design, New York, John Wiley & Sons, Inc., 1997.

[20] K. Wong, Compact and Broadband Microstrip Antennas, New York, John Wiley & Sons, Inc., 2002.

[21] W. Stutzman, G. Thiele, Antenna Theory and Design, New York, John Wiley & Sons, Inc., 1998.

[22] S. Bokhari, J. Zurcher, J. Mosig, F. Gardiol, "A small microstrip patch antenna with a convenient tuning option," IEEE Transactions on Antennas and Propagation, vol. 44, Issue: 11, Nov. 1996, pp. 1521-1528.

[23] S. Dey, R. Mittra, T. Kobayashi, M. Itoh, S. Maeda, "Circular polarized meander patch antenna array," IEEE Antennas and Propagation Society International Symposium, vol. 2, July 1996, pp. 1100-1103.

[24] Sang-Gyu Kim and K. Chang "Ultra wideband exponentially-tapered antipodal Vivaldi antennas" IEEE Antennas and Propagation Society Symposium, vol. 3, pp. 2273 – 2276, June 2004, Monterey, CA.

[25] J. J. Lee and S. Livingston, “Wide band bunny-ear radiating element”, IEEE Antennas Propagation Society International Symposium. pp. 1604-1607., July 1993, Ann Arbor, MI.

[26] M.C. Greenberg, L.L. Virga, “Characterization and design methodology for the dual exponentially tapered slot antenna” IEEE Antennas and Propagation Society International Symposium, vol.1, pp. 88 - 91, July 1999, Atlanta, GA.

[27] M.C. Greenberg, K.L. Virga, C.L. Hammond, “Performance characteristics of the dual exponentially tapered slot antenna (DETSA) for wireless communications applications” IEEE Transactions on Vehicular Technology, vol.52 , no.2 , pp. 305 – 312, March 2003.

[28] Yo-Shen Lin, Tzyh-Ghuang Ma, Shyh-Kang Jeng, Chun Hsiung Chen, **“**Coplanar waveguide-fed dual exponentially tapered slot antennas for ultra-wideband applications**”,** Antennas and Propagation Society Symposium, vol. 3, pp. 2951 – 2954, June 2004, Monterey, CA.

[29] K. S. Yngvesson, D. H. Schaubert, T. L. Korzeniowski, E. L. Kollberg,T. Thungren, and J. F. Johansson, “Endfire tapered slot antennas on dielectric substrates,” IEEE Transactions on Antennas and Propagation, vol. AP-33, pp. 1392–1400, December 1985.

[30] Janaswamy and D. H. Schaubert, “Analysis of the tapered slot antenna,” IEEE Transactions on Antennas and Propagation, vol. AP-35, pp. 1058–1064, September 1987.

[31] S. Nikolaou, G. E. Ponchak, J. Papapolymerou, and M. M. Tentzeris, “ Double exponentially tapered slot antenna (DETSA) on Liquid Crystal Polymer (LCP) for UWB applications”, IEEE APS 2005, vol. 2A pp. 623-626, July 2005.

[32] Y. H. Suh and I. Park, “Eccentric annular slot antenna”, IEEE AP 2001, vol. 1, pp. 94-97, July 2004.

[33] R. Chair, A.A. Kishk, and K. F. Lee, “Ultra-wideband coplanar wavequide fed rectangular slot antenna”, IEEE Antennas and Wireless Propagation Letters, vol. 3, 2004.

[34] S. Nikolaou, G. E. Ponchak, J. Papapolymerou, and M. M. Tentzeris, “CPW-fed elliptical slot antenna with a tuning uneven U-shaped stub on liquid crystal polymer (LCP)”, accepted for presentation at the IEEE ACES 2006, Miami. FL, March 2006.

[35] T. Yang and W.A Davis, “Planar half-disc antenna structures for ultra wide-band communications.”, IEEE APS 2004, vol. 3, pp. 2508-2511, June 2004.

[36] J. Liang, C. C. Chiau, X. Chen, and C. G. Parini, "Printed circular disc monopole antenna for ultra wideband applications", Electronic Letters, vol. 40, no. 7, pp. 1246-1248, September 2004.

[37] J.T. Bernhard,R. Wang, R. Clark, and P. Mayes, "Stacked reconfigurable antenna elements for space-based radar applications", IEEE Antennas and Propagation Society International Symposium, vol. 1, pp. 158 – 161, July 2001.

[38] K. Tomiyasu, "Conceptual reconfigurable antenna for 35 GHz high-resolution spaceborne synthetic aperture radar", IEEE Transactions on Aerospace and Electronic Systems, vol. 39, Issue: 3, pp. 1069 – 1074, July 2003.

[39] J.T. Aberle, Sung-Hoon Oh, D.T. Auckland, and S.D. Rogers, "Reconfigurable antennas for wireless devices" IEEE Antennas and Propagation Magazine, vol. 45, Issue:6, pp. 148 – 154, December 2003.

[40] G.H. Huff, J. Feng, Shenghui Zhang, G. Cung, and J.T. Bernhard "Directional reconfigurable antennas on laptop computers: Simulation, measurement and evaluation of candidate integration positions", IEEE Transactions on Antennas and Propagation, vol. 52, Issue:12, pp. 3220 – 3227, December 2004.

[41] J. Nanbo, Y. Fan, and Y. Rahmat-Samii, "A novel reconfigurable patch antenna with both frequency and polarization diversities for wireless communications", IEEE Antennas and Propagation Society International Symposium, vol. 2, pp.1769-1799, June 2004.

[42] J.T. Bernhard, G.H. Huff, J. Feng, S. Zhang, and G.Cung, "Reconfigurable portable antenna systems for high-speed wireless communication", IEEE Topical Conference on Wireless Communication Technology, pp.82 – 83, October 2003.

[43] C. E. Tong, and R. Blundel, "An annular slot antenna on a dielectric half-space", IEEE Transactions on Antennas and Propagation, vol. 2, no.7, pp. 967 – 974, July 1994.

[44] H. Morishita, K. Hirasawa, and K. Fujimoto, " Analysis of a cavity-backed annular slot antenna with one point shorted", IEEE Transactions on Antennas and Propagation, vol. 39, no.10, pp. 1472 – 1478, October 1991.

[45] S. Kanamaluru, Ming-Yi Li, and Kai Chang, "Narrowband filter and annular slot antenna for PCS applications", IEEE MTT-S International Microwave Symposium Digest, vol. 2 , pp. 987 – 990, June 1996.

[46] Cheng-Shong Hong, "Small annular slot antenna with capacitor loading" Electronics Letters , vol. 36 , no.2, pp. 110 – 111, January 2000.

[47] H. Tehrani and Kai Chang, "A multi-frequency microstrip-fed annular slot antenna", IEEE Antennas and Propagation Society International Symposium, vol. 2, pp. 632 – 635, July 2000.

[48] F. Le Bolter, and A. Louzir, "Multi-band annular slot antenna for WLAN applications", IEEE Antennas and Propagation Society Conference, vol. 2, pp. 529 – 532, April 2001.

[49] N. Behdad and K. Sarabandi, "A wideband bi-semicircular slot antenna", IEEE Antennas and Propagation Society Symposium, vol. 2, pp. 1903 – 1906, June 2004.

[50] K.-H. Kim, Y.-J. Cho, S.-H. Hwang, S.-O. Park, "Band-notched UWB planar monopole antenna with two parasitic patches", Electronic Letters vol. 41, pp. 783 – 785, July 2005.

[51] Y. Gao, B.-L. Ooi, A.P. Popov, "Band-notched ultra-wideband ring-monopole antenna", Microwave and Optical Techology Letters, vol. 48, issue 1, pp. 125-126, January 2006.

[52] I.-J. Yoon, H. Kim, K. Chang, Y. J. Yoon, Y.-H. Kim, "Ultra wideband tapered slot antenna with band-stop characteristic", IEEE APS 2004, vol. 2, pp. 1780 – 1783, Jun. 2004.

[53] K. Chung, J. Kim, J. Choi , "Wideband microstrip-fed monopole antenna having frequency band-notch function", IEEE Microwave and Wireless Components Letters, vol. 15, issue 11, pp. 766 – 768, Nov. 2005.

[54] Y. J. Cho, K. H. Kim, D. H. Choi, S. S. Lee, S.-O. Park, "A miniature UWB planar monopole antenna with 5-GHz band-rejection filter and the time-domain characteristics", IEEE Transactions on Antennas and Propagation, vol. 54, issue 5, pp. 1453-1460, May 2006.

[55] W. Choi, J. Jung, K. Chung, J. Choi, "Compact wideband printed monopole antenna with frequency band-stop characteristic" IEEE APS 2005 vol. 3A, pp. 606-609, July 2005.

[56] S. Nikolaou, G.E. Ponchak, J.Papapolymerou, M.M. Tentzeris, "Conformal double exponentially tapered slot antenna (DETSA) on LCP for UWB applications", *IEEE Trans. Antennas Propag.,* vol. 54, issue 6, pp.1663 – 1669, Jun. 2006.

[57] S. Nikolaou, G. Ponchak, M.M. Tentzeris, J. Papapolymerou, "Compact Cactus-Shaped Ultra Wide-Band (UWB) Monopole on Organic Substrate", to appear in Procs. of the 2006 IEEE-APS Symposium, pp.1035-1038, Waikiki, HI, June 2007.

[58] S. Nikolaou, R. Bairavasubramanian, G. E. Ponchak, J. Papapolymerou, and M.M. Tentzeris, "Development of Miniaturized Flexible UWB Antennas on LCP Organic Materials", Submitted to IET Microwaves, Antennas and Propagation Proceedings.

[59] S. Nikolaou, B. Kim, G.E. Ponchak, M.M. Tentzeris, and J. Papapolymerou, "Compact Cactus-Shaped Monopole UWB Antenna with Controllable Return Loss", Submitted to IEEE Antennas and Wireless Propagation Letters

[60] D.C. Thompson, O.Tantot, H. Jallageas, G.E. Ponchak, M.M. Tentzeris, J. Papapolymerou, "Characterization of liquid crystal polymer (LCP) material and transmission lines on LCP substrates from 30 to 110 GHz", IEEE Transactions on Microwave Theory and Techniques, vol. 52, no.4, pp. 1343-1352, April 2004.

[61] Ansoft HFSS 9.0 User manual.

[62] J.D.S. Langley, P.S. Hall, P. Newham, "Balanced antipodal Vivaldi antenna for wide bandwidth phased arrays", IEE Proceedings on Microwaves, Antennas and Propagation, vol. 143, Issue 2, pp. 97-102 April 1996.

[63] Hyungkuk Yoon, Hyungrak Kim, Kihun Chang, Young Joong Yoon, Young-Hwan Kim," A study on the UWB antenna with band-rejection characteristic", IEEE Antennas and Propagation Society Symposium, vol. 2, pp. 1784 - 1787 June 2004, Monterey, CA.

[64] Tzyh-Ghuang Ma and Shyh-Kang Jeng **"**A compact tapered-slot-feed annular slot antenna for ultra-wideband applications**",** IEEE Antennas and Propagation Society Symposium, vol. 3, pp. 2943 – 2946, June 2004, Monterey, CA.

[65] R. Q. Lee and R. N. Simons, "Effect of curvature on tapered slot antennas," IEEE Antennas and Propagation Society Symposium, vol. 1, pp. 188-191, July 1996.

[66] K. F. Lee and W. Chen, "Advances in Microstrip and Printed Antennas", John Wiley & sons, New York 1997, pp. 477 – 479.

[67] C.-Y. Huang, W.-C. Hsia, "Planar elliptical antenna for ultra-wideband communications" Electronics Letters, vol. 41, Issue 6, pp.296 – 297, March 2005

[68] S. Nikolaou, G. E. Ponchak, M.M. Tentzeris, and J. Papapolymerou, "Study of a CPW line to an ultra wideband elliptical radiator transition", Submitted to IEEE Microwave Components Letters.

[69] W. Choi, K. Chung, J. Jung, J. Choi, "Compact ultra-wideband printed antenna with band-rejection characteristic", Electronics Letters, vol. 41, Issue 18, pp. 990 – 991, September 2005.

[70] M. Klemm, I.Z. Kovcs, G.F. Pedersen, G. Troster, "Novel small-size directional antenna for UWB WBAN/WPAN applications",Antennas and Propagation, IEEE Transactions on vol. 53, Issue 12, pp. 3884 – 3896, December 2006.

[71] S. Nikolaou, B. Kim, G.E. Ponchak, M.M. Tentzeris, and J. Papapolymerou, "Study of Conformal Omni-Directional UWB Antennas on Flexible Substrate Mounted on Non-Planar Surfaces for WBAN Applications", Submitted to IEEE Transactions on Antennas and Propagation.

[72] K.C.L. Chan, Y. Huang, X. Zhu, "A planar elliptical monopole antenna for UWB applications", IEEE ACES International Conf., pp.182 – 185, April 2005.

[73] L. Pengcheng, L. Jianxin, C. Xiaodong, "Study of printed elliptical/circular slot antennas for ultrawideband applications", IEEE Trans. Antennas Propag., vol. 54, pp.1670 – 1675, June 2006.

[74] J. Liang, L. Guo,C.C. Chiau, X. Chen,G.C. Parini, "Study of CPW-fed circular disc monopole antenna for ultra wideband applications", IEE Microwaves, Antennas and Propag. Proc., pp.520 – 526, 2005.

[75] T. Yang, S. Seong-Youp, R. Nealy, W.A. Davis, W.L. Stutzman, "Compact antennas for UWB applications", IEEE Aerospace Electr. Syst. Magas., vol. 19, pp. 16 – 20, May 2004.

[76] S. Nikolaou, G. E. Ponchak, M. M. Tentzeris, and J. Papapolymerou, "UWB elliptical monopoles with reconfigurable band notch using MEMS switches actuated without DC bias lines", Submitted to IEEE Transactions on Antennas and Propagation

[77] W.-S. Lee, D.-Z. Kim, K.-J. Kim, J.-W. Yu, "Wideband planar monopole antennas with dual band-notched characteristics" IEEE Transactions on Microwave Theory and Techniques, vol.54, issue 6, no. 2, pp.2800 – 2806, June 2006

[78] Y. J. Cho, K. H. Kim, D. H. Choi, S. S. Lee, S.-O. Park, "A miniature UWB planar monopole antenna with 5-GHz band-rejection filter and the time-domain characteristics",IEEE Transactions on Antennas and Propagation, vol. 54, issue 5, pp.1453 – 1460, May 2006.

[79] B. Kim, S. Nikolaou, D. E. Anagnostou, Y. S. Kim, M. M. Tentzeris, and J. Papapolymerou, "A ConformaL-shaped Antenna on Liquid Crystal Polymer Substrate for Ultra-Wideband Systems with WLAN Band-Stop Characteristics", submitted to IEEE Transactions on Antennas and Propagation.

[80] N. Kingsley, D. E. Anagnostou, M. M. Tentzeris, J. Papapolymerou, "RF MEMS Sequentially-Reconfigurable Sierpinski Antenna on a Flexible, Organic Substrate Without the Need for DC Bias Lines" submitted to IEEE Transactions on Antennas and Propagation.

[81] N. Kingsley and J. Papapolymerou, "Organic 'Wafer-Scale' Packaged Miniature Four-Bit RF MEMS Phase Shifter", IEEE Transactions on Microwave Theory and Technique, vol. 54, No. 3, March 2006.

[82] N. Kingsley, G. Wang, J. Papapolymerou, "Comparative Study of Analytical and Simulated Doubly-Supported RF MEMS Switches for Mechanical and Electrical Performance", Applied Computational Electromagnetics Society Journal, vol. 21, No. 1, pp. 9-15, March 2006.

[83] S. Nikolaou, R. Bairavasubramanian, C. Lugo Jr., I. Carrasquillo, D.C. Thompson, G.E. Ponchak, J. Papapolymerou, and M.M. Tentzeris, "Pattern and Frequency Reconfigurable Annular Slot Antenna using PIN Diodes", IEEE Transactions on Antennas and Propagation, Vol.54, No.2, pp. 439-448, February 2006.

[84] K.C. Gupta, R. Garg, I. Bah, and P. Bhartia, "Microstrip Lines and Slotilines", Artech House, Second Edition, pp. 282 – 286.

[85] C. A. Balanis "Antenna Theory Analysis and Design", John Wiley & sons, Second Edition, pp. 152 –157.

[86] H. Morishita, K. Hirasawa, and K. Fujimoto, " Analysis of a cavity-backed annular slot antenna with one point shorted", IEEE Transactions on Antennas and Propagation, vol. 39, no.10, pp. 1472 – 1478, October 1991.

[87] R. L, Li, V. F. Fusco and R. Cahil, "Pattern shaping using a reactively loaded wire loop antenna", IEE Proceedings on Microwaves, Antennas and Propagation, vol. 148, Issue: 3, pp. 203 – 208, June 2004.

[88] P. Hallbjorner, "Electrically small unbalanced four-arm wire antenna" IEEE Transactions on Antennas and Propagation, vol. 52, Issue: 6, pp. 1424 – 1428, June 2004.

[89] RongLin Li, G.DeJean, M.M. Tentzeris, and J. Laskar, "Development and analysis of a folded shorted-patch antenna with reduced size", IEEE Transactions on Antennas and Propagation, vol. 52, Issue: 2, pp. 555 – 562, February 2004.

[90] Cheng-Shong Hong, "Small annular slot antenna with capacitor loading" Electronics Letters, vol.36, no.2, pp. 110 – 111, January 2000

[91] C.Lugo and J. Papapolymerou, “Electronic switchable bandpass filter using PIN diodes for wireless low cost system-on-a-package applications.” IEE Proceedings on Microwaves, Antennas and Propagation, vol. 151, Issue: 6, pp. 497 – 502, December 2004.